2005-03-11

Simulation-Based Design Under Uncertainty for Compliant Microelectromechanical Systems

Jonathan W. Wittwer
Brigham Young University - Provo

SIMULATION-BASED DESIGN UNDER UNCERTAINTY FOR COMPLIANT MICROELECTROMECHANICAL SYSTEMS

by

Jonathan W. Wittwer

A dissertation submitted to the faculty of

Brigham Young University

in partial fulfillment of the requirements for the degree of

Doctor of Philosophy

Department of Mechanical Engineering

Brigham Young University

April 2005

BRIGHAM YOUNG UNIVERSITY

GRADUATE COMMITTEE APPROVAL

of a dissertation submitted by

Jonathan W. Wittwer

This dissertation has been read by each member of the following graduate committee and by majority vote has been found to be satisfactory.

Date	Larry L. Howell, Chair
Date	Kenneth W. Chase
Date	Alan R. Parkinson
Date	Timothy W. McLain
Date	C. Shane Reese

BRIGHAM YOUNG UNIVERSITY

As chair of the candidate's graduate committee, I have read the dissertation of Jonathan W. Wittwer in its final form and have found that (1) its format, citations, and bibliographical style are consistent and acceptable and fulfill university and department style requirements; (2) its illustrative materials including figures, tables, and charts are in place; and (3) the final manuscript is satisfactory to the graduate committee and is ready for submission to the university library.

_____ _____

Date

Larry L. Howell
Chair, Graduate Committee

Accepted for the Department

_____

Matthew R. Jones
Graduate Coordinator

Accepted for the College

_____

Douglas M. Chabries
Dean, Ira A. Fulton College of Engineering and Technology

ABSTRACT

SIMULATION-BASED DESIGN UNDER UNCERTAINTY FOR COMPLIANT MICROELECTROMECHANICAL SYSTEMS

Jonathan W. Wittwer

Department of Mechanical Engineering

Doctor of Philosophy

The high cost of experimentation and product development in the field of micro-electromechanical systems (MEMS) has led to a greater emphasis on simulation-based design for increasing first-pass design success and reliability. The use of compliant or flexible mechanisms can help eliminate friction, wear, and backlash, but compliant MEMS are sensitive to variations in material properties and geometry. This dissertation proposes approaches for design stage uncertainty analysis, model validation, and robust optimization of nonlinear compliant MEMS to account for critical process uncertainties including residual stress, layer thicknesses, edge bias, and material stiffness. Methods for simulating and mitigating the effects of non-idealities such joint clearances, semi-rigid supports, non-ideal loading, and asymmetry are also presented. Approaches are demonstrated and experimentally validated using bistable micromechanisms and thermal micro-actuators as examples.

ACKNOWLEDGMENTS

Many people deserve thanks for helping to complete the work reported in this dissertation. All along the way people have provided answers to questions, access to equipment, help with testing and analysis, and often just a listening ear or thoughtful insight. I am extremely grateful for the support of my family, advisor, friends, colleagues, committee members, and my Heavenly Father. I want to especially thank my wife for her support, friendship, and patience. My advisor, Larry Howell, has been a great mentor and I appreciate the many hours he has spent guiding my research, editing papers, and helping me see things from a broader perspective.

In addition to my advisor and committee members, a number of people have contributed to the technical aspects of this research, including Mike Baker, Les Reasonover, Sydney Wait, Jeff Anderson, Michael Cherry, Sita Mani, Mike Shaw, Nicholas Johnson, Becky Hubbard, David Dawson, and Jeremy Walraen. I thank everyone who I have had the pleasure to work with at Brigham Young University and Sandia National Laboratories.

The funding for this research came from a National Science Foundation Graduate Research Fellowship, the Sandia National Laboratories MESA Institute program, and other grants (NSF grant CMS-9978737) and scholarships through Brigham Young University and the Department of Mechanical Engineering.

TABLE OF CONTENTS

LIST OF TABLES

LIST OF FIGURES

CHAPTER 1 INTRODUCTION

1.1 Motivation

Research and development in the field of microelectromechanical systems (MEMS) usually involves fabrication processes that push the limits of technology or processes that are under development. In such cases, it is common to deal with large uncertainties due to lack of data, inherent variation in material properties and feature dimensions, variable loading conditions, adverse environmental effects, and other reliability issues. The use of compliant or flexible mechanisms has helped minimize the effects of friction, wear, and backlash in MEMS. However, compliant MEMS can be highly sensitive to variations in material properties and geometry. Due to the high cost and slow turnaround during the prototyping stage of micro mechanism design, it is important to take these uncertainties into account in order to increase reliability and shorten the product development cycle.

Using computer simulations to consider uncertainties during design can provide a cost-effective approach to MEMS development, particularly when little can be done to reduce inherent process variations. For example, uncertainty analysis can aid in developing testing procedures and designing devices to be insensitive to variation in order to

increase yield and reliability. Simulation-based design under uncertainty for MEMS has the potential for enabling the following important objectives:

- Increased first-pass design success
- Improved understanding of device behavior
- Model validation using both experimental data and computer simulations
- Feasibility studies for deciding whether a given design can achieve performance objectives
- Improved device performance through robust design

One of the methods for increasing first-pass success in MEMS design is to fabricate multiple devices using various design-of-experiment approaches. Uncertainty analysis and sensitivity analysis can aid in screening variables and determining factor levels in order to reduce the size of these experiments and increase the chances that the desired results will be obtained. An indirect benefit of uncertainty analysis is a better understanding of the behavior of the device. This is helpful for identifying lurking variables when unexpected results are obtained.

Model validation is particularly important in MEMS because designers must often deal with non-idealities or phenomena not common in macro mechanism design. Due to the cost and difficulty of obtaining experimental data, it is often not practical to obtain a sufficient amount of data required for traditional model validation. Modern simulation-based uncertainty analysis methods offer a means to validate models where only a limited amount of data is available.

Feasibility studies can be used to assess the risk in pursuing the development of a particular design when sources of uncertainty are understood for the fabrication process.

By identifying the significant variables affecting design performance, modifications can either be made to the process to try to reduce variation, or the design can be modified to avoid or design around the known variations.

Methods for optimization under uncertainty can be used to reduce sensitivity to variations in order to create more robust designs, thereby increasing reliability and yield. This approach is particularly useful in MEMS design, where there is little control over the process variations or tolerances.

1.2 Purpose

The purpose of this research is to develop approaches for simulation-based design under uncertainty in compliant microelectromechanical systems and to demonstrate how these can be used to evaluate design performance, increase first-pass success, validate models, and increase device yield. Results will be demonstrated through simulation, fabrication, and testing.

1.3 Approach

Implementation of design-stage uncertainty methods requires (1) an understanding of the sources of errors and variation, (2) a parametric model that can be used for simulating effects of variation, and (3) an efficient means for running the computer experiment and analyzing the data. In order to make simulation-based design under uncertainty an effective approach for MEMS, all three of these challenges must be met.

Chapter 2 provides a review of compliant MEMS and the application of design-stage uncertainty analysis in MEMS. It also provides a general review of uncertainty analysis methods.

Chapter 3 discusses in detail some of the important sources of variation in compliant MEMS. It presents a generalized method for uncertainty analysis when a model consists of implicit systems of equations. A linear displacement bistable micromechanism is used as an example, where the main focus is to show how design-stage uncertainty analysis can aid in achieving first-pass design success.

Chapters 4 and 5 discuss modeling issues related to compliant MEMS, providing ways to reduce modeling error by improving accuracy or mitigating non-idealities. In addition to the effects of joint clearances discussed in Chapter 3, these chapters consider the effects of local elasticity in semi-rigid supports, non-ideal loading conditions, and asymmetry that may result from process variations.

Chapter 6 provides a detailed overview of an approach for simulation-based design under uncertainty that can be used for analyzing nonlinear finite element models. A simple and efficient second-order uncertainty analysis method is presented that can account for large relative uncertainties in complex models, while maintaining simplicity and transparency (ease of interpretation). The approach is used in model validation of a thermal microactuator. Some of the specific contributions related to this method are:

- Use of multivariate multiple linear regression to create efficient first and second-order surrogate models

- Visualization of relative uncertainty contributions via area charts, including correlation
- Inclusion of distribution information via surrogate-based Monte Carlo simulation

The main contribution of this dissertation is the demonstration that simulation-based design under uncertainty can enable the development of MEMS devices that are less sensitive to existing process variations. In Chapter 7, this approach is experimentally validated, using a case study involving a nonlinear, fully compliant, bistable micromechanism.

The final chapter summarizes the main contributions of this dissertation and provides recommendations for further research. Several of the chapters have been published or submitted for publication as separate articles, so additional background and conclusions are provided within individual chapters.

CHAPTER 2 BACKGROUND AND LITERATURE REVIEW

2.1 Compliant MEMS

The past decade has seen a rapid expansion of methods for designing and analyzing flexible mechanisms (Howell, 2001; Lobontiu, 2003; Smith, 2000). The need for greater accuracy and precision, along with advances in the ability to model complex elastic systems, has led to an increase in the use of flexible or compliant mechanisms in precision machinery and instrumentation (Smith and Chetwynd, 1992; Smith, 2000). The elimination of traditional mechanical joints through the use of material compliance or elasticity eliminates some of the largest problems in precision mechanism design, namely backlash, wear, and friction. These characteristics have made compliant mechanisms particularly useful in micro-electro-mechanical systems (MEMS) (Kemeny *et al*., 2002), where assembly is either difficult or impossible, and joint clearances and wear have proven to be one of the main problems in reliability (Tanner *et al*., 2000a).

One of the most common compliant components in MEMS is the linear suspension spring, or folded-beam linear suspension. It is used in electrostatic comb drives to provide a mechanical restoring force, to eliminate friction, and to prevent shorting by providing purely linear motion (Zhou *et al*., 2001; Legtenberg *et al*., 1996; Jaecklin *et al*., 1993). This type of spring or a similar configuration has also been used for micro resonators

(Tanner *et al*., 2003), on-chip force gauges (Wittwer *et al*., 2002a), and tunable capacitors (Xiao *et al*., 2002). One of the advantages of this type of spring is that it can be modeled using simple analytical equations for the linear spring stiffness, maximum stress, and natural frequency.

A variety of other configurations for suspension springs have been used for RF switches (Peroulis *et al*., 2003), variable capacitors (Nguyen *et al*., 2004; Chen *et al*., 2003), electrostatic actuators (Chan and Dutton, 2000), and electromagnetic actuators (Sadler, *et al*. 2000). Closed-form solutions for the spring stiffness(es) can sometimes be derived or estimated, but the implementation of multi-physics solutions in commercial finite-element analysis software is making it possible to model these devices coupled with electrostatic or electromagnetic models. These models are often complex and computationally expensive, so it is still common to decouple the analysis in order to perform separate structural, modal, dynamic, thermal, and electrostatic analyses.

In addition to using compliant components as springs or suspensions, the small scale of micromachined beams enables the use of the material resistivity to achieve actuation via coulomb heating and thermal expansion. Thermal actuators that make use of this principle have some advantages over electrostatic actuation since they can provide higher forces using lower actuation voltages. The two most common micro thermal actuators are the bent-beam (Lott *et al*., 2001; Que *et al*., 2001; Sinclair, 2000; Park *et al*., 2000; Que *et al*., 1999; Cragun and Howell, 1999), and asymmetric cross-section (Huang *et al*., 2000; Lerch *et al*., 1996; Comtois *et al*., 1995) configurations. A significant amount of work has been done to model these types of thermal actuators in order to provide a means for

designing actuators for specific applications or requirements. Predicting actuator behavior based upon voltage or current input is a very complex problem, involving a combination of thermal, electrical, and structural properties, and efforts are still being made to validate models and investigate non-idealities.

Compliant bistable mechanisms are another common MEMS component, particularly for applications such as switches, relays, valves, nonvolatile or mechanical memory cells, clamps, hinges, and positioners. The first bistable MEMS device, reported by Hälg (1990), made use of residual stress to provide initial curvature to a beam. An electrostatic force was then applied to toggle it into a second stable equilibrium position. Although there are other methods for deriving bistable behavior in MEMS such as electrostatic pull-in, making use of nonlinear compliance can be beneficial since no power is required to hold the device in the two stable equilibrium positions. Although the analysis can be complex, often requiring nonlinear finite-element analysis, the pseudo-rigid-body model has helped simplify the analysis and improve understanding of how compliant bistable mechanisms behave (see Opdahl *et al*., 1998). Pseudo-rigid-body models provide a way to transform the bending of flexible members to a rigid-body kinematics problem. These models have helped to group the different configurations for compliant bistable MEMS that have been developed into the following categories:

- buckling of pre-stressed beams (Saif, 2000; Vangbo, 1998; Yang and Kim, 1995a; Yang and Kim, 1995b; Matoba *et al*., 1994; Halg, 1990)
- buckling of bistable membranes (Capanu *et al*., 2000; Goll *et al*., 1996; Wagner *et al*., 1996)

- having pseudo-rigid-body models that resemble double-slider toggle mechanisms (Qiu *et al*., 2004; Masters and Howell, 2002; Qiu *et al*., 2001; Chang *et al*., 2001; Parkinson *et al*., 2000)
- having pseudo-rigid-body models that resemble four-bar toggle mechanisms (Jensen *et al*., 1999b; Jensen *et al*., 1998)
- having pseudo-rigid-body models that resemble slider-crank mechanisms (Kruglick and Pister, 1998; Howell *et al*., 1994a)
- pinned-pinned snap-through devices (Wittwer *et al*., 2002b ; Baker *et al*., 2000).

Due to the planar nature of surface micromachining, MEMS design often provides an ideal application of advanced compliant mechanism design techniques such as topology and size/shape optimization. Kota *et al*. (2001) used size/shape optimization to design a motion amplifier for an electrostatic comb drive in order to reduce the overall device footprint. Topology optimization has been applied to thermal actuator design, where the additional electrical and thermal energy domains add a high degree of complexity (Yin and Ananthasuresh, 2002; Li and Ananthasuresh, 2001; Jonsmann *et al*., 1999).

2.2 Modeling Methods for Compliant Mechanisms

Modeling the behavior of compliant mechanisms gives a designer greater power to develop custom solutions to specific design problems. Predictive models can also help save development cost and decrease the time to production. Choosing the design method that is most appropriate is a decision that comes down to a complex trade-off between simplicity, efficiency, accuracy, and cost. The modeling method can also affect what uncertainty analysis approach is practical.

Compliant mechanism models can be grouped into one of four categories:

- Classical models
- Finite element models
- Kinematic models (pseudo-rigid-body model)
- Metamodels, surrogate models, or surface response models

Classical modeling methods for compliant mechanisms include shear and moment diagrams, Castigliano's theorem and other energy methods (Gere and Timoshenko, 1997; Juvinall, 1967; Young, 1989), and elliptical integral solutions (Gorski, 1976; Bisshopp and Drucker, 1945). The advantage of some of these models is that for the most part, they involve simple explicit equations that can be solved directly, without iteration. This makes them computationally efficient, but they often involve a great many assumptions that will result in systematic modeling error. The small-deflection assumption is the most common, along with the assumption of isotropy, linear elasticity, and homogeneity.

Finite element models for compliant mechanisms are those based upon continuum mechanics and involve the use of custom or commercial software packages (Sevak and McLarnan, 1974; Gandhi and Thompson, 1981). The main advantage of FEM is the ability to accurately model complex mechanisms, taking into account such things as complex geometries, nonlinear and anisotopric material properties, residual stresses, temperature gradients, dynamics, etc. The disadvantage is that these models are often computationally expensive. Much of the compliant mechanism literature is associated with design methods that make use of FEM, such as topology optimization (Ananthasuresh *et al*., 1994a) and size and shape optimization (Kim and Kota, 2002).

Pseudo-rigid-body models are often derived from classical models or FEM, but they are unique in that they transform the problem from the bending of flexible members to the analysis of rigid-body mechanisms. These models take advantage of the intuition and expertise gained through experience in traditional mechanism design, and are popular for use in developing concepts. Through the use of rigid-body replacement, these concepts are converted to compliant mechanisms using a pseudo-rigid-body model (PRBM), which models the compliance and energy storage in elastic members using torsional and linear springs connected to rigid links (Howell, 2001).

The last major type of model is called a metamodel or a surface response model. Surface response modeling is usually associated with developing a model from experimental data (Morris, 2000; Myers and Montgomery, 1995; Myers *et al*., 1989). Finite-element analysis and other computer modeling methods can be so complex that simplified models are often derived from virtual or computer experiments (Giunta *et al*., 2003; Simpson *et al*., 1997; Montgomery and Evans, 1975). The term metamodel is used to represent a "model of the model" or "surrogate model" derived from these computer experiments. These simpler, more computationally efficient models can then be used for variable screening (Welch *et al*., 1992), reducing design costs (Wang and Ge, 1999), design optimization (Giunta, 2002; Jin *et al*., 2001), optimization under uncertainty (Jin *et al*., 2003; Eldred *et al*., 2002; Wojtkiewicz *et al*., 2001), and model validation (Doebling, *et al*. 2002; Baghdasaryan *et al*., 2002). Pseudo-rigid-body models could be thought of as metamodels because of how they are derived (from FEA or elliptic integral solutions), but they are kept as a separate category because of the correlation to rigid-body kinematics.

2.3 MEMS Reliability and Uncertainty

Current standards for the expression of uncertainty and the methods for detailed uncertainty analysis group uncertainties into two classes, systematic and random (ANSI/ ASME, 1998; ISO, 1993). Systematic, bias, or reducible uncertainty is reduced by increasing the accuracy of the predictive model and through calibration and control of a device after fabrication or assembly. Random, precision, or irreducible uncertainty is a result of random fluctuations in controlled and uncontrolled variables that cannot be reduced through calibration. It is important to distinguish between these two types of uncertainty when performing experiments and reporting measurement uncertainty, but in design-stage uncertainty analysis, all errors are grouped together and considered to be random during the early design stages (Coleman and Steele, 1999).

Reliability has many definitions but probably the most general definition used in mechanical design is the probability that a device will meet certain functional specifications or performance criteria. Haldar and Mahadevan (2000a, pg 2) refer to reliability as a "probabilistic assurance of performance." A more common but narrow definition of reliability is the "...the probability of a device performing its function over a specified period of time and under specified operating conditions" (Rao, 1992). This definition applies particularly to fatigue life estimations which are important in compliant mechanism design. In this research, reliability is used in the general sense to refer to both the probability of failure due to static loading and the probability of meeting general performance specifications.

Although the term reliability-based design (RBD) can indicate that the reliability of a device is considered during design, RBD is often specifically associated with quantitative failure analysis through the use of a mathematical performance function. RBD and parametric design-stage uncertainty analysis are practically synonymous, except that evaluation of reliability requires a performance metric, specification, or limit-state function (Haldar and Mahadevan, 2000a).

MEMS reliability is an active field of research, and is mostly concerned with identifying failure modes and finding ways of preventing failures (Tanner *et al*., 2000a; Rosing *et al*., 2000; Smith *et al*., 1999). Parametric design-stage uncertainty analysis is one method for preventing failures, but it cannot account for all the different failure modes and effects associated with MEMS reliability. Layout errors, configuration management, packaging, handling, storage, modeling errors, and other qualitative or subjective uncertainties all affect the reliability of a device, but may not be quantifiable. Only those quantifiable sources of uncertainty that can be associated with one or more of the model parameters can be included in an uncertainty analysis.

A formal approach for systematically identifying failure modes and their effects is known as FMEA, or failure mode and effect analysis (Stamatis, 1995) and this approach has been applied in the design of pressure sensors (Rosing *et al*., 2000). The FMEA concept provides a way to integrate qualitative failure analysis with quantitative fault simulation and is a widely accepted approach for evaluating and improving system reliability. Some of the issues known to affect MEMS reliability are listed below:

- Stiction and release

- Packaging, handling, and storage
- Modeling errors, assumptions, and simplifications
- Geometric or dimensional variations due to mask misalignments, etch bias, photolithography, conformal deposition, etching, and polishing.
- Bending of support structures or semi-rigid links
- Residual stresses and stress gradients
- Clearances, wear, and particulate contamination and shorting
- Charging and electrostatic discharge
- Non-ideal, unexpected, or variable loading conditions
- Material property variations, nonlinearity, homogeneity, or isotropy
- Fatigue and thermal cycling
- Humidity, stress corrosion cracking, creep, optical degradation, thermal degradation, dormancy
- Radiation
- Shock and vibration

These issues do not affect all MEMS devices, but identifying what effects are significant in the performance of a device will continue to be a necessary part of MEMS research. This dissertation addresses only those sources of uncertainty that can be quantified and included in the parameterization scheme of the model.

In addition to identifying sources of uncertainty in MEMS, it is important to obtain data relative to common levels of replication (Coleman and Steele, 1999; Figliola and Beasley, 1995). For example, Limary *et al*. (1999) provides reproducibility data regarding the SUMMiT V process in the form of trend charts for layer thicknesses, sheet resistance, and line widths. These charts indicate lot-to-lot (process-level) variation and wafer-to-wafer (lot-level) variation. Tanner *et al*. (2003) showed that there is also a significant mod-

ule-to-module (wafer-level) variation for line widths, following a center-to-edge trend that is commonly understood as being a factor in many micro fabrication processes. To be complete, uncertainties ought to also be defined relative to feature-to-feature (module-level) variation, time-dependency (first-order replication), and resolution (zero-order replication).

2.4 Uncertainty Analysis in Compliant MEMS

Considering uncertainty in design is not a new concept, but before stochastic methods were developed, designers typically used deterministic safety factors in order to design for strength-based reliability. The trade-off between increasing accuracy and reliability and minimizing cost has led to reliability-based optimization (Haldar and Mahadevan, 2000a, 2000b; Kuo *et al*., 2001), tolerance allocation (Hong and Chang, 2002), robust optimization (Parkinson *et al*., 1993), and sensitivity analysis (Saltelli *et al*., 2000), all of which are related to modifying a design to meet some performance criteria. These research areas are fairly similar and include both deterministic and probabilistic methods.

One of the earliest papers on error analysis in compliant mechanisms discussed the issue of parasitic deflections (Jones and Young, 1956). The term parasitic error was used to represent any motion other than the desirable motion. In modern kinematic terminology this would be a combination of both structural and mechanical error (Hartenberg and Denavit, 1964). Ryu and Gweon (1997) discussed the effects of machining imperfections, specifically the position variation in drilled holes, on the behavior of flexure-based linear suspensions. But, most of the literature having to do with error analysis in compliant mechanisms is associated with structural error resulting from the choice of modeling

methods, and not mechanical or operational error due to tolerances, clearances, variable loading, or material properties.

Statistical uncertainty and reliability analysis techniques have only recently been applied to compliant mechanisms. Mirfendereski *et al*. (1993) applied stochastic finite-element methods to analyze uncertainty in micro strain gauges. Howell *et al*. (1994d) included variation in link lengths, material properties, and cross-sectional dimensions in the analysis of the strength-based reliability of a bistable compliant mechanism. Smith (2000) provides a fairly detailed discussion of manufacturing issues in compliant mechanisms, but discusses only basic uncertainty and tolerance analysis principles. Wittwer (2001) explored the use of first-order second moment (FOSM) methods for systems of implicit equations as a means of estimating the precision and reliability of micro compliant mechanisms considering the effects of variations in material property and dimensional parameters using the pseudo-rigid-body model. This method is only accurate for cases involving relatively small variations or tolerances, but can be useful in design to determine the effects of uncertainty in individual parameters on various performance functions.

There has not been extensive research on reliability-based design methods or design-stage uncertainty analysis in MEMS, although it is widely known that large variations in material geometric characteristics do exist in microfabrication processes (Limary *et al*., 1999). Most of the existing literature addressing uncertainty analysis in MEMS has to do with microsystem metrology, where basic structural material properties, such as Young's modulus, fracture strength, and residual stress must be inferred from other measurable quantities (Wittwer *et al*., 2002a; Baker *et al*., 2002; Pryputniewicz *et al*. 2002;

Jensen *et al*., 2001; Allen and Johnson, 2001; Tanner *et al*. 2000a; Gupta 2000; Johnson *et al*., 1999; Gianchandani and Najafi, 1996; Mirfendereski *et al*., 1993). In most of these cases, basic uncertainty quantification methods were used to determine overall measurement uncertainty. Mirfendereski *et al*. (1993), Gupta (2000), and Wittwer *et al*. (2002a) provided some discussion of how individual uncertainties contribute to device performance.

Recently, Maute and Frangopol (2003) embedded topology optimization inside of a reliability-based design optimization framework, providing a stochastic method for reliable compliant MEMS design. While this technique has the benefit of taking advantage of modern reliability-based design methods, reliability assessment assumes that (1) you have an accurate understanding of the distributional form of the uncertainties, (2) you have clearly defined metrics and performance specifications, (3) your model has been fully validated. In MEMS, these conditions are rarely ever met, so the reliability or probability of success becomes a rather subjective metric. Still, reliability-based design optimization using stochastic finite-element analysis may be useful for robust design of compliant MEMS.

Visualizing and quantifying uncertainty through the use of error bands, confidence intervals, and relative uncertainty contributions can help a designer make qualitative decisions based upon the predicted performance of a micro sensor or measurement device (Wittwer *et al*. 2002a , Wittwer *et al*., 2002b). Initial research completed by the author (Wittwer, 2002a) demonstrated a generalized design-stage uncertainty analysis method based upon mechanical tolerance analysis for models involving systems of implicit equa-

tions. The method was applied to the design of a micro linear-displacement bistable mechanism and provides a first example of designing a micro mechanism to meet specific performance requirements based upon the use of process uncertainties to ensure first-pass design success. This method will be described in the next, along with the discussion of the sources of uncertainty associated with the design.

2.5 Uncertainty Analysis Methods

Fundamental to almost all analytic or sampling-based uncertainty quantification (UQ), uncertainty analysis (UA), tolerance analysis (TA), and reliability analysis (RA) methods is the principle of error propagation or transmission of variation. Computer models are inherently deterministic, in that the same set of inputs will yield the exact same responses. Real systems are inherently stochastic, so simulating error propagation involves statistical methods for changing the input variables and evaluating the resulting response to determine the mean, standard deviation, or distribution of the response.

Many texts have been written to document the wide variety of methods for performing reliability analysis or probabilistic uncertainty analysis (Haldar and Mahadevan, 2000a; Haldar and Mahadevan, 2000b; Saltelli *et al*., 2000; Coleman and Steele, 1999; Figliola and Beasley, 2000; Rao, 1992; Wadsworth, 1990). These methods are typically either sampling-based or sensitivity-based. The most common sampling based methods are Monte Carlo (MC) simulation and Latin Hypercube (LH) sampling, but others include bootstrap sampling (BS), importance sampling (IS), quasi-Monte Carlo simulation (qMC), and Markov chain Monte Carlo simulation (McMC). The most common sensitivity-based methods are known as differential analysis methods in that the function is expanded using

a first or second-order Taylor series expansion. Propagation of system moments (Shapiro and Gross, 1981; Cox, 1979) is then used to determine the statistical characteristics of the response. Second-order methods combined with the propagation of system moments have been shown to be useful when the function is nonlinear and uncertainties are relatively large (Glancy and Chase, 1999; Lewis, 1993). Another second-order method involves running a Monte Carlo simulation using the second-order Taylor series expansion as a surrogate model (Iman and Helton, 1985).

A third method for uncertainty analysis that applies to computational continuum mechanics is stochastic finite element (SFEA). This approach has been widely developed for structural analysis (Haldar and Mahadevan, 2000b; Ghanem and Red-Horse, 1999; Ma *et al*., 1996; Ghanem and Spanos, 1991; Kam and Lin, 1990; Contreras, 1980; Kleiber, 1980) and has been applied to MEMS (Mirfendereski *et al*. 1993) and compliant mechanisms (Maute and Frangopol, 2003). SFEA is currently used mostly for static assemblies and structures. It is not a very efficient means for analyzing compliant mechanisms, where it is often desirable to predict variation at many positions, because there is a significant amount of work involved in setting up the model.

Another advanced area of research for studying error propagation in engineering models is Bayesian analysis (Chandrashekar and Krishnamurty, 2002; Welch *et al*., 1992), which can be grouped into the sampling-based methods, because much of the research involves choosing optimal sampling plans. Bayesian methods can often be used to include both quantitative and qualitative information for predicting the stochastic response of a model, and the problems are formulated so that information can be updated as it becomes

available. For this reason, Bayesian methods are receiving attention as useful approaches for model validation. However, an advanced understanding of statistics is required.

Most uncertainty and reliability analysis methods are probabilistic, where probability distributions are used to represent uncertainty in input parameters. Fuzzy-set or possibility-based methods are another type of uncertainty analysis, that is typically used when there is a lack of information and uncertainties are based upon subjective estimates (Nikolaidis *et al*., 2004; Ayyub, 1998; Ayyub and Gupta, 1997).

No single method is ideal for all problems that may be encountered in compliant MEMS design, since each method has a number of advantages and disadvantages. For example, sensitivity-based methods cannot account for discontinuities in the model and Monte Carlo simulation is too computationally expensive to use with a finite-element model. For this reason, hybrid methods based upon creating surrogate uncertainty models are popular for large-scale problems (many variables) and small-scale problems involving complex FEA models (Wojtkiewicz *et al*., 2001).

A wide variety of software is available for implementing various UA methods, but most of the effort in uncertainty quantification is in developing the parametric model to accurately propagate sources of error and uncertainties. Therefore, toolkits such as DAKOTA (Eldred *et al*., 2002), that treat the model as a "black box" and allow the same model to be used for design and analysis of computer experiments (DACE), optimization, design exploration, and uncertainty quantification studies, have particular appeal for research and development (Giunta, 2002). DAKOTA also takes advantage of the fact that UA and optimization routines involve parallel processes. The idea of using an object-ori-

ented approach to computer simulation is also part of a new design methodology, where automated encapsulations of a streamlined design process are created in order to reduce cycle time and errors in the design and layout of MEMS (Cherry *et al*., 2003).

CHAPTER 3 UNCERTAINTY ANALYSIS FOR ANALYTICAL COMPLIANT MECHANISM MODELS

This chapter presents a generalized uncertainty analysis method for compliant MEMS where models consists of analytical implicit systems of equations. The approach is demonstrated using a micro linear-displacement bistable mechanism, considering the effects of joint clearances, dimensional and material property variations, and friction. The analysis is performed at multiple deflections to estimate uncertainty bands around the force-displacement curve of the mechanism. Effects of joint clearances are minimized by ensuring a forced-closed contact condition through the use of compliant segments. Applying design-stage uncertainty analysis resulted in a functional first-time prototype of a bistable mechanism that can be actuated using a non-amplified thermal actuator.

3.1 Introduction

Reliable engineering design involves the use of uncertainty analysis during all stages of the experimental process. Due to the high cost and slow turn-around during the prototyping stage of micro mechanism design, great advantage can be gained by performing uncertainty analysis during the early design stages.

Joint clearances, variable loading due to friction forces, dimensional variations, and uncertain material properties all contribute to the uncertainty of micro system behav-

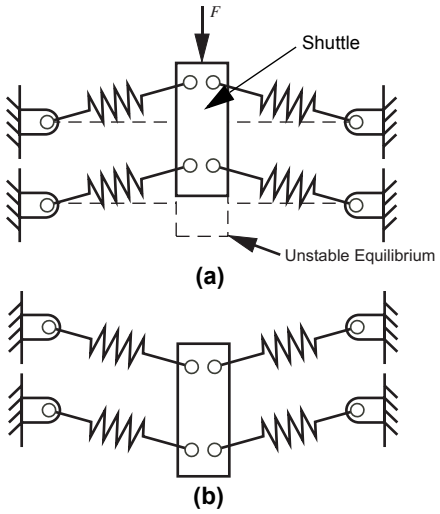

Figure 3.1 Kinematic model for the LDBM showing the (a) fabricated position and the (b) second stable position.

ior. For micro mechanisms, these uncertainties are often relatively large, making it difficult to design functional first-time prototypes.

The purpose of this chapter is to demonstrate how general uncertainty analysis can be used to evaluate the design of a micro linear-displacement bistable mechanism (LDBM) (Baker *et al*., 2000) that must meet certain force-deflection requirements.

Bistable mechanisms have two stable equilibrium positions within their range of motion. They are used in many types of applications, including switches, valves, clamps, hinges, and positioners. Application of bistable mechanisms at the micro level is of interest because the mechanism remains in each position without requiring any input power.

One of the most common bistable mechanism designs involves the use of a compression or tension spring attached to a link that is then toggled between two positions. When the motion of this toggle link is linear, the mechanism is called an LDBM and the link is often referred to as a shuttle. Figure 3.1 shows a schematic of an LDBM that uses

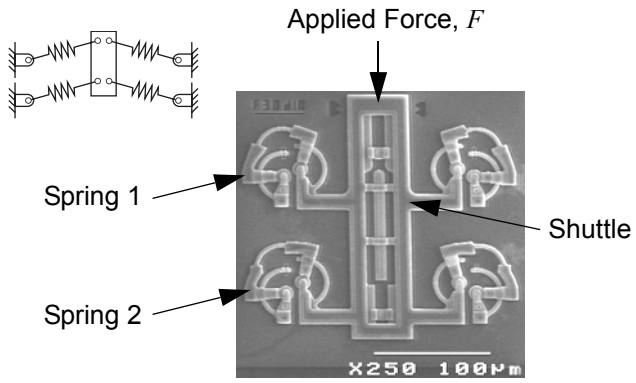

Figure 3.2 A micro LDBM using functionally-binary pinned-pinned segments as springs.

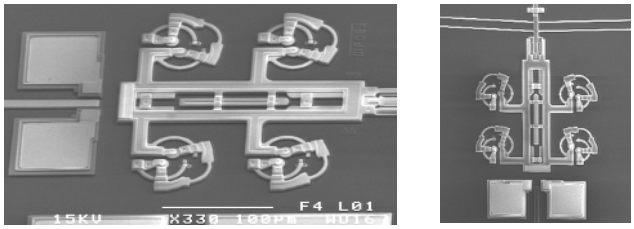

Figure 3.3 An LDBM used as an electro-mechanical switch.

this type of design. The force, *F*, represents an applied force required to move the shuttle. When the shuttle passes the unstable equilibrium position, it will snap to the second stable position without requiring any additional power. The spring function can be achieved using any number of methods employing the elastic deflection of flexible members. The micro LDBM described in this chapter (Figure 3.2) is fabricated using surface micromachining, and compliant functionally binary pinned-pinned segments (Wittwer and Howell, 2002; Howell, 2001) are used as springs.

When the LDBM is used as a precision positioner, a designer may need to estimate the position error in the second stable equilibrium position. Figure 3.3 shows an LDBM being used as an electro-mechanical switch. To ensure an adequate electrical contact, the designer may need to know where to place the contact and be able to ensure a minimum contact force. In addition, there may be a limit on the maximum force required to actuate

the mechanism due to the capabilities of the micro actuator. In all of these cases, estimating the effect of uncertainty on the performance of the mechanism during the design process may not only save time and cost, but will help in designing more robust mechanisms.

Methods for estimating uncertainty for models that are described with explicit functions are well-established (Coleman and Steele, 1999). However, kinematic models such as the one used to model the bistable mechanism in Figure 3.1 are generally systems of equations that are both implicit and nonlinear. Uncertainty analysis of such systems is not a new concept, but the analysis is often avoided during design due to mathematical or statistical complexity.

A method common to tolerance analysis, known as the Direct Linearization Method (DLM) (Chase *et al*., 1995) describes a way to model position error in assemblies using vector loops, that combine to form an implicit system of nonlinear equations. The DLM uses a set of rules for developing correct vector models based upon effects of geometric variation, part tolerances, and dimensioning schemes. These rules provide the guidelines for ensuring that the model can correctly simulate the effects of variation or uncertainty. The DLM has been shown to be useful in the analysis of mechanisms which require uncertainty analysis to be performed for a series of positions (Wittwer, 2001). The mathematical basis of the DLM is simply a matrix form of the error propagation equation used in uncertainty analysis. This chapter presents the DLM in a generalized form that can be applied to a system of equations that involves force and stress in addition to position.

Following the description of the general uncertainty analysis method for implicit systems of equations, some of the main sources of uncertainty in micro mechanisms will

be discussed. The model for the LDBM will then be described, followed by a discussion of the results of the design-stage uncertainty analysis. The analysis is performed at multiple displacements of the shuttle, resulting in error bands around the nominal force-deflection curves. These results can then be used to evaluate the performance of the LDBM in terms of the design requirements.

3.2 Generalized Uncertainty Analysis

The mathematical basis of the Direct Linearization Method is similar to the general uncertainty analysis method described by Coleman and Steele (1999), but the DLM uses matrix notation. Both methods are based upon a first-order Taylor series expansion and use only second-moment statistics. In general uncertainty analysis, the equation that describes the way errors propagate in a model is known as the error propagation equation. This section describes a generalized form of the error propagation equation, where the sensitivity matrix is determined based upon the DLM.

First, let **G** be a system of equations in implicit form

$$\mathbf{G}(\mathbf{u},\mathbf{v}) = [g_1(\mathbf{u},\mathbf{v}), g_2(\mathbf{u},\mathbf{v}), \ldots, g_p(\mathbf{u},\mathbf{v})]^{\mathrm{T}} = \mathbf{0} \tag{3.1}$$

where **u** is a vector of q primary variables, $\mathbf{u} = [u_1, u_2, \ldots, u_q]^{\mathrm{T}}$, and **v** is a vector of p secondary variables, $\mathbf{v} = [v_1, v_2, \ldots, v_p]^{\mathrm{T}}$. Let $\mathbf{S}_u$ be the estimated covariance matrix for **u**. If all elements of **u** are independent, then $\mathbf{S}_u$ is a diagonal matrix, where each element s_{ii} is the variance of u_i. The estimate of the covariance of **v** is found using

$$\mathbf{S}_v = \theta \mathbf{S}_u \theta^{\mathrm{T}} \tag{3.2}$$

which is derived from second-moment statistics and a multivariate Taylor series expansion about the nominal or mean values of **u** and **v**. θ is the sensitivity matrix of size p x q where the elements θ_{ij} represent $\partial v_i / \partial u_j$.

There are numerous ways of obtaining the sensitivity matrix, θ. A common approach is to estimate it using finite-difference techniques. For small systems of equations, where it is possible to obtain partial derivatives of g_i with respect to u_i and v_i symbolically, the procedure used in the DLM is more precise. The sensitivity matrix is found using

$$\theta = -\mathbf{B}^{-1}\mathbf{A} \tag{3.3}$$

where **A** is a matrix of size p x q with elements a_{ij} equal to $\partial g_i / \partial u_j$, and **B** is a matrix of size p x p with elements b_{ij} equal to $\partial g_i / \partial v_j$ (see Wittwer *et al*., 2004).

In uncertainty analysis, it is usually a good practice to describe the model in terms of the most fundamental physical variables in order to ensure that all the primary variables are independent. When this is not possible, Equation (3.2) is still general enough to handle linear correlation between the primary variables. Otherwise, the only additional assumptions in Equation (3.2) are the assumptions made in estimating $\mathbf{S}_u$, such as the distributional forms of the primary variables. A detailed discussion of confidence intervals will not be included in this chapter, so all uncertainties will be reported at one standard deviation.

3.3 Sources of Uncertainty

Current standards for the expression of uncertainty and the methods for detailed uncertainty analysis make use of a differentiation between systematic (bias) error and random (precision) error (ANSI/ASME, 1998; International Organization for Standardization, 1993). Although it is important to distinguish between these two types of uncertainty when performing experiments, in general uncertainty analysis, all errors are grouped together and considered to be random during the early design stages (Coleman and Steele, 1999).

The bistable mechanism described in this chapter was fabricated using the MCNC multiuser MEMS process (MUMPs), a surface micromachining process that consists of three polycrystalline silicon layers (*Poly0*, *Poly1*, and *Poly2*), two sacrificial phosphosilicate glass (PSG) layers (*Oxide1* and *Oxide2*), and a gold metal layer. Further details of the process are described in the *MUMPs Design Handbook* (Koester *et al*., 2001). The remainder of this section describes some of the specific sources of uncertainty that ought to be considered in designing bistable MEMS using this process.

3.3.1 Film Thickness Uncertainty

The growth of the polysilicon and PSG layers is timed and subject to varying operating conditions. Although there is usually negligible variation in thickness from mechanism-to-mechanism on a single wafer, the variability in the operating conditions leads to

significant variation in thickness from wafer to wafer and batch to batch. Table 3.1 shows the target values reported in the *MUMPs Design Handbook* and the estimated process mean μ and process standard deviation σ for each layer. These estimates were based on data from 38 different batches (MUMPs runs 10-47) with sample sizes of about 15.

The estimate of variance for the thickness of each *i*th layer s_i^2 is found by adding the variances corresponding to the systematic and random uncertainties.

$$s_i^2 = \hat{\sigma}^2 + s_{\hat{\mu}}^2 \tag{3.4}$$

where σ is the estimate of the random uncertainty, and $s_{\hat{\mu}}$ is the estimate of the systematic uncertainty or the standard deviation of the process mean.

The flexible beams used in the LDBM are a *Poly1-Poly2* laminate, so the uncertainties combine by root-sum-square to give an overall thickness of $h = 3.5 \pm 0.05$ μm.

3.3.2 Width Variation and Cross-Section Shape

It is important to consider the uncertainty in cross-sectional shape because both the forces and stresses in beams undergoing planar bending are highly sensitive to the in-plane width of the beam. Inspection of beams fabricated using MUMPs reveals that the cross-

Table 3.1 Mean and standard deviation for layer thicknesses in MUMPs (in μm).

Layer	**Target**	$\hat{\mu}$	$\hat{\sigma}$	$s_{\hat{\mu}}$	s_i
Nitride	0.600	0.602	0.022	0.013	0.025
Poly0	0.500	0.505	0.004	0.008	0.009
Oxide1	2.000	2.019	0.055	0.057	0.079
Poly1	2.000	1.990	0.029	0.029	0.041
Oxide2	0.750	0.753	0.021	0.019	0.029
Poly2	1.500	1.500	0.018	0.022	0.028
Metal	0.520	0.506	0.019	0.028	0.034

section of etched polysilicon is trapezoidal rather than rectangular (Sharpe *et al*., 2001; Mirfendereski *et al*., 1993). Although there is some variation in the width due to the irregularities caused by the etch process, the cross-section is fairly constant along the length of the beam.

A detailed analysis for in-plane bending should use the trapezoidal moment of inertia about the vertical axis

$$I = \frac{h}{48}(w_b^3 + w_b^2 w_t + w_b w_t^2 + w_t^3) \tag{3.5}$$

where w_t is the width of the top surface, w_b is the width of the bottom surface, and h is the layer thickness. Sharpe *et al*. (2001) have made measurements of the top and bottom surfaces of beams ranging from 2 to 20 μm in width using TEM images. They found that the bottom surface was generally one micron wider, regardless of the beam width. This implies that the side wall angles may be independent of the width. Using this assumption, a more practical approach is to use optical or SEM images to measure the width of the top surface. The width of the bottom surface can be estimated by assuming an angle for the side wall and using

$$w_b = w_t + 2h\tan\theta \tag{3.6}$$

where θ is the angle of the side wall.

Preliminary measurements have found that the top surface of a *Poly1-Poly2* laminate specified as 3 μm wide results in a width of about 2.45 ± 0.15 μm. Assuming a similar bias for a 4 micron wide beam, the width of the flexible segment for the LDBM will be considered to be $w_t = 3.45 \pm 0.15$ μm. Measurements made from images such as that in

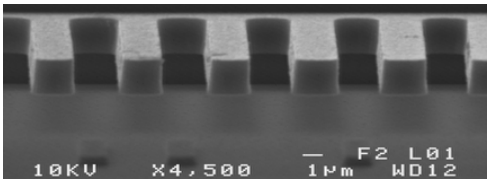

Figure 3.4 SEM image of an array of cantilever beams showing angled side walls.

Figure 3.4 show that the sidewall angle is approximately $\theta = 3.5 \pm 2$ degrees from vertical. These measurements were taken from multiple features on a single wafer, so they do not represent the process mean and standard deviation. Better estimates for the actual cross-sectional shape will be possible as more data becomes available.

3.3.3 Joint Clearances

Joint clearance is one of the largest contributors to position and force uncertainty at the micro level. Many micro system designs are made impractical due to the effects of the joint clearances alone, especially when a system is limited by the force and displacement capabilities of a micro actuator. While extensive work has been done to predict the effects of clearance on the position error of macro machines (Garrett and Hall, 1969; Choi *et al*., 1998), only some attention has been given to these effects at the micro level (Kosuge *et al*., 1991; Sacks and Allen, 1998; Behi *et al*., 1990).

Pin joints created using surface micromachining methods typically have relatively large clearances. The amount of clearance is determined by the thickness of the sacrificial oxide layer (*Oxide2*) that separates the contacting surfaces and is usually defined as the differences in diameters of the hole and pin. Mali *et al*. (1999) found that the thickness of the film coverage of *Oxide2* on vertical sidewalls is approximately 40% of the layer thick-

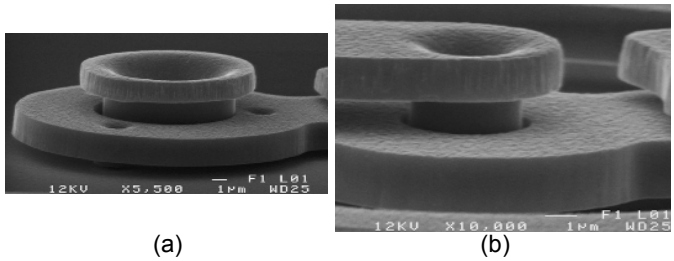

(a) (b)

Figure 3.5 (a) Anchored and (b) floating pin joints showing joint clearance.

ness indicated in Table 1. This means that the nominal half-clearance c is approximately 0.3 µm and the uncertainty of c is correlated with the uncertainty in thickness of *Oxide2*.

Figure 3.5 shows SEM images of a grounded and floating planar revolute joint used in the surface micromachined LDBM. After a mechanism is released (i.e. the sacrificial oxide layers are removed), the links generally fall to the substrate. Not only is there a possibility of rotation out of plane, but the angle of the side walls contributes to the uncertainty in the clearance. Although not reported by Mali *et al*., there is some systematic uncertainty associated with the 40% conformability factor and some random uncertainty due to the surface roughness caused by reactive ion etching of polysilicon (Behi *et al*., 1990). When all these sources of uncertainty are taken into account, the estimate used in this chapter for pin joint clearance in MUMPs is $c = 0.34 \pm 0.06$ µm. Measurements of clearance from images such as those in Figure 3.5 are in general agreement with these values.

3.3.4 Material Property Uncertainty

Uncertainty in material properties often presents a challenge for predicting mechanism performance and reliability. Mechanisms that rely on the force and deflection characteristics of elastic members are particularly sensitive to uncertainty in material stiffness

and fracture strength (Wittwer *et al*., 2002). Polysilicon exhibits a high degree of variation from batch to batch. It is often not practical to determine the exact properties for each batch and therefore material properties can remain a large source of uncertainty.

Sharpe *et al*. (2001) provides a summary of experiments performed by several different groups to determine Young's modulus for polysilicon, and gives a range of values between 135 and 173 GPa. Using three separate approaches, Sharpe *et al*. determined that for design purposes, a conservative value for Young's modulus is $E = 158 \pm 10$ GPa. They also found that specimen size had no significant effect on Young's modulus, but strength increased from 1.21 ± 0.08 GPa to 1.65 ± 0.28 GPa as specimen size decreased. Due to the large discrepancies in reported fracture strengths, a conservative value used in this chapter is $S_y = 1.50 \pm 0.25$ GPa.

3.3.5 Uncertainty Due to Friction

A number of factors contribute to friction in MEMS devices, including viscous drag forces, surface roughness, surface contamination, electrostatic attraction, and van der Waals forces. Though efforts have been made to reduce the causes of friction, it cannot be eliminated entirely and is often difficult to quantify. Lim *et al*. (1990) used polysilicon folded beam structures to measure static friction coefficients, and de Boer *et al*. (1998b) used a hinged microstructure to measure a sliding coefficient of friction. The results for these two experiments were very different, illustrating the wide range of values for friction coefficients depending on surface conditions and experimental environments. In addition to uncertainty in the coefficient of friction, there will also be uncertainty in the normal forces from which the friction force is calculated. This chapter will consider the effects of

friction by representing it as a force $F_{friction}$ that acts in opposition to the shuttle motion. The prediction of the friction force ought to be fairly conservative due to the large variation that is common in MEMS. Based upon prior experience with similar devices, a conservative estimate of the friction force for the LDBM is $F_{friction} = 15$ μN.

3.4 Nominal Force and Position of the LDBM

The first stage in analyzing the LDBM is to develop a model that relates the applied force to the displacement under nominal conditions. This chapter uses a kinematics-based approach to modeling the LDBM, where clearances are modeled using clearance vectors (Choi *et al*., 1998), and linear springs are used to represent the compliant segments. The goal is to develop a system of equations $\mathbf{G}(\mathbf{u},\mathbf{v})$ which can then be used to perform the uncertainty analysis of the complete system. Although the equations will be placed into implicit form, the example used in this chapter does not require a nonlinear solution method to obtain the nominal positions, forces, and stresses.

If the springs on the right side of the LDBM are the same as the springs on the left, then when a force is applied at the center of the shuttle as shown in Figure 3.1, there is no rotation of the shuttle. This symmetry allows a simplification of the model shown in Fig-

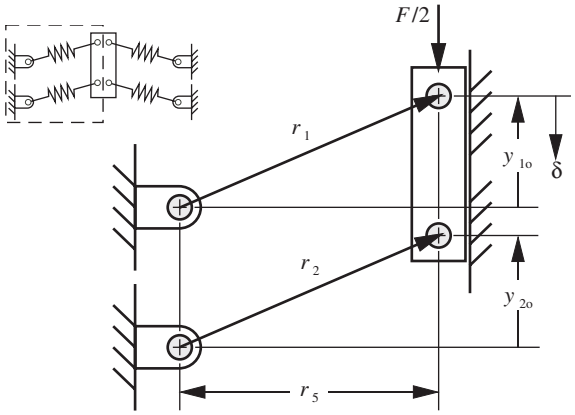

Figure 3.6 Kinematic model for the LDBM in its fabricated position.

ure 3.6, where the applied force for the half-model is *F*/2. The boundary condition on the shuttle is a result of the symmetry and also assumes that the variation in spring constants and dimensions does not lead to any rotation. This assumption is reasonable because the batch-to-batch variation that leads to systematic uncertainty is much larger than the random variation that exists after fabrication of an individual mechanism.

The kinematic model for the LDBM is shown in Figure 3.6, where δ is the displacement from the initial fabricated position, and the initial position is given by r_{1o} = 17.45 μm, r_{2o} = 18.38 μm, y_{1o} = 8.91 μm, y_{2o} = 10.62 μm, and r_5 = 15 μm. These initial values will be considered to be constant because the location of the ideal centers of the holes in the *Poly1* layer are determined by a single mask and the accuracy of the relative placement of different features within a single mask is very precise. The pins are created based on the conformity of the *Poly2* layer within these holes, so the axes of the pins and holes are almost perfectly aligned during fabrication.

3.4.1 Springs

The micro LDBM in Figure 3.2 uses functionally binary pinned-pinned (FBPP) segments, which will be modeled as linear springs. The linear spring constant found using Castigliano's method is

$$k = EI\Phi \tag{3.7}$$

where Φ is based upon the initial shape of the pinned-pinned segment. This value will be treated as a constant in this chapter, but a more detailed description of how Φ is derived can be found in the work by Wittwer and Howell (2002). The main source of uncertainty introduced by Equation (3.7) is the systematic uncertainty due to using the linear spring model for typically nonlinear FBPP segments. This uncertainty is specified as a percent uncertainty. To include modeling error when the error is a percentage as opposed to a fixed value, the spring constant equation is

$$k = \frac{EI\Phi}{1 + p_k} \tag{3.8}$$

where p_k is nominally zero and will be considered a primary variable. If the maximum modeling error is ±5% and this is treated as systematic uncertainty, then the estimate of the standard deviation of p_k is $s_{p_k} = 0.05/2$.

3.4.2 Modeling Clearances

For static analysis of force-closed assemblies and mechanisms, clearance vectors provide an accurate method of considering both the direction that clearances are taken up and the statistical variation in the size of the clearance. The direction corresponds to the

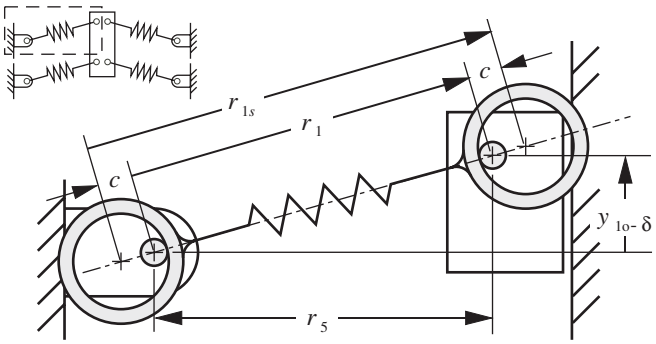

Figure 3.7 Schematic showing how clearance is taken up when a pinned-pinned spring is compressed.

direction of the resultant contact force at the joint. A pinned-pinned segment or link can only support forces along the axis between the two pinned ends. Therefore, the direction of the clearance vectors will always be parallel to the spring vector when the spring is loaded. Figure 3.7 shows how these clearances are modeled for a spring in compression. In compression, the length of the first spring is determined by $r_{1s} = r_1 + 2c$, while in tension, the length of the spring is $r_{1s} = r_1 - 2c$. A zone of contact loss in which the force in the spring is zero can be described mathematically as $r_{1s} = r_{1o}$ when $|r_1 - r_{1o}| < 2c$. Similar equations apply to the second spring as well.

A common method of reducing the position error due to joint clearance is applying a load on the joints such that the joints always maintain contact. For surface-micromachined planar mechanisms, this technique is not possible in the initial fabricated state, but for the LDBM, the position error at the second stable equilibrium position can be reduced by using two or more springs with different initial positions (i.e. $y_{1o} \neq y_{2o}$). This can be

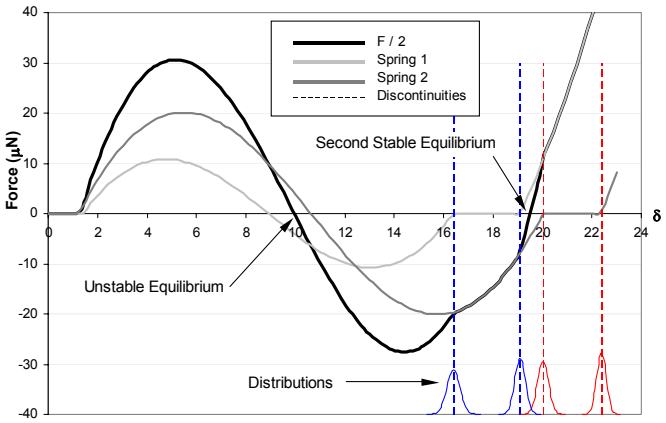

Figure 3.8 Individual and combined force-displacement curves for two different springs.

seen in Figure 3.8, which is a plot of the *y*-component of force applied to the springs as a function of δ. The flat regions in the figure represent the zero-force regions where there is no forced contact in the joints. The plot of the combined force of the two springs, *F*/2, shows that the second stable position does not fall within a zone of contact loss.

For a micro positioner, designing an LDBM to have no contact loss at the second stable position is possible by using statistical interference theory (Rao, 1992) to estimate the variation in the location of the no-contact zones. The displacements at which the points of loss of contact, or discontinuities, occur near the second stable equilibrium position are

$$\delta_{c1} = y_{1o} + \sqrt{(r_{1o} \pm 2c)^2 - r_5^2} \tag{3.9}$$

$$\delta_{c2} = y_{2o} + \sqrt{(r_{2o} \pm 2c)^2 - r_5^2} \tag{3.10}$$

where δ_{c1} and δ_{c2} are the displacements of springs 1 and 2, and y_{1o} and y_{2o} are the initial *y*-positions of the pin joints on the shuttle as shown in Figure 3.6. The variations in the positions of the discontinuities are shown as normal distributions at the bottom of Figure 8. These distributions were estimated using a separate uncertainty analysis of Equations

(3.9) and (3.10) considering the clearance *c* as a normal random variable. The mechanism described in this chapter was designed to ensure that the probability of contact loss in the second stable position was less than 0.27%, which can be seen by the small overlap of the two center distributions.

3.4.3 Stresses

The maximum stress in each spring is an important consideration in design. The equation for the maximum tensile or compressive stress using the linear model is

$$S_{max} = \left|\frac{F_s bc}{I}\right| + \left|\frac{F_s}{A}\right| \tag{3.11}$$

where F_s is the force in the spring, $c = w_b/2$ is the distance from the neutral axis to the outer edge of the beam, $A = h(w_b + w_t)/2$ is the cross-sectional area, and b is a distance based upon the initial shape of the beam (see Wittwer and Howell, 2002). To avoid a completely separate analysis, the stress equations for each spring will be included in the system of equations. The strength-based reliability, or the probability that $S_{max} - S_y < 0$, can then be evaluated during the uncertainty analysis of the complete system.

3.5 Performance Uncertainty of the LDBM

After evaluating the *nominal* performance of the device at a given displacement, we can use the generalized uncertainty analysis method described in Section 3.2 to estimate the *uncertainty* in performance (i.e. the variances for the secondary variables). The

equations developed in the preceding sections must first be placed into a system of implicit equations:

$$g_1 = r_1 - \sqrt{r_5^2 + (y_{1o} - \delta)^2} = 0 \tag{3.12}$$

$$g_2 = r_2 - \sqrt{r_5^2 + (y_{2o} - \delta)^2} = 0 \tag{3.13}$$

$$\begin{aligned} g_3 &= r_{1s} - r_1 + 2c\,\mathrm{sgn}(r_1 - r_{1o}) = 0 \text{ for } |r_1 - r_{1o}| > 2c \\ g_3 &= r_{1s} - r_{1o} = 0 \text{ for } |r_1 - r_{1o}| < 2c \end{aligned} \tag{3.14}$$

$$\begin{aligned} g_4 &= r_{2s} - r_2 + 2c\,\mathrm{sgn}(r_2 - r_{2o}) = 0 \text{ for } |r_2 - r_{2o}| > 2c \\ g_4 &= r_{2s} - r_{2o} = 0 \text{ for } |r_2 - r_{2o}| < 2c \end{aligned} \tag{3.15}$$

$$g_5 = k_1 - (EI\Phi_1)/(1 + p_{k_1}) = 0 \tag{3.16}$$

$$g_6 = k_2 - (EI\Phi_2)/(1 + p_{k_2}) = 0 \tag{3.17}$$

$$g_7 = w_b - w_t - 2h\tan\theta = 0 \tag{3.18}$$

$$g_8 = I - \frac{h}{48}(w_b^3 + w_b^2 w_t + w_b w_t^2 + w_t^3) = 0 \tag{3.19}$$

$$g_9 = F_{s1} - k_1(r_{1s} - r_{1o}) = 0 \tag{3.20}$$

$$g_{10} = F_{s2} - k_2(r_{2s} - r_{2o}) = 0 \tag{3.21}$$

$$g_{11} = \frac{(F - F_{friction})}{2} + F_{s1}\frac{(y_{1o} - \delta)}{r_1} + F_{s2}\frac{(y_{2o} - \delta)}{r_2} = 0 \tag{3.22}$$

$$g_{12} = A - h(w_b + w_t)/2 = 0 \tag{3.23}$$

$$g_{13} = S_{max1} - \left(\left|\frac{F_{s1} b_1 w_b}{2I}\right| + \left|\frac{F_{s1}}{A}\right|\right) = 0 \tag{3.24}$$

$$g_{14} = S_{max2} - \left(\left|\frac{F_{s2} b_2 w_b}{2I}\right| + \left|\frac{F_{s2}}{A}\right|\right) = 0 \tag{3.25}$$

The sgn(x) function used in Equations (3.14) and (3.15) is defined as +1 for positive x and -1 for negative x. There are 14 equations, so **v** consists of 14 secondary variables,

$$\mathbf{v} = [r_1, r_2, r_{1s}, r_{2s}, k_1, k_2, w_b, I, F_{s1}, F_{s2}, F, A, S_{max1}, S_{max2}]^T \tag{3.26}$$

There are 7 primary random variables that form the **u** vector:

$$\mathbf{u} = [E, h, w_t, c, p_{k1}, p_{k2}, \theta]^T \tag{3.27}$$

All other variables in Equations (3.12)-(3.25) are considered to be constants, except for δ, which is the displacement of the shuttle. The values for Φ_1, Φ_2, b_1, and b_2 are 1.474E-5 μm^{-3}, 1.479E-5 μm^{-3}, 44.57 μm, and 44.58 μm, respectively. It is important to ensure that all the values for the primary variables conform to some base unit system. The system used in this chapter is a variation of the mks system which is convenient for micro mechanism analysis, where the units are μm for length, μN for force, and MPa for stress. The nominal values of the primary variables in the **u** vector are

$$\mathbf{u} = [158000, 3.5, 3.45, 0.34, 0, 0, 3.5]^T \tag{3.28}$$

Because the uncertainties are uncorrelated, the only non-zero elements in the primary covariance matrix $\mathbf{S}_u$ are along the diagonal. The diagonal elements are the squares of the standard deviations for the corresponding primary variables. The standard deviations corresponding to the **u** vector can be written as the vector

$$\mathbf{s}_u = [10000, 0.5, 0.15, 0.06, 0.025, 0.025, 2]^T \tag{3.29}$$

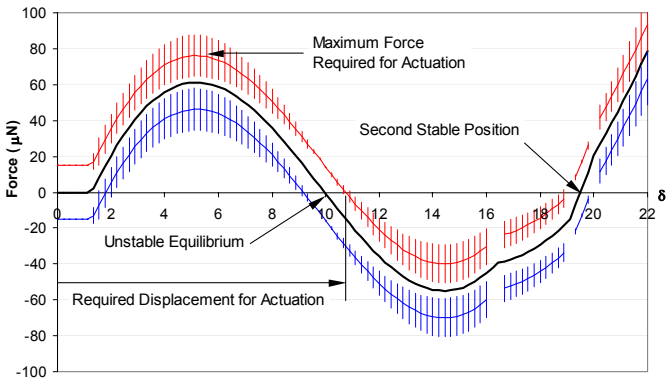

Figure 3.9 Result of uncertainty analysis for the LDBM.

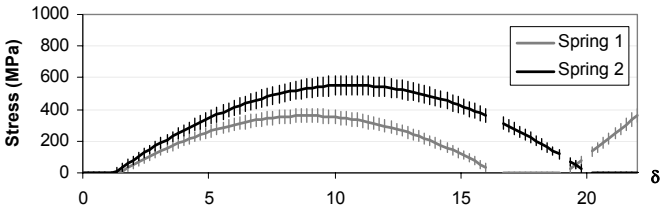

Figure 3.10 Stress vs. shuttle displacement.

The **A** and **B** matrices were formed symbolically to evaluate the sensitivity matrix θ, and the sensitivities were verified using finite-difference. The evaluation of the uncertainty was then automated by incrementing the displacement of the shuttle and using Equations (3.2) and (3.3) to solve for the covariance matrix of the secondary variables at each position.

The result of the uncertainty analysis is shown in Figure 3.9, where a separate uncertainty analysis at incremental values of δ lead to error bands about the nominal force-deflection curves. The heavy line in the center represents the case where the friction force is zero. Friction shifts the curve according to the direction of motion. The upper curve is the force for forward actuation. The lower curve represents the force required to return to the initial stable position. Instead of using an average friction force with uncer-

tainty, a more conservative approach was used, where the maximum expected friction force was assumed to be 15 μN. This was done because the large friction uncertainty masked the effects of the other variations. With the variation in friction set to zero, the error bands in Figure 3.9 are representative of the uncertainty in clearances, dimensions, and material properties. The gaps in Figure 3.9 and Figure 3.10 represent the regions close to the points of loss of joint contact, where the accuracy in the evaluation of the uncertainty is unknown because of the problem of linearizing the system of equations near discontinuities, and the violation of the distribution assumptions.

The graph in Figure 3.9 can now be used to evaluate the performance of the LDBM. Friction changes the location of the unstable equilibrium position, so an actuator must displace the shuttle a minimum of 11 microns; however, this displacement is still within the range of a non-amplified linear-displacement thermal actuator (Cragun and Howell, 1998). The maximum force required to actuate the mechanism occurs at about 5 microns. The force uncertainty is quite large at this position, so a reliable system would require an actuator with an output of about 100 μN or more.

Friction also changes the location of the second stable equilibrium position, which is undesirable for precision positioning. A better way to achieve precise positioning when friction is an issue is to place a stop before the first discontinuity, or around $\delta = 15$ μm.

When the LDBM is used as an electrical switch, the variation in the contact force becomes an important consideration. If a minimum contact force requirement had to be met, the location of the contact most likely to meet the requirement would be at about $\delta = 14$ μm.

The strength-based reliability needs only to be evaluated at the points of maximum deflection of the springs, but including the equations for stress in the overall system makes it a simple matter to obtain the variation at multiple positions. Figure 3.10 shows that the stresses in the springs are well below the fracture strength of 1.5 GPa, even when considering the uncertainty. The probability of failure can be evaluated using the technique described by Rao (1992). Assuming a normal distribution for the maximum stress and the fracture strength, the probability of failure for both springs, or the probability that $S_y - S_{max} < 0$ is less than zero, was lower than 0.27%.

In summary, when applied to the design of the LDBM shown in Figure 3.3, the general uncertainty analysis method helped lead to a successful first-time prototype. Although the friction was somewhat greater than expected, the LDBM was successfully actuated using a non-amplified linear thermal actuator.

3.6 Conclusions

This chapter has demonstrated a generalized uncertainty analysis method applied to a linear displacement bistable mechanism. Adapting the DLM approach using matrix notation results in an efficient method for performing uncertainty analysis for a system of implicit equations. One of the main benefits of this approach is the ability to evaluate the uncertainty of multiple dependent variables simultaneously, such as position, force, and stress. Although the method is simple to apply, the main limitation is that interpretation of the estimated uncertainty near discontinuities is difficult. This example leads to a more general question of what methods ought to be used to automate the error analysis of kinematic models that may involve discontinuous functions.

Finally, the work has shown how the results of the uncertainty analysis can be used to predict the performance of the LDBM. A graph containing the nominal force-deflection curve and the uncertainty bands showed the effects of friction, material properties, dimensional uncertainty, and clearances. These results were used to evaluate design constraints based upon the force required to overcome friction, the force and displacement characteristics of the actuator, or the force required to maintain a closed electrical contact. Using the techniques described, a first-time prototype that pushed the design limits of the MUMPs process was successfully actuated using a non-amplified thermal actuator.

CHAPTER 4 NON-IDEAL BOUNDARY CONDITIONS - MITIGATING EFFECTS OF LOCAL ELASTICITY

It is not always possible to develop analytical uncertainty models like the one described in the previous chapter, so compliant mechanisms are often analyzed using finite-element models. As models become more computationally expensive, uncertainty analysis can become less practical, so much of the work in simulation-based design has to do with investigating non-idealities and identifying ways to simplify the model without making assumptions that lead to significant modeling error.

This chapter discusses the effects of local elasticity in semi-rigid supports and beam segments, focusing on the analysis of monolithic planar compliant mechanisms, which are common components in precision devices and MEMS, such as folded-beam linear suspension springs and micro force gauges (Wittwer *et al*. 2002a; Jaecklin *et al*., 1993; Zhou *et al*., 2001). It is often desirable to use beam elements when modeling compliant mechanisms, but these elements and classical beam theory cannot account for the effects of local elasticity. A method for mitigating the effects of local elasticity in planar compliant mechanisms through the use of optimally sized fillets is presented, which allows beam elements or classical analytical methods to be used without a significant loss of accuracy.

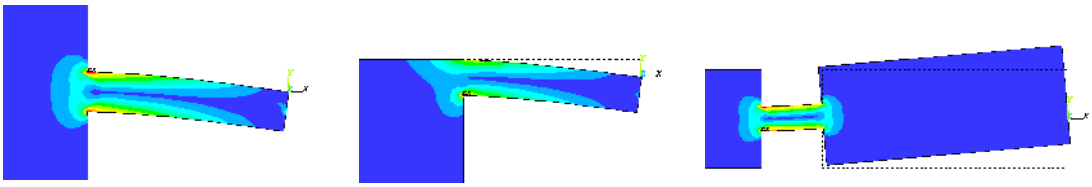

(a) half-plane support (b) quarter-plane support (c) flexure-hinge

Figure 4.1 Stress distribution at the juncture of a flexible beam and (a) an elastic half-plane, (b) an elastic quarter-plane, and (c) semi-rigid segments in series.

4.1 Introduction - Support Elasticity

It is common to assume that flexible members are attached to perfectly rigid supports. However, the seminal works by O'Donnell (1960) and Small (1961) demonstrate through analysis and experiment that the local flexibility at the juncture of a support and a cantilever beam or plate can lead to a significantly larger deflection for a given load. The stress distributions in Figure 4.1 show the local distortion occurring at the juncture of a beam and an elastic support, or a discontinuity in the cross section. To account for this additional deflection, O'Donnell (1963) and Matusz *et al*. (1969) developed flexibility coefficients to use in a variety of classical equations for the deflections and stresses in beams. Recently, Allen and Johnson (2001) considered this effect in the analysis of a micro resonator, since the difference in the spring constant affects the natural frequency of the device. Other recent works have also demonstrated the importance of modeling the elasticity of the support instead of assuming boundary conditions in MEMS (Jensen *et al*., 2001; Kobrinsky *et al*. 2000; Jensen *et al*. 1999a; Gill *et al*., 1998; Meng *et al*. 1993).

This chapter derives a novel approach to the analysis of planar loading of cantilever beams by using appropriately sized fillets to mitigate the effects of local elasticity in the support. It stands to reason that if the local flexibility of the support results in addi-

tional deflection from bending and shear loading, then adding material to the beam in some optimal geometry would provide the additional stiffness to mitigate the effect. It is common practice to use fillets to reduce stress concentrations and improve manufacturability, so the additional stiffness will be applied by optimizing the size of the fillet at the built-in end of the beam.

The optimal fillet radius is specified in terms of a non-dimensional parameter called the *optimal fillet ratio*, ρ*, which is equal to the fillet radius divided by the beam width (r/h). This parameter is shown to be nearly constant for a wide range of beam geometries under predominantly bending loads. This discovery makes it a useful parameter in the design of planar monolithic flexible mechanisms. It enables the designer to use simplified analytical models during design that do not account for localized distortion, while achieving accurate predictions by specifying the appropriate fillet prior to manufacture.

4.2 Determining the Optimal Fillet Ratio

Using Castigliano's displacement theorem for the analysis of an end-loaded rectangular cantilever beam, the vertical deflection, δ, due to an applied moment or shear force are given by the following equations:

$$\delta = \left(\frac{6L^2}{Ewh^3}\right)M = C_{\delta,M}M \tag{4.1}$$

$$\delta = \left(\frac{4L^3}{Ewh^3} + \frac{12(1+\upsilon)}{5Ewh}\right)F = C_{\delta,F}F \tag{4.2}$$

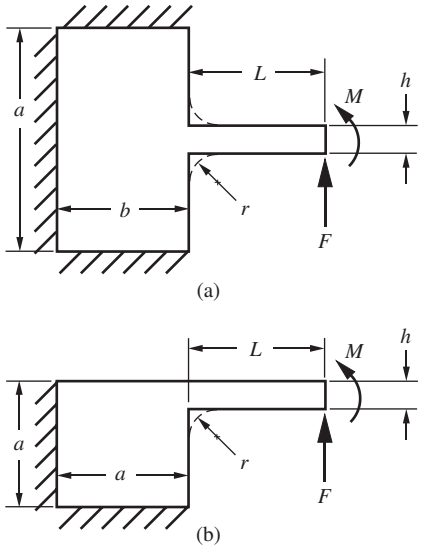

Figure 4.2 Schematics for a cantilever beam attached to (a) an elastic half-plane, and (b) an elastic quarter-plane under moment and shear loading.

where E is the elastic modulus, ν is Poisson's ratio, w is the beam width, h is the beam thickness, and L is the beam length. The general assumptions are that deflections are small, cross-sections remain plane, and the material is linearly elastic, isotropic, and homogenous. For small deflections, the deflection is proportional to the applied force, with a proportionality constant, C, commonly termed the *compliance*, which is the inverse of the *spring constant* or *spring rate*. The subscripts for $C_{\delta, M}$ indicate that the compliance is related to the deflection δ for an applied load M. Note that Equation (4.2) includes the effect of transverse shear, in addition to the deflection due to bending.

The optimal fillet is determined based upon a comparison of Equation (4.1) or (4.2) with the results obtained from finite element analysis of a cantilever attached to an elastic half-space or quarter-space as shown in Figure 4.2. These two geometries represent the most common types of junctures in planar compliant mechanisms, where w is the out-of-plane width. The results are given in terms of an error in the compliance

$\varepsilon = (C - C_a)/C_a$ or spring rate $\varepsilon = (k_a - k)/k$, where the subscript, *a*, refers to the "actual" value as simulated using the FEA model. These expressions are equivalent to the equations below:

$$\text{For a given load, } L\text{: } \varepsilon = (\delta_a - \delta)/\delta \tag{4.3}$$

$$\text{For a given displacement, } \delta\text{: } \varepsilon = (L - L_a)/L_a \tag{4.4}$$

The error ε will often be reported as a percent. The *optimal fillet* is defined herein as the fillet that reduces this error to zero.

FEA models were used to obtain the results and check the sensitivity of the optimal fillet ratio to factors such as plane size, poisson's ratio, material stiffness, transverse shear, beam width, and FEA parameters such as element size and mesh refinement. Although not all of these models are discussed in detail, the following section describes the setup of the primary model used to determine the optimal fillet ratio for mitigating the flexibility at the juncture of a cantilever beam and an elastic half-space and quarter-space under pure bending.

4.2.1 FEA Model Setup

The first stage of the analysis involved determining the appropriate parameters for the FEA models, including element size, mesh refinement, loading conditions, boundary

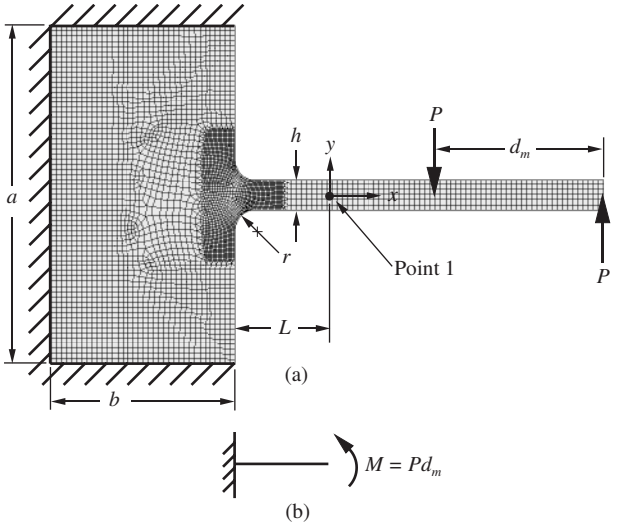

Figure 4.3 (a) FEA model and (b) simplified model for simulating a constant-moment end-loaded cantilever beam of length, *L*, attached to an elastic half-plane.

conditions, etc. This was necessary to minimize the systematic error inherent in the simulation.

Figure 4.3a shows the model used to simulate pure bending at the juncture of the beam and the support. The deflection at the reference point (Point 1) was compared to the vertical deflection of a moment end-loaded cantilever beam with a perfectly rigid support Figure 4.3b. A two-dimensional 8-node structural solid element, which is well-suited to curved geometry, was used in all the FEA models. The plane elements allow only three degrees of freedom, and therefore do not allow application of rotational displacement or moment load. To simulate a moment applied at Point 1, a couple was applied to an extension of the beam far enough from the point of interest so that the local distortions at the application of the forces are insignificant.

To ensure that the loading conditions were appropriate and to determine an appropriate element size, a 2-D model with a rigid boundary condition was compared to Figure

4.3b. Using a mapped mesh with a basic element size of $h/6$ resulted in a systematic error of about $\varepsilon = 0.0003$ or 0.03% using Equation (4.3). Figure 4.3a was therefore determined to be an appropriate model for simulating constant-moment bending between the reference point and the elastic support.

A good approximation to an infinite plane can be achieved using a large finite plane size, a (see Figure 4.3). Following the procedure used by Matusz *et al*. (1969), an appropriate value was determined by increasing the plane size until the sensitivity of the results to the plane size was insignificant. As in Matusz *et al*. (1969), a value of $a/h \geq 5$ was found to be sufficient for the quarter-plane, but the value used in this study was $a/h = 15$ in order to reduce the systematic error to less than 0.1%. A value of $a/h \geq 9$ with $b = (a/2) - h$ was found to be sufficient for the half-plane, but a conservative value of $a/h = 20$ was used. In each model, the mesh was refined around the points of high stress in order to obtain a more accurate determination of the stress concentration factor.

4.2.2 Optimal Fillet Ratio for a Specific Geometry and Loading Condition

As mentioned in the introduction, adding a fillet to the beam can provide the additional stiffness necessary to mitigate the effect of the support elasticity. The two main factors for determining the optimal size of the fillet are (1) the geometry of the beam and the support, and (2) the type of loading.

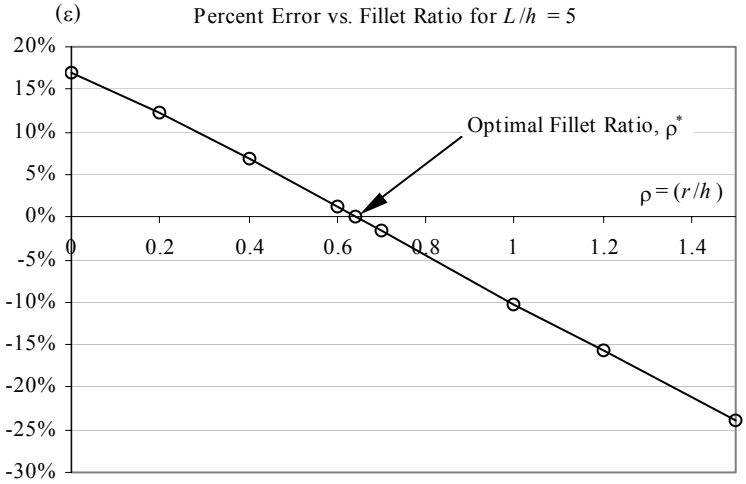

Figure 4.4 Graph of percent error vs. fillet ratio for pure bending of a beam with a specific geometry.

The results for pure bending found that the percent error was only significantly affected by three non-dimensional geometric parameters: the slenderness ratio (L/h), the fillet ratio $\rho = (r/h)$, and the plane size (a/h).

Figure 4.4 shows the results for pure bending of a beam with a slenderness ratio of $L/h = 5$ and where the support has been modeled as an infinite half-plane. The percent error using Equation (4.3) has been graphed vs. the fillet ratio. A positive percent error means that the beam will have a larger deflection than predicted when using Equation (4.1). The point where the line crosses the x-axis is defined as the *optimal fillet ratio*, ρ^*. At this point, the results from the FEA model match the simplified analytical equation.

4.2.3 Results for Moment End-Loading, or Pure Bending

A significant discovery was made when beams with varying geometry were analyzed and compared. For a fixed plane size, the percent error was plotted as a function of

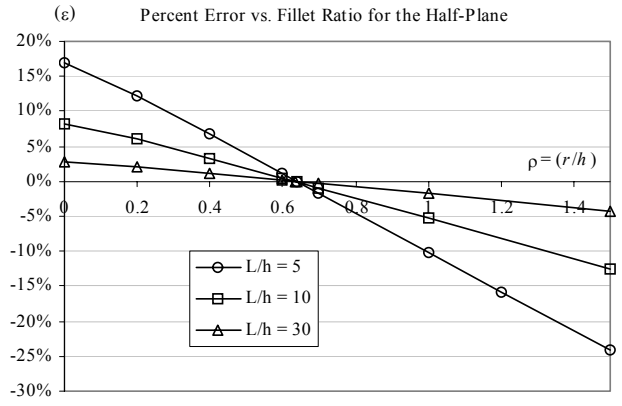

(a)

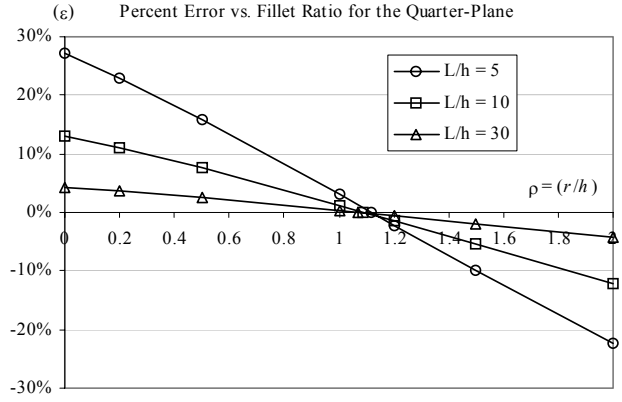

(b)

Figure 4.5 Plot of the percent error vs. the fillet ratio and slenderness for the (a) half-plane model, and (b) the quarter-plane model, under pure bending.

the fillet ratio as in Figure 4.4. Three different geometries were chosen to determine how the percent error varied with the beam slenderness, L/h. Figure 4.5 shows the results of this study for both the half-plane (Figure 4.5a) and quarter-plane (Figure 4.5b) supports. These graphs show that for relatively small fillets, the error due to local elasticity in the support can be highly significant, especially for non-slender beams. The serendipitous discovery was that each of the lines in the plots intersected the x-axis at nearly the same point. Or, in other words, ρ^* is nearly identical for each geometry.

The optimal fillet ratio does have a *slight* dependence on the plane size and the slenderness. Because the optimal values are very similar and the sensitivity to variation is small, a sufficient approach is to use the same fillet ratio for all geometries. Using the graphs in Figure 4.5, appropriate approximations of ρ* for the half-plane and quarter-plane are $\rho_H = 0.64$ and $\rho_Q = 1.1$, respectively. The robustness of these values to changes in slenderness and plane size will be discussed later.

An approximate analytical equation can be developed for the graphs in Figure 4.5, since the individual curves are nearly linear for each value of *L*/*h*. The slopes of these lines are inversely proportional to *L*/*h*. Thus, an approximate analytical equation for representing the error is

$$\varepsilon = c\left(\frac{L}{h}\right)\left[\left(\frac{r}{h}\right) - \rho^*\right] \tag{4.5}$$

where *c* is a constant found through linear regression and is equal to 1.43 and 1.28 for the half-plane and quarter-plane, respectively. It can be seen from this equation that using a fillet ratio (r/h) equal to ρ* will result in zero error.

The geometric stress concentration factor is usually a concern in design for determining both a static safety factor, and for calculating an estimate of the fatigue life. Most charts of geometric stress concentrations are only for fillet ratios below 0.3, since values larger than that result in very small or negligible stress concentrations (Pilkey, 1997). When using the ratios $\rho_H = 0.64$ and $\rho_Q = 1.1$, the results obtained from the finite element model for pure bending show essentially no stress concentration ($K_t = 1.00$). This

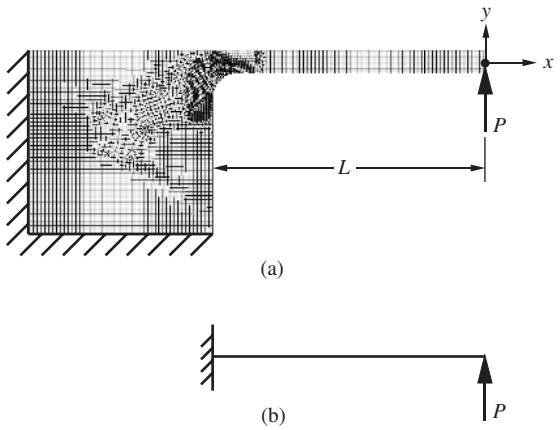

Figure 4.6 (a) FEA model and (b) simplified model for simulating a vertically end-loaded cantilever beam of length, L, attached to an elastic quarter-plane.

shows that not only does using the optimal fillet ratio mitigate the effects of the flexibility of the juncture, but it also practically eliminates the geometric stress concentration.

4.2.4 Results for Vertical End-Loading or Nonuniform Bending

It is common to have both bending and shear loading of beams, so the analysis discussed in the previous section was repeated for the case of a vertically end-loaded cantilever beam. Figure 4.6 shows the FEA model used for the quarter-plane geometry with this type of loading.

The results shown in Figure 4.7 show the same trends as those for pure bending in that the intersections of the lines and the x-axis are nearly identical. The important result from these graphs is that the optimal fillet ratios are all fairly close to the same values as those for pure bending, namely $\rho_H = 0.64$ and $\rho_Q = 1.1$. Combined loading involving bending and shear makes up a large portion of problems in compliant mechanisms analysis, so the fact that the same fillet ratio works to mitigate the effect of local elasticity for

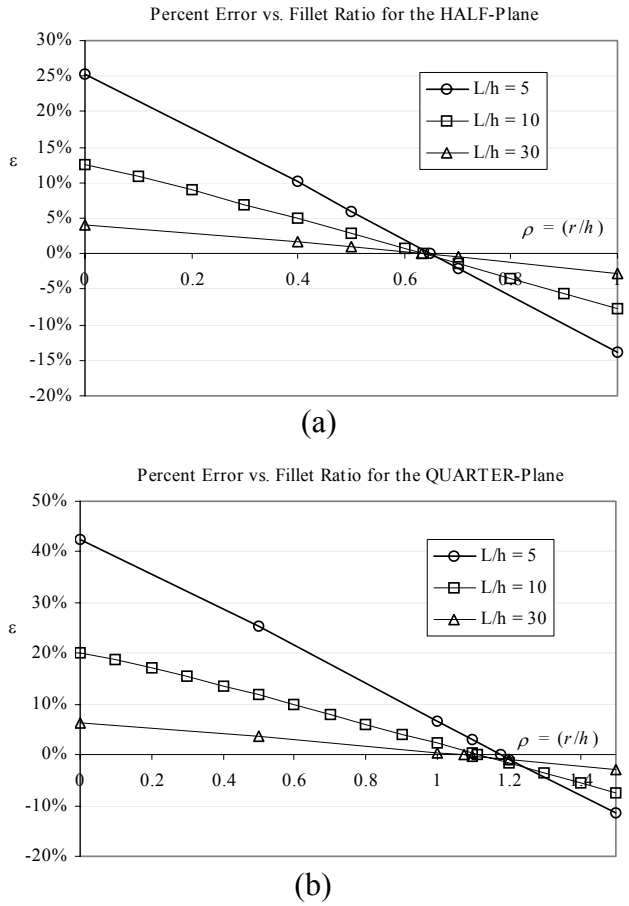

Figure 4.7 Plot of the percent error vs. the fillet ratio and slenderness for the (a) half-plane model, and (b) the quarter-plane model, under nonuniform bending.

both loading conditions is advantageous. In addition, the geometric stress concentration for vertical end-loading was less than 1.06 when the optimum fillet ratio was used.

4.3 Robustness of the Optimal Fillet Ratio

Although in theory there exists a unique ρ* for nearly any loading condition and beam geometry, the application of the approach described in this chapter is based upon using a constant value of ρ for a large class of problems. It is therefore important to determine how robust this approach is with respect to varying loads and geometries.

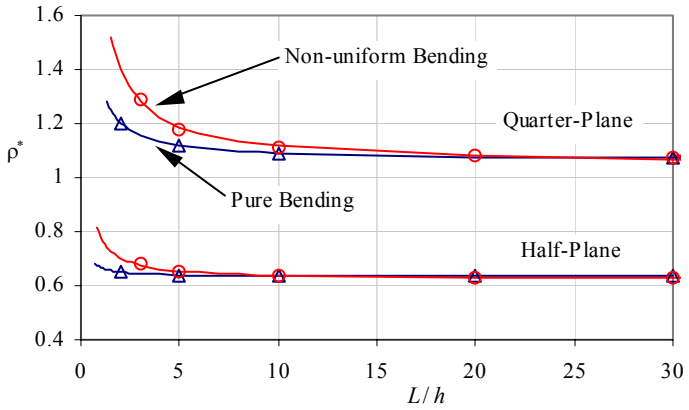

Figure 4.8 Optimal fillet ratio vs. slenderness for different loading conditions of a cantilever beam attached to an elastic half-plane and quarter-plane.

4.3.1 Beam Slenderness

It was mentioned in the previous section that the results of the finite element analysis models show some dependence of ρ* on the slenderness of the beam. This dependence is graphed in Figure 4.8, showing that ρ* is larger for less slender beams. The results for both pure bending (constant moment load) and nonuniform bending (constant shear load) are shown, and it can be seen that the effect of slenderness on ρ* is more evident for nonuniform bending than for pure bending. The optimal fillet ratio was found to be inversely proportional to the slenderness, so the lines in Figure 4.8 represent the regression fit of the FEA data. These graphs are bounded by physical limits for L/h. For infinitely slender beams, $L/h = \infty$. The minimum value for L/h is limited by the size of the fillet, or $L/h = \rho^*$.

The important factor to recognize is that the majority of compliant mechanisms use fairly slender beams, where the value of L/h is greater than 5 and the value of ρ* is

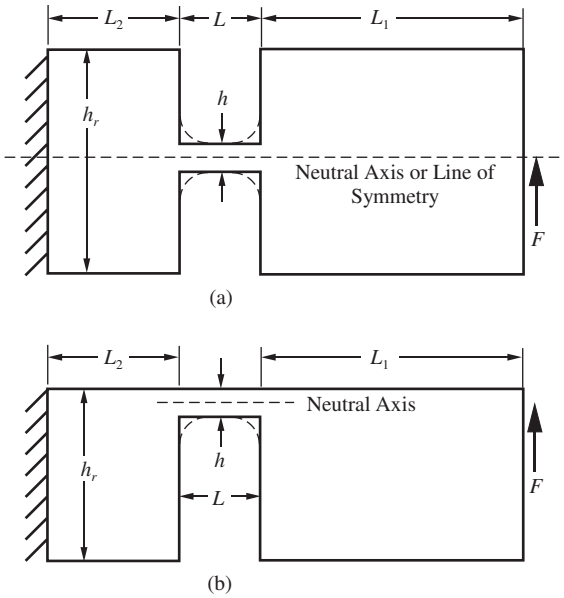

Figure 4.9 (a) Longitudinally symmetric flexure hinge and (b) longitudinally non-symmetric flexure hinge.

nearly constant. In these cases, using the values $\rho_H = 0.64$ and $\rho_Q = 1.1$ will reduce the percent error by at least an order of magnitude and in most cases two orders of magnitude.

4.3.2 Flexure hinges

A large class of problems in which flexible beams will be non-slender are cases where compliant mechanisms implement short flexible segments, called flexure hinges or small-length flexural pivots. These cases represent classic examples of where discontinuities in cross section occur and Castigliano's method cannot account for the localized elasticity at the junctures. Figure 4.9 shows schematics of two common types of flexures, classified as longitudinally symmetric and non-symmetric (Lobontiu, 2003). Although the junctures for these flexures correspond to the half-plane and quarter-plane, respectively, there arises the question of how large the ratio of the thickness of the semi-rigid segment should be to the thickness of the flexible segment (h_r / h). In the design of compliant

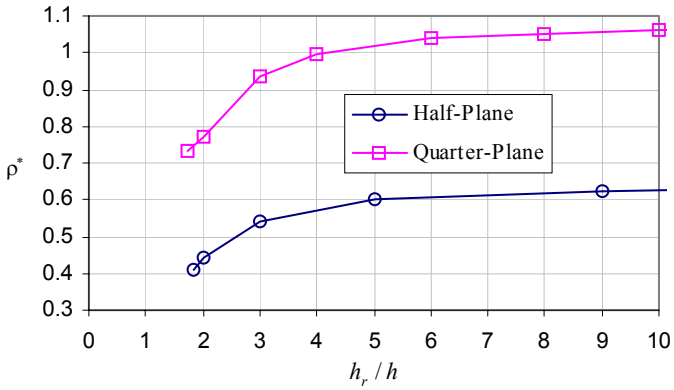

Figure 4.10 Relationship between the optimal fillet ratio and the relative thickness of semi-rigid segments.

mechanisms, this ratio is generally chosen to be large so that the semi-rigid segments can be modeled as perfectly rigid.

To investigate the effect of the thickness ratio h_r/h on ρ*, finite element results were compared to a corresponding beam-element model that did not include the fillets. The relationship between ρ* and the thickness ratio is graphed in Figure 4.10, showing that as the thickness ratio increases, ρ* converges to values close to those chosen earlier ($\rho_H = 0.64$ and $\rho_Q = 1.1$). These results suggest that the same design rule (large h_r/h) used to model the semi-rigid members as perfectly rigid *also* applies to the application of the optimal fillet ratio. From Figure 4.10, an appropriate design rule to apply when implementing the optimal fillet ratio would be to maintain a thickness ratio of $h_r/h > 5$.

The use of flexure hinges and long slender beams attached to flexible supports represent a large class of problems in the design of precision instruments. It is often desirable to use simple analytical equations or rectangular finite beam elements in these cases and

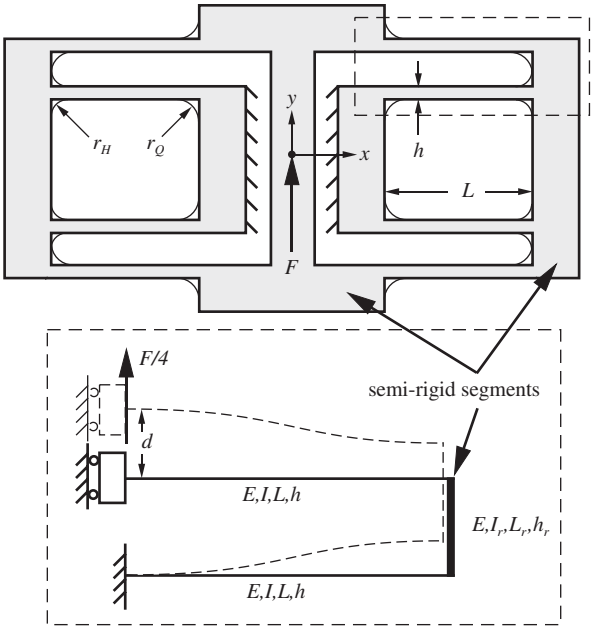

Figure 4.11 Schematic for a folded-beam linear suspension and the simplified model for applying Castigliano's method to obtain the spring constant.

application of the optimal fillet ratio would allow these approaches to be more accurate and would be an important aid in the design of precision mechanisms.

4.4 Example 1

A device used in both precision instrumentation and in microelectromechanical systems (MEMS) is a folded-beam linear suspension (Howell, 2001; Jaecklin *et al*, 1993; Zhou *et al*., 2001). This suspension is based upon the same principles as the compound linear leaf springs described in Jones *et al*. (1951). A schematic for the suspension is shown in Figure 4.11 along with the corresponding simplified model that can be used to obtain the spring constant. This suspension uses a combination of half-plane and quarter-plane junctures. These junctures do not represent beams attached to infinite half-planes or quarter-planes, but as mentioned in the previously section, the method of using optimal fillets is robust to these boundary conditions when the rigid members are over 5 times the

thickness of the beams ($h_r / h > 5$). From Castigliano's method, the compliance of this linear suspension $C_{d,F}$ for a load F and deflection d, applied in the y-direction (see Figure 4.11), is

$$C_{d,F} = \frac{1}{wE}\left(\frac{L^3}{2h^3} + \frac{6(1+\nu)L}{5h} + \frac{L_r}{2h_r} + \frac{3L^2L_r}{2h_r^3}\right) = \frac{1}{k_{d,F}} \tag{4.6}$$

where w is the out-of-plane thickness of the suspension, and the last two terms represent the compliance of the semi-rigid segment as shown in Figure 4.11. It is common to leave the last three terms out of the equation because they contribute little to the compliance; however, they are included here for completeness and to prevent confounding the error with the additional compliance due to flexibility at the juncture. A full model using beam elements was used to validate the assumptions made in deriving Equation (4.6). The percent difference between the beam element model and Equation (4.6) was 0.5%, indicating that the schematic shown in Figure 4.11 is an appropriate simplification of the suspension spring.

Two finite element models were made for the linear suspension. The first was modeled without fillets (Figure 4.12a), and the second was modeled using fillets based upon the values $\rho_H = 0.64$ and $\rho_Q = 1.1$ (Figure 4.12b). The models are simplified using a symmetric boundary condition, which is valid for the given load. The distribution of the stress for these two models can be seen in Figure 4.12, where it is clear that there is

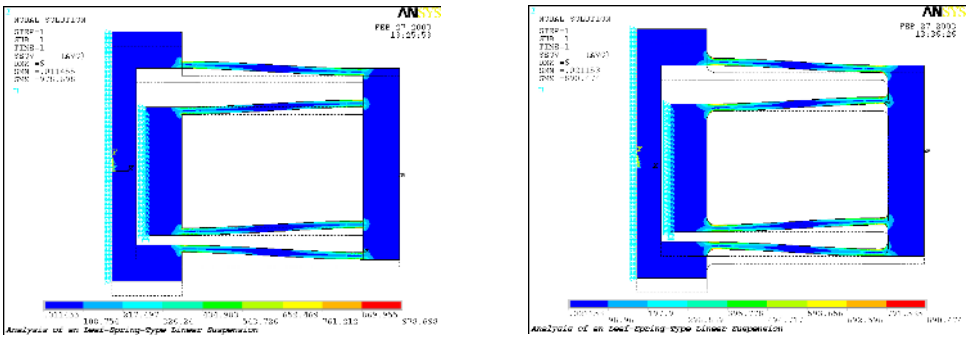

(a) (b)

Figure 4.12 Stress distribution in the linear suspension for (a) the no-fillet model, and (b) the optimal fillet model.

distortion in the semi-rigid segments near the junctures in both models. Adding a fillet does not eliminate local elastic strain, but it does change the compliance or spring constant. These plane-element FEA models, which can account for local elasticity, serve as benchmarks for comparison to Equation (4.6) and the beam-element model. Table 4.1 lists the values of the variables used in this example.

The results for this example are summarized in Table 4.2. Note that the overall spring constant $k_{d,F} = 1/C_{d,F}$ is being compared instead of the compliance since the mechanism is typically used as a spring. The percent error is calculated as $100(k - k_a)/k_a$, where the subscript, a, refers to the plane-element FEA model that is

Table 4.1 Parameter values used in Example 1.

Variable	Value	Units
E	162000	MPa
ν	0.22	- -
w	3.5	µm
L	75	µm
h	3	µm
L_r	9	µm
h_r	18	µm
r_H	1.9	µm
r_Q	3.3	µm

used to simulate the *actual* mechanism. The results indicate that when designing the mechanism using models that can not account for local elasticity, manufacturing the mechanism using the estimated optimal fillet ratios $\rho_H = 0.64$ and $\rho_Q = 1.1$ may lead to insignificant error. If the mechanism were to be made without fillets, the FEA simulation indicates that the percent error would be as much as two orders of magnitude higher. So, instead of building a more complicated analytical model to match the behavior of the real device, physical adjustments can be made to the actual mechanism to make it behave more like the analytical model. In the process, the geometric stress concentrations at these junctures are eliminated through the use of relatively large fillets.

It should be noted that it is the *percent* error that is being reduced, and therefore the benefits obtained from this improved accuracy are dependent on the actual magnitude of the force or deflection. For example, if a spring is being used as a measuring instrument, a large percent error for small forces may be acceptable, but the error for larger forces will of course be amplified. In micro mechanisms, where it is often not possible to separate force and displacement measurement loops, as in the case of micro force gauges (Wittwer *et al*., 2002a), the benefits obtained from improving the accuracy by an order of magnitude can be important.

Table 4.2 Comparison of analytical and finite element results for Example 1.

Model		FEA without fillets (Figure 4.12a)	FEA using estimated ρ* (Figure 4.12b)
	$k_{d,F}$ (μN/μm)	**63.1**	**72.0**
Simplified, Eq. (4.6)	**72.1**	14.3%	0.18%
Beam Element	**71.6**	13.5%	-0.51%

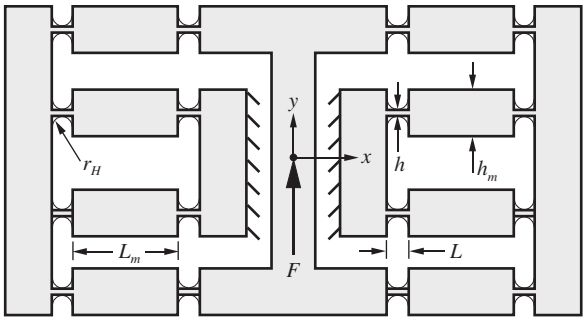

Figure 4.13 Schematic for a flexure-hinge linear suspension spring.

4.5 Example 2

This second example is similar to the linear suspension in Example 1, but it involves a series of flexure hinges instead of long flexible segments. These types of designs are particularly common in ultra-precision machinery, and are called double compound linear springs in Smith, 2000. Most flexure hinges involve half-plane junctures, so the value for ρ used in this example is again $\rho_H = 0.64$.

This example compares the results of plane-element FEA models to two types of simplified equations. A beam-element model was also created for this example, to serve as a benchmark for the analytical equations. The schematic for the flexure-hinge linear suspension is shown in Figure 4.13. The fillets are shown in the schematic to indicate that they will be added when the mechanism is manufactured, but the analytical equations below do not use them. Table 4.3 lists the values of the parameters unique to this example. The variables not specified have values equal to those in Table 4.1 of Example 1.

The first simplified analytical equation is called a pseudo-rigid-body model (PRBM) (Howell, 2001). It assumes that all of the semi-rigid links are perfectly rigid and

models the flexures as pin joints with torsional springs. The compliance equation using the PRBM is:

$$C_{d,F} = \frac{3L(L+L_m)^2}{Ewh^3} \tag{4.7}$$

The second model uses Castigliano's theorem to account for the flexibility of the middle semi-rigid segment (having length L_m and width h_m):

$$C_{d,F} = \frac{1}{wE}\left(\frac{L_m^3}{2h_m^3} + \frac{3LL_m^2}{h_p^3} + \frac{6L^2L_m}{h_p^3} + \frac{4L^3}{h_p^3}\right) \tag{4.8}$$

Table 4.4 shows a comparison of each of the modeling methods to an FEA model that includes the fillet. The results are specified in terms of the spring constant, $k_{d,F} = 1/C_{d,F}$. The simplified analytical Equations (4.7)-(4.8) compared to the beam-element model indicate that very little of the error is due to neglecting bending of the

Table 4.3 Parameter values used in Example 2.

Variable	Value	Units
L	9.65	μm
h	2.5	μm
L_m	55.70	μm
h_m	15	μm
r_H	1.6	μm

Table 4.4 Comparison of analytical and finite element results for Example 2.

Model		FEA without fillets	FEA using estimated ρ*
	$k_{d,F}$ (μN/μm)	**58.3**	**70.3**
PRBM, Eq. (4.7)	**71.7**	23.0%	1.93%
Castigliano, Eq. (4.8)	**70.9**	21.7%	0.87%
Beam Element	**69.8**	19.8%	-0.77%

semi-rigid links. However, the local flexibility at the junctures is a considerable issue in this example as shown by the difference between the two plane-element FEA models. As in the previous example, the FEA simulation that uses optimal fillets closely matches the results from the models that cannot account for local elasticity at the junctures. This implies that an accurate spring constant or compliance factor can be obtained without the need for a complex FEA model, by mitigating the effects of local elasticity through the use of optimal fillets.

4.6 Conclusions

This chapter has presented an approach for mitigating the effects of the local flexibility at built-in ends of beams and flexures using optimal fillets. The *optimal fillet ratio*, ρ^*, was shown to be a useful non-dimensional parameter for the design of planar monolithic flexible mechanisms and structures under predominantly bending and shear loads. It enables the designer to use simplified analytical equations or beam elements in the design, while achieving accurate predictions by implementing the optimal fillet at the manufacturing stage, and eliminating the geometric stress concentration factor. This method applies to planar mechanisms involving half-plane and quarter-plane junctures which are common in a large number of problems in flexible mechanisms. The examples demonstrated that the percent error can be reduced by as much as two orders of magnitude, compared to the case where the effects of fillets and local elastic deflections are neglected.

CHAPTER 5 SIMULATION OF NON-IDEAL THERMAL MICROACTUATOR PERFORMANCE

The previous chapter discussed the importance of considering the elasticity of supports and semi-rigid segments in the design of compliant mechanisms. Other common modeling assumptions for finite element models involve symmetry and loading conditions. This chapter describes the effects of asymmetry and non-ideal loading on the behavior of chevron-shaped thermal in-plane microactuators.

Predicting the force capabilities of thermal microactuators is a key issue when designing to meet specific size and power requirements. In this chapter, simulation and experimental results show that a significant decrease in performance can occur for some designs due to non-ideal buckling, which may be caused by an offset load or process variations that lead to asymmetry. Nonlinear finite element models are used to simulate the behavior, provide predictions of the force output capability, and develop design rules for mitigating the effect of non-ideal buckling.

5.1 Introduction

Thermal microactuators can provide larger forces and greater deflections than other devices of similar size that use piezoelectric, magnetic, and electrostatic actuation.

High forces combined with low drive current and low voltage makes thermal actuation particularly useful for compatibility with CMOS circuity (Reid *et al*., 1996). Thermal actuation has been used in a number of applications including linear micromotors (Maloney *et al*., 2004), precision micropositioning (Chu and Gianchandani, 2003), microgrippers (Comtois and Bright, 1997), microrelays (Gomm *et al*., 2002), bistable switches (Baker and Howell, 2002), and optical-fiber switches (Comtois and Bright, 1997).

Two main topologies for in-plane thermal actuators are the heatuator or bimorph design (Comtois and Bright; 1995) and the chevron or bent-beam design (Cragun and Howell, 1999; Que *et al*., 1999), both of which can be grouped into arrays to provide higher output forces. Sinclair and Wang (2003) provide a description of these two topologies, and describe the chevron-shaped actuator as more efficient since "all bending beams are force-producing, even when they are arrayed to increase output force".

Force measurements are usually obtained through *in-situ* force testers which consist of anchored beams or springs. Reid *et al*. (1996) provided experimental force data related to the bimorph thermal actuator configuration using cantilever beams rigidly supported on one end that pointed to an indicator to provide amplification of the displacement. Cragun and Howell (1999) used a compliant parallel guiding spring anchored to the substrate which deflected under the force applied by a chevron-shaped thermal actuator. Others (Maloney *et al*., 2004; Que *et al*., 2001; Park *et al*., 2001; Sinclair, 2000; Jonsmann *et al*., 1999; Que *et al*., 1999) have used similar approaches, but experimental data has been limited, often due to the fact that the springs are too soft to determine the true actuator capability. Recently, Lai *et al*. (2004) used an acupuncture needle with known stiffness

attached to a positioning stage to obtain *ex-situ* force measurements by measuring the deflection of the needle. The advantage of this approach was that measurements could be made on a single actuator at multiple power levels.

When fixed or anchored load springs are used for force measurements, a single test setup can only provide one data point at each input power level, resulting in a single load-line. In order to fully characterize a particular design, an array of tests needs to be fabricated in which the stiffness of the spring is varied, but creating an array of test structures introduces uncertainties having to do with variations in geometry between different actuators. Sinclair and Wang (2003) describe the use of a variable-length cantilever beam to change the stiffness of the load spring, but if the beam is stiff enough to measure peak output forces, the deflection of the beam may be too small to measure accurately. An alternative method is to use a single movable *in-situ* force gauge (Wittwer *et al*., 2002a) designed to measure the full range of force of an actuator at multiple power levels.

The purpose of this chapter is to characterize the force capabilities of chevron-shaped thermal microactuators through simulation and experiment. Force measurements are obtained using a novel approach that includes both anchored spring tests and *in-situ* force gauge measurements. Non-ideal buckling is shown to cause reduced performance as compared to ideal conditions. This may be caused by non-ideal loading or asymmetry due to process variations. Nonlinear finite element models are used to simulate the behavior, provide predictions of the force output capabilities, and determine design rules for mitigating the effect of non-ideal buckling.

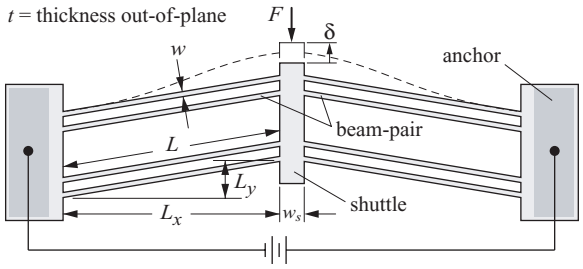

Figure 5.1 Schematic of a thermal in-plane microactuator with 4 beam-pairs.

5.1.1 Thermal Microactuators

Figure 5.1 shows a schematic of a thermal in-plane microactuator (TIM). The device can be fabricated with a single layer of material of thickness t, although in surface micromachining, laminated layers are often used to increase the aspect ratio. A current is passed through the legs of the TIM and the beams expand due to Joule heating and since the beam-pairs are fixed at both ends, buckling occurs. The initial angle of the beams determines which direction the center shuttle moves as the legs buckle, and a large aspect ratio (t/w) ensures that only in-plane buckling occurs. This creates a lateral displacement δ of the center shuttle which can provide an in-plane actuation force F.

Predicting the unloaded output displacement of the actuator for a given input current is a complicated heat transfer problem in which the temperature distribution is not uniform (Sinclair and Wang, 2003; Lott *et al*., 2001). When predicting the force output via simulation, it is possible to decouple the heat transfer problem from the structure model by assuming a constant thermal strain. A nonlinear finite element model can then be used in which a thermal strain is first applied, followed by an incremental displacement back to the zero-strain position, generating a force vs. displacement curve.

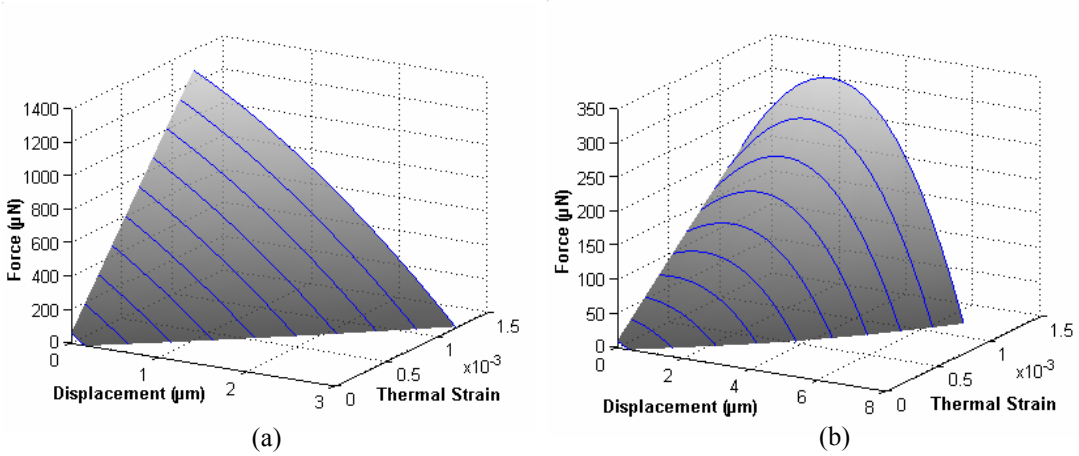

Figure 5.2 Force equilibrium surface for a TIM with (a) a large initial offset and (b) a small initial offset.

Figure 5.2 shows graphs of the predicted force capability of a thermal actuator in which the surface represents the force equilibrium at specific displacements and thermal strains. The surface, created using multiple force-displacement curves, provides a full characterization of the force output of the powered actuator. The designs characterized in Figures 5.2a and 5.2b have initial offsets of $L_y = 2.5$ μm and $L_y = 15$ μm, respectively. There is a distinct trade-off between displacement and force as the initial offset is increased. Adding more leg-pairs can increase the magnitude of the output force without changing the displacement, but this also results in higher power requirements (Cragun and Howell, 1999; Lai *et al*., 2004).

The thermal strain is controlled by changing the current across the beams, but a limit is reached where the legs become so hot that material properties are adversely affected and the TIM becomes permanently damaged or warped (Sinclair and Wang, 2003). Even with zero thermal strain, there is some amount of displacement in chevron-shaped thermal actuators due to the residual stress inherent in surface micromachining of

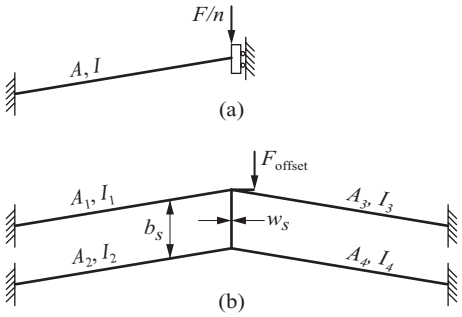

Figure 5.3 Finite element model for (a) ideal loading conditions and (b) an offset load and asymmetry.

polysilicon or the fabrication of other materials. This is not surprising, since similar devices have been used as strain sensors (Gianchandani and Najafi, 1996). A compressive stress of 10 MPa has been used in these simulations.

5.1.2 Model Description

A nonlinear structural finite element model is used to analyze the force output of the TIM. Beam elements were used that take the moment of inertia (I) and cross-sectional area (A) of the beams as inputs. When ideal loading conditions and symmetry apply, a simplified model shown in Figure 5.3a is used. With this model, the force output is a multiple of the number of beams (n) in the actuator. Ideally, using more than one beam-pair prevents rotation of the shuttle, leading to a higher-order buckling mode that can provide larger output forces. In order to take into account non-idealities such as an offset load or asymmetry, the full model shown in Figure 5.3b is used, where b_s is the spacing between the beam pairs and w_s is the width of the shuttle.

The model is exercised on two main designs that are summarized in Table 5.1. The two actuators were designed to have approximately the same maximum forces by adjust-

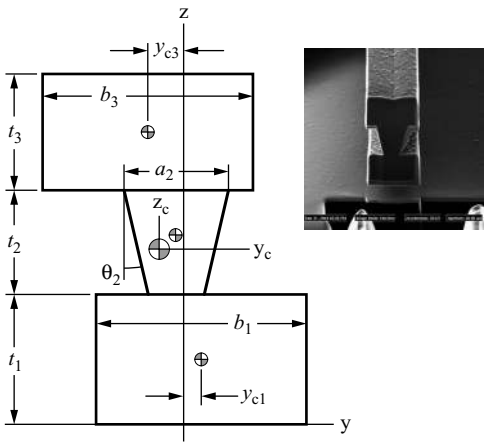

Figure 5.4 Cross-section of a thermal actuator I-beam.

ing the beam length ($L = \sqrt{L_x^2 + L_y^2}$), width (w), and vertical offset (L_y). The beam angle (α) for the two designs are similar. The main difference is the beam slenderness, or the ratio of the length to the width (L/w). The actuators were fabricated using the SUMMiT V™ surface micromachining process (Sniegowski and de Boer, 2000).

In addition to the design variables that describe the topology in Figure 5.1, the beam cross-section geometry is also important. Figure 5.4 shows a schematic of the cross-section of the beam legs. In order to prevent the TIM from deflecting or buckling out-of-

Table 5.1 Parameter values.

Variable	Design I	Design II
L_x (μm)	300	200
L_y (μm)	3.5	2.5
t (μm)	6.95	6.5
w (μm)	3.8	3.8
α (degrees)	0.716	0.668
L/w	52.6	79.0
b_s (μm)	80	80
w_s (μm)	10	10
E (MPa)	164000	164000
v	0.23	0.23
S_r (MPa)	-10	-10

plane, an I-beam shape was used. This was done by connecting two layers using a via (etching the sacrificial oxide layer). For Design I, these two layers are Poly12 (Poly1-Poly2 laminate) and Poly3 and in Design II, the two layers are Poly3 and Poly4. No data has been published regarding the shape of the web, but based upon measurements of images obtained using a focused ion beam as shown in Figure 5.4, the angle of the side-wall in the web (θ_2) is approximated as 10 degrees. A summary of the other nominal dimensions used for designs I and II are given in Table 5.2.

Variations in the cross-sectional geometry occur during the fabrication process that can affect the model uncertainty. The area and moment of inertia are affected by variations in line widths, layer thicknesses, mask alignment, and the slope of the sidewalls for the web. At the device level, these variations are often correlated so that they affect each beam similarly, but there may also be some degree of variation between the geometry of different beams (and possibly even within the same beam). The full model assumes that each beam has a constant cross-section, but it allows each beam to have a different area and moment of inertia in order to investigate the effects of small variations between beams, as discussed later.

Table 5.2 Cross-section parameter values.

Variable	Design I	Design II
t_1 (μm)	2.5	2.25
t_2 (μm)	2	2.2
t_3 (μm)	2.25	2.25
$y_{c1}=y_{c2}=y_{c3}$	0	0
b_1 (μm)	3.8	3.8
b_3 (μm)	3.8	3.8
a_2 (μm)	2	2
θ_2 (degrees)	10	10

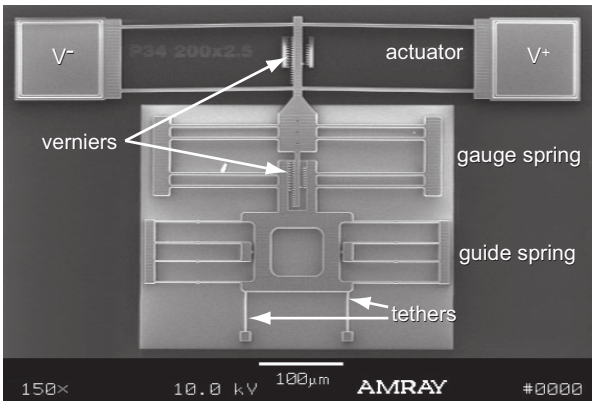

Figure 5.5 Scanning electron micrograph of a thermal actuator with an *in-situ* force gauge attached.

5.2 Force Measurement

A new test approach is proposed to obtain experimental force data. A dual stage *in-situ* force gauge is introduced that performs the functions of both a fixed load spring and a movable force gauge. This allows both load-line and force-curve testing on the same device, eliminating device-to-device uncertainty in the measurements. Figure 5.5 shows a scanning electron micrograph of one of the designs used in our experiment with a dual stage force gauge attached. The gauge acts as an anchored spring when the tethers are in place and as a movable force gauge after the tethers are broken. Verniers on both the thermal actuator and gauge are used to obtain displacement measurements in increments of 0.33 μm. An additional guide spring was used to help keep the force gauge off the substrate and to help prevent laterally applied forces from manually manipulated probes.

The first stage of the testing was to gather data using the load-line approach before the tethers were broken. Each load-line test consisted of applying a specific current across the TIM and recording the displacements from each vernier. These tests were found to be highly repeatable within the accuracy achievable with the verniers.

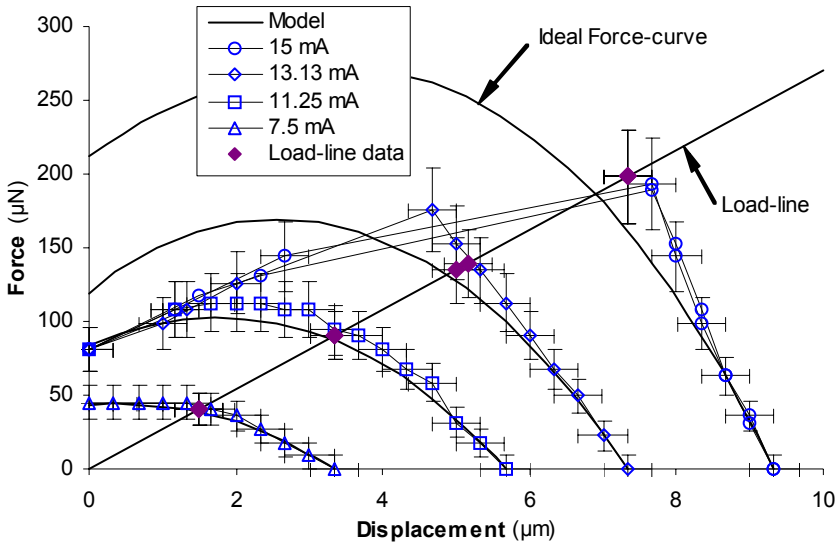

Figure 5.6 Force measurement results for Design I compared to the ideal model.

The second stage involved a series of force-curve tests using the movable force gauge. Each test was run using a different current level, beginning with the highest current level and stepping down. After applying a current, the force gauge was positioned such that the vernier on the gauge read zero. This represented the unloaded displacement of the TIM. The gauge was then moved incrementally to obtain force measurements at each 0.33 μm increment of displacement of the actuator, similar to the way in which the force curves are generated using the finite element models.

The results of the tests for Design I are shown in Figure 5.6, along with the ideal-model (Figure 5.3a) predictions. The significance of this graph is that all the tests come from a single device using a single gauge, providing data that is not subject to device-to-device variation. The error bars on each of the data points represent the 2-sigma (95%) uncertainty resulting from vernier measurements and the dimensional and material prop-

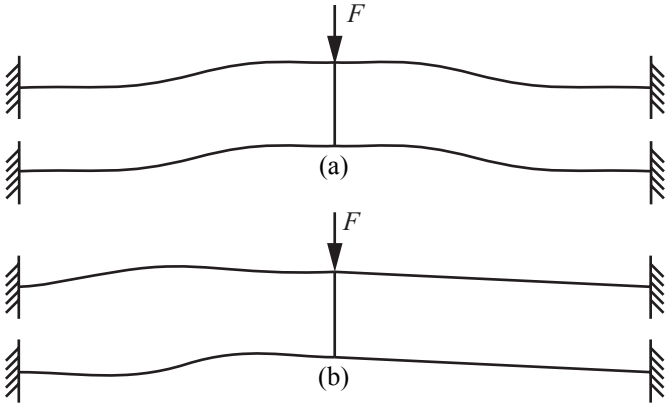

Figure 5.7 Schematics showing (a) ideal buckling and (b) non-ideal buckling of a thermal actuator.

erty uncertainties in the force gauge, as explained in Wittwer *et al*. (2002a). The thermal strain used in the model is based upon the measured unloaded displacement.

After performing the test at the lowest current level (7.5 mA), the test was repeated at the highest current level (15 mA). This test was conducted to ensure that the length of time involved in gathering the data, the high temperatures, and high stress in the actuator did not result in permanent deformation and a resulting shift in the data. The test verified that there was no significant shift in the data, making it possible to perform multiple tests on the same device. Also, it is encouraging to note that the results of the load-line tests correspond well to the force-curve tests.

The force-test data in Figure 5.6 shows a significant difference in performance from that predicted by the ideal model. The difference was hypothesized to be caused by the beams buckling in a non-ideal manner, a visibly noticeable phenomenon that was also observed by Cragun and Howell (1999) for actuators with long beams. An example of a non-ideal buckling mode is shown in Figure 5.7. Non-ideal buckling was observed in pre-

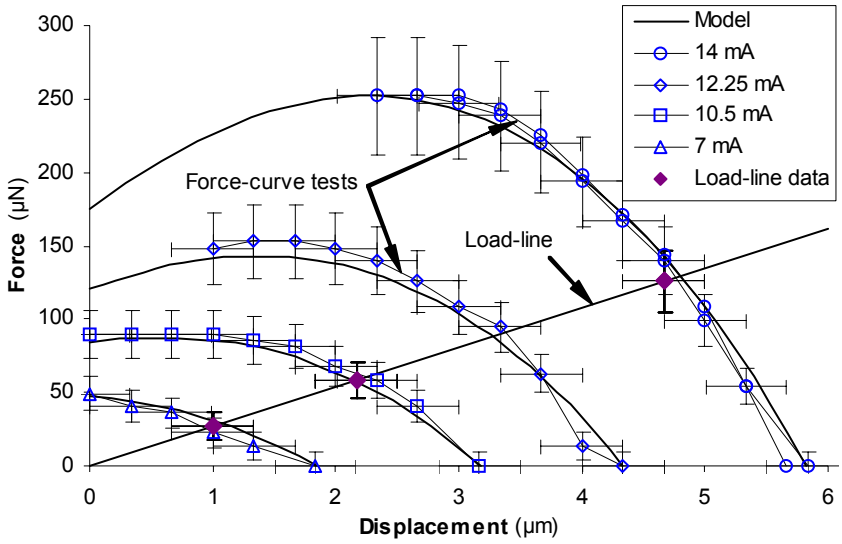

Figure 5.8 Force measurement results for Design II compared to the ideal model.

vious tests and was the cause for including the guide spring (Figure 5.5) to help prevent non-ideal loading conditions that might cause the shuttle to rotate.

The test results for Design II in Figure 5.8 do not show the same non-ideal buckling phenomenon. This data provides evidence that the ideal behavior can be achieved. The following section addresses the development of models that predict the non-ideal behavior, with the goal of identifying ways to prevent or mitigate non-ideal buckling.

5.3 Non-Ideal Buckling

The two main factors that we predicted to be probable causes of the instability of the actuator were non-ideal loading conditions and asymmetry due to variations in geometry. After developing models to simulate the behavior of the actuator under these conditions, an investigation of the effects of design parameters led to identifying a design rule for preventing non-ideal buckling.

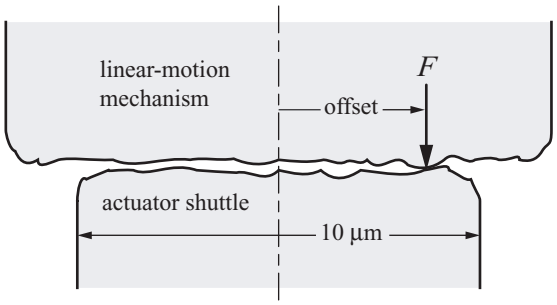

Figure 5.9 Roughness of the contact surface resulting in an offset load.

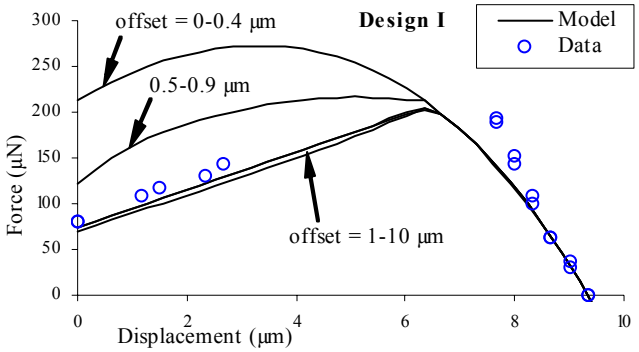

Figure 5.10 Comparison of offset-load simulations and experimental data for Design I.

5.3.1 Effects of Non-Ideal Loading

Non-ideal loading conditions can occur during testing if lateral forces are introduced as the force gauge is moved, but the non-ideal buckling phenomenon was also observed when Design I was used to push on a linear-motion mechanism. The width of the shuttle is 10 µm, so when used to actuate another device, it is possible that small variations in the contacting surfaces as shown in Figure 5.9 could lead to a load offset of up to 5 µm. Therefore, we performed simulations using the full FEA model (Figure 5.3b) to investigate what effects an offset load could have on the force curve.

Figure 5.10 shows a comparison of simulations for Design I in which the offset is increased from zero (the ideal curve) to 10 µm. The measured data is included to show

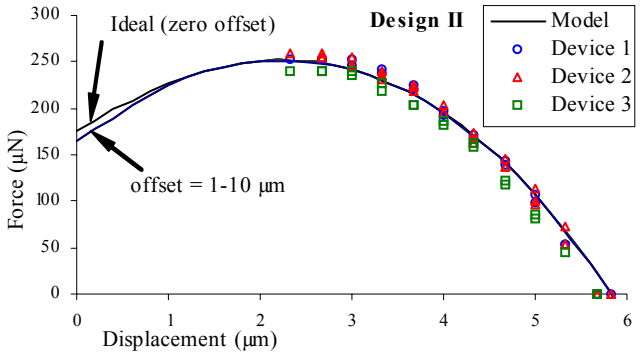

Figure 5.11 Comparison of offset-load simulations and experimental data for Design II.

how the simulation more closely matches the experimental results. The offset causes some rotation of the shuttle due to the moment induced by the off-axis load, but the shape of the force curve is mostly dependent upon the buckling mode, causing a discrete difference between the shapes of the curves rather than a gradual shift in the curve as the offset is increased. These simulations demonstrate that the ideal force-displacement curve can be fairly difficult to achieve because even a small offset of 1 µm can result in the lower, or worst-case performance curve. Therefore, off-axis loading is a plausible cause for the buckling observed in testing Design I. To avoid the possibility of applying an offset load due to surface roughness variation, it may be better to use a pointed rather than flat contact surface.

The offset-load simulation was performed using Design II, and the results in Figure 5.11 show that the difference between the ideal and worst-case force-displacement curve is much smaller than for Design I. Force tests were performed at the same current level (14 mA) on two additional devices at different locations on the wafer to help validate the model. In each case the peak actuation force was close to the model prediction.

5.3.2 Effects of Asymmetry Due to Process Variations

In addition to loading conditions, the maximum force capability of the actuator depends in large part on the symmetry of the device. Another possible reason for non-ideal buckling might be the asymmetry caused by small variations in the cross-sectional geometry of different beams. Mask alignment combined with edge bias variation can result in a change in beam width and a shift in the centroid (y_{ci}) of each individual layer. The geometry of the web may also vary somewhat between different beams. Little data is available to determine the statistical distributions for variations at the device level, so the purpose of this simulation is to use reasonable estimates of the uncertainties and determine whether small deviations could be a factor in affecting the stability of the TIM.

A Monte Carlo simulation was run to simulate the effects of random variation in the beam legs within a reasonable expected tolerance. The widths of the layers (b_1, b_2, a_2) were allowed to vary by ±0.05 μm. The angle of the sidewall of layer 2, θ_2, was allowed to vary by ±2 degrees. The shift in the individual centroids, y_{ci}, for each layer was allowed to vary by ±0.05 μm.

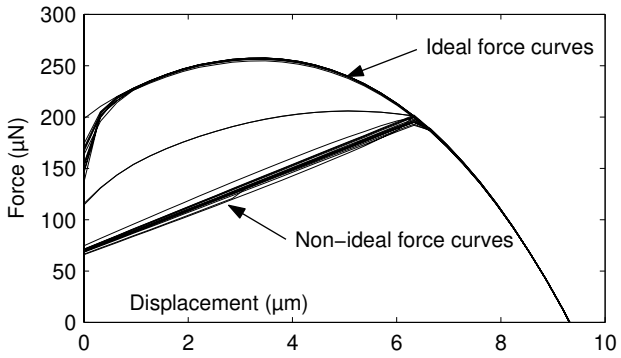

Figure 5.12 50 random force curves generated via Monte Carlo simulation for Design B.

Figure 5.12 shows the results of 50 simulations for Design I at the maximum power level tested in Section 5.2. 50% of the simulations resulted in the lower force curve, indicating that variation in beam geometry is also a plausible cause for the non-ideal buckling behavior in the actuators. The results of the Monte Carlo simulation show the same discrete steps in the force curve as in the offset-load model. Therefore, when designing a thermal actuator, it may be sufficient to use the offset-load model to determine the worst-case force curve.

It is usually assumed that increasing the spacing between the beam-pairs will increase the stability of the TIM. While it is true that using multiple beam-pairs helps prevent rotation of the shuttle due to lateral loads or moments, the Monte Carlo simulation shows that even with no offset load or moment, small differences in beam geometry can lead to non-ideal buckling modes.

5.3.3 Effects of Design Variables

The difference between the effects of non-ideal buckling in Designs I and II led to the hope that certain design variables could be identified that govern the behavior. Exten-

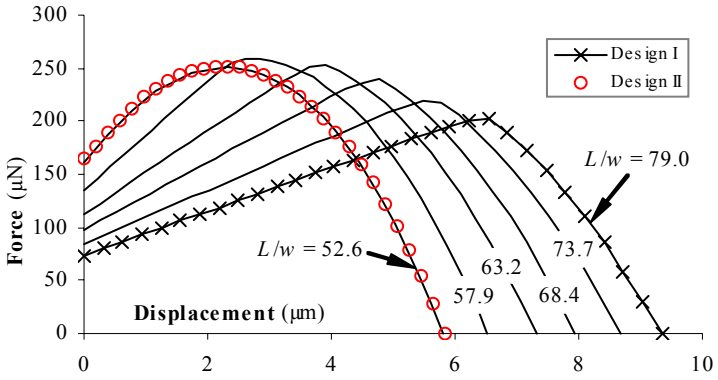

Figure 5.13 Effect of beam slenderness on worst-case buckling (via simulation).

sive simulations were run to investigate various design changes, such as changing the initial angle, the spacing between beam pairs, and the beam length. At first, it was thought that a metric for the stability of the device would be the distance of the load offset for which non-ideal buckling was first observed. However, simulations[1] suggested that the ideal buckling mode requires nearly zero offset for some designs and it is therefore wise to assume the worst-case scenario when using such designs for high-force applications.

Fortunately, a geometric design variable was identified as the most important factor contributing to the difference between the stability of Design I and II. Perhaps not surprisingly, this variable was the beam slenderness ratio, a common non-dimensional parameter in columnar buckling problems (Gere and Timoshenko, 1997). The slenderness ratio, *L*/*w*, is 79.0 and 52.6 for Designs I and II, respectively. Figure 5.13 shows the effect of the beam slenderness on the shape of the force-displacement curve of Design I with an offset load of 10 μm. The slenderness is decreased incrementally by changing the length

1. For a given offset load, the convergence of the nonlinear finite element solution at the bifurcation point is usually what determines the specific buckling mode. Therefore, the resulting buckling mode is highly dependent upon the number of load steps. Increasing the number of load steps can result in non-ideal buckling being observed at a smaller offset.

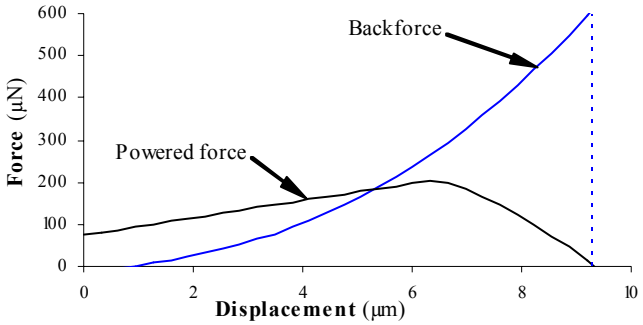

Figure 5.14 A comparison of the backforce and the powered force for Design I with a load offset of 10 μm.

of the beam while holding the beam angle and all other parameters constant. When the slenderness ratio for Design I is the same as Design II, the curves are very similar, in spite of the minor variations in the overall beam thickness and beam angle as given in Table 5.1. These results lead to the following design rule: "For chevron-shaped thermal actuators, maintain a slenderness ratio, L/w, less than 50, or assume the worst-case force curve associated with non-ideal buckling."

5.4 Backforce

As discussed in Cragun and Howell (1999), a substantially larger force can be achieved at large deflections by removing the current and using the force available from the thermal strain energy. Figure 5.14 shows a comparison of the powered (heated) force and the backforce or unpowered (cooled) force for Design I. Both simulations use an offset load of 10 μm. This analysis is particularly useful for stepper or ratcheting motors, in which both the powered force and backforce are used.

Simulating the steady-state backforce is simply a matter of applying a displacement to the nonlinear model of an unpowered thermal actuator to determine the reaction

force. Although the backforce is much higher at the maximum deflection, the force drops off to zero as the actuator contracts back to its initial position. The backforce is not susceptible to the buckling instabilities of the pushing force discussed above because it is a result of tension in the beams rather than compression. Consequently, there is practically no difference in the backforce when an offset load of 10 μm is applied vs. the ideal zero offset case.

5.5 Conclusions

This chapter provides experimental force measurements for two different thermal in-plane microactuators, using a combination of both anchored spring or load-line tests and *in-situ* force gauge measurements. This novel test setup allows more data to be gathered on a single mechanism, thus eliminating device-to-device uncertainty in the measurements.

The experimental results for one of the designs showed a significant decrease in the expected performance as compared to the ideal half model. Simulation showed that the phenomenon could be a result of non-ideal loading or small variations in geometry leading to asymmetry. The data matched the simulated worst-case force curve predicted using the full model.

Both the experimental results and simulation showed that an actuator can be designed to reduce the effects of non-ideal buckling by decreasing the beam slenderness ratio, L/w. A general design rule is to use a slenderness ratio L/w less than 50 or assume the worst-case force curve associated with non-ideal buckling.

CHAPTER 6 SURROGATE-BASED UNCERTAINTY ANALYSIS FOR COMPUTER MODELS

This chapter describes approaches for uncertainty analysis that can be applied to nonlinear[1] finite element models for compliant MEMS. The first stage of the simulation process involves building and verifying a parametric model to ensure that uncertainty is propagated correctly. The second stage involves the creation of a first or second-order surrogate[2] model, or *metamodel* ("model of a model"), that can be used in place of the more computationally expensive model. The surrogate model can then be used for sensitivity analysis and uncertainty analysis through a direct use of the attributes (coefficients) of the model (Doebling *et al*., 2002). Finally, the metamodel can be used in a Monte Carlo simulation in order to account for non-Normal distributions and relatively large uncertainties (Iman and Helton, 1984). This approach is demonstrated using the thermal microactuator described in Chapter 5 as an example.

1. The term *nonlinear* can apply to many different aspects of modeling and analysis. *Nonlinear* finite element analysis for compliant mechanisms usually refers to the fact that the small-angle assumption does not apply for large displacements, and therefore the stiffness matrix must be updated at incremental displacements. Also, *nonlinear* can refer to the fact that the force vs. displacement relationship is not a straight line. In statistics, *nonlinear* often refers to a function that does not consist of the addition of terms with constant coefficients. All of these definitions apply to the methods described in this chapter, but only *linear* polynomial regression models are considered (according to the statistical definition). One of the other common uses of the term *nonlinear* in FEA is to describe material properties, but this aspect is not covered in this dissertation.
2. *Surrogate model* and *metamodel* are used interchangeably and both are used to refer to a "model of a model".

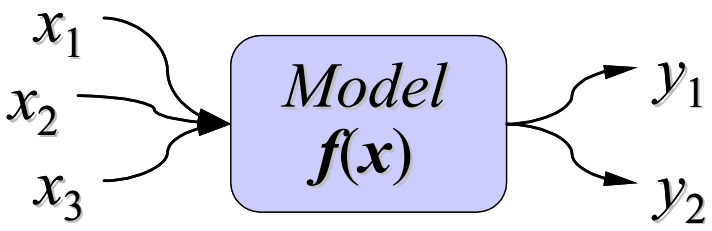

Figure 6.1 A deterministic model treated as a "black box" in which a given set of inputs yield a set of outputs.

6.1 Model Parameterization

Parametric uncertainty analysis treats a model as a "black box", as shown in Figure 6.1. The key to implementing uncertainty algorithms is therefore to be able to first create a parametric model and then be able to interface with the model in a way that permits automated iteration using different inputs.

It is convenient to use a coding scheme that takes a vector of input variables $\mathbf{x} = [x_1, x_2, \ldots, x_n]^T$ and returns a vector of output (response) variables $\mathbf{y} = [y_1, y_2, \ldots, y_p]^T$. The computer model or response surface is then represented by the vector function $\mathbf{f}(\mathbf{x}) = [y_1(\mathbf{x}), y_2(\mathbf{x}), \ldots, y_p(\mathbf{x})]^T$.

When performing uncertainty analysis, we attempt to model the actual behavior of the true system by making **x** a set of variables that can be used to simulate the propagation of error and uncertainty. These variables may or may not correspond to design parameters. For example, there may be uncertainty associated with the stiffness of a material, but for a given material we may not have direct control over the stiffness.

Correct parameterization is important particularly when we need to consider correlation. For example, in surface micromachining, the uncertainty associated with different flexible beams of width w_1 and w_2 may be affected by both independent and correlated sources of variation. It is reasonable to assume that width bias affects both beams equally, but there may also be variation that affects the beams independently, such as surface roughness (usually negligible in MEMS compared to uncertainty in width bias) or spacing (known to affect the side wall angle and the width bias).

There are two main ways of parameterizing the model to account for variation in the beam widths (assuming a constant cross-section along the length of the beam). The first parameterization, and probably the most straight forward, is to treat the width bias, Δw, as a separate design parameter. The input vector would be

$$\mathbf{x} = [x_1, x_2, x_3]^{\mathrm{T}} = [w_1, w_2, \Delta w]^{\mathrm{T}} \tag{6.1}$$

In this case, the model would need to include the reassignments $w_1 = x_1 + x_3$ and $w_2 = x_2 + x_3$ in order to propagate variation in the inputs.

The alternative parameterization eliminates the width bias as one of the inputs by correlating the uncertainty in Δw with the uncertainty in the beam widths, or

$$\mathbf{x} = [x_1, x_2]^{\mathrm{T}} = [w_1, w_2]^{\mathrm{T}} \tag{6.2}$$

The second approach requires the use of more advanced statistical analysis techniques by considering the uncertainty to be correlated rather than handling the correlation within the model itself (see Section 6.5.1). It also has the advantage of reducing the number of inputs, resulting in fewer function evaluations. The benefit of the first approach is

that it is easier to discern from the results whether variations in width bias or the independent variations in the individual beams are more significant (through sensitivity analysis). If the independent random effects are not significant, then you might use $\mathbf{x} = [\Delta w]$ to further reduce the number of variables.

Choosing a parameterization scheme may be the most important part of setting up a problem for uncertainty analysis. In many (if not most) cases, an existing model must be modified or completely re-created in order to properly handle parametric variation. Taking the time to carefully plan the parameterization scheme early in the design process can not only help save time, but can also lead to the creation of a more re-usable model.

6.2 Metamodeling

The goal in metamodeling is to develop an approximate model that is computationally inexpensive to evaluate and provides a better understanding of the functional relationship between $\mathbf{x}$ and $\mathbf{y}$. One of the most well-established and simple methods for developing the surrogate model is to create a first-order or second-order polynomial approximation via regression. This approach is straight forward and the results provide a great deal of information about the behavior of the system that can be used in design.

When the true response surface $\mathbf{y}(\mathbf{x})$ of a computer model is not known or is computationally expensive to evaluate, a metamodel can be constructed as an approximation or surrogate model. The true response surface is then:

$$\mathbf{y} = \mathbf{g}(\mathbf{x}) + \mathbf{e} \tag{6.3}$$

where $\mathbf{g}(\mathbf{x})$ is the surrogate response surface and $\mathbf{e}$ is the error. If the true response surface is a deterministic computer model, then the error is just the error of approximation, as discussed in Simpson *et al*. (1997).

6.2.1 First-Order Polynomials

For uncertainty analysis, where we are evaluating the response surface over only a small portion of the design space, polynomials can often provide a good approximation. Fitting a linear model is usually sufficient for small variations, and it is also the most computationally efficient approach. The first-order response surface can be described as

$$g_i(\mathbf{x}) = b_{io} + \sum_{j=1}^{n} b_{ij} x_j \tag{6.4}$$

where the coefficients b_{ij} are estimates of the partial derivatives of g_i with respect to x_j. If it is desirable to have zero error at the nominal design point, then we can model the first-order *error* surface using:

$$\Delta g_i(\mathbf{x}) = \sum_{j=1}^{n} b_{ij} x_j \tag{6.5}$$

If we substitute Δx_j for x_j in Equation (6.5), then we obtain the first-order Taylor series polynomial

$$\Delta g_i(\Delta\mathbf{x}) = \sum_{j=1}^{n} b_{ij} \Delta x_j \tag{6.6}$$

Compliant mechanisms are typically nonlinear with respect to design parameters. For example, the spring constant for a vertically end-loaded rectangular cantilever beam

involves a multiplicative relationship, $k = Etw^3/(4L^3)$. In this case, interactions between the random variables w, L, t, and E may require the use of a second-order response surface to obtain an accurate estimate of the uncertainty in k, particularly when the uncertainties in the random variables are relatively large.

6.2.2 Second-Order Polynomials

The second-order response surface, as in a second-order Taylor series expansion, involves the use of quadratic and interaction terms. The response surface is

$$g_i(\mathbf{x}) = b_{io} + \sum_{j=1}^{n} (b_{ij}x_j + b_{ijj}x_j^2) + \sum_{j=1}^{n-1} \sum_{k>j}^{n} b_{ijk}x_j x_k \tag{6.7}$$

In Equation (6.7), the coefficients b_{ij} do *not* represent the partial derivatives of g_i with respect to x_j. However, as in Equation (6.6), we can create an error surface that is identical to the second-order Taylor series expansion by substituting Δx for x, or

$$\Delta g_i(\Delta\mathbf{x}) = \sum_{j=1}^{n} (b_{ij}\Delta x_j + b_{ijj}(\Delta x_j)^2) + \sum_{j=1}^{n-1} \sum_{k>j}^{n} b_{ijk}\Delta x_j \Delta x_k \tag{6.8}$$

where $b_{ij} = \partial g_i/\partial x_j$, $b_{ijj} = 0.5(\partial^2 g_i/\partial x_j^2)$, and $b_{ijk} = \partial^2 g_i/(\partial x_j \partial x_k)$.

Second-order polynomials are not always the best choice for forming accurate response surfaces, particularly for models with high-order nonlinearity or discontinuities. Simpson *et al*. (1997) and Jin *et al*. (2001) provide a review and comparison of various metamodeling methods, including polynomial regression, orthogonal arrays, neural networks, inductive learning, kriging, multivariate adaptive regression splines, and radial

basis functions. The trade-offs between these methods have to do with the statistical characteristics of experimental designs (e.g. orthogonality, rotatability, variance, and bias), accuracy, robustness, simplicity, transparency (ease of interpretation), and efficiency. Polynomial regression is one of the most simple approaches and is very accurate for models with low-order nonlinearity (Jin *et al*. 2001).

6.3 The Design Matrix

In order to evaluate sensitivities, perform uncertainty analysis, and create surrogate models, we begin by choosing a design for our computer experiment. The sequence of model evaluations is typically described using a *design matrix*, **D**, such that each row of the matrix represents the levels of the inputs at which to evaluate the computer model (Montgomery and Evans, 1975). For N evaluations of the model,

$$\mathbf{D} = [\mathbf{x}_1, \mathbf{x}_2, \ldots, \mathbf{x}_N]^{\mathrm{T}} \text{ or } \mathbf{D} = \begin{bmatrix} x_{11} & x_{21} & \cdots & x_{n1} \\ x_{12} & x_{22} & \cdots & x_{n2} \\ \cdots & \cdots & \cdots & \cdots \\ x_{1N} & x_{1N} & \cdots & x_{nN} \end{bmatrix} \tag{6.9}$$

In order to compare or describe specific methods for design of experiments, design matrices are usually scaled to $[-1, 1]$. For uncertainty analysis, it is convenient to use the vector $\Delta\mathbf{x} = \mathbf{s}$ to scale the design matrix based upon the standard deviations of the inputs ($\mathbf{s}$). The design matrix can be calculated from the scaled matrix using

$$\mathbf{D} = \mathbf{j}\mathbf{x}^{\mathrm{T}} + \mathbf{D}_s * [\mathbf{j}(\Delta\mathbf{x})^{\mathrm{T}}] \tag{6.10}$$

where $\mathbf{D}_s$ is the scaled design matrix, $\mathbf{j}$ is a vector of 1s of length N, and the operator "*" is used to describe element-wise multiplication, or $\mathbf{A}*\mathbf{B} \equiv a_{ij}b_{ij}$. It is often useful to define an *input perturbation matrix* ($\Delta\mathbf{X}$) as the second term in the right-hand side of Equation (6.10), or

$$\Delta\mathbf{X} = \mathbf{D}_s*[\mathbf{j}(\Delta\mathbf{x})^{\mathrm{T}}] \tag{6.11}$$

There are many possible designs that can be used to create both first-order and second-order response surfaces (Montgomery and Evans, 1975). This section describes a design that corresponds directly to methods used for tolerance analysis where sensitivities are evaluated numerically using finite difference formulae as in Glancy and Chase (1999).

6.3.1 First-Order Designs

There are two main designs for first-order metamodels. The first design corresponds to the model evaluations required to evaluate first-order sensitivities using a forward difference formula. For $n = 3$ variables, the scaled design matrix is

$$\mathbf{D}_{\mathrm{FD}} = \begin{bmatrix} 0 & 0 & 0 \\ 1 & 0 & 0 \\ 0 & 1 & 0 \\ 0 & 0 & 1 \end{bmatrix} \tag{6.12}$$

requiring $N = 1 + n$ function evaluations. The first row of the matrix represents the model evaluated at the nominal inputs. Each variable is then subsequently varied one at a time. Although this design is not accurate over a very large range for nonlinear models, it can be used in optimization routines and for screening variables that may not have a significant impact on the response or the overall uncertainty.

The second design corresponds to the function evaluations required to evaluate first-order sensitivities using a central difference formula. For $n = 3$ variables, the scaled design matrix is

$$\mathbf{D}_{\text{CD}} = \begin{bmatrix} 0 & 0 & 0 \\ \pm 1 & 0 & 0 \\ 0 & \pm 1 & 0 \\ 0 & 0 & \pm 1 \end{bmatrix} \tag{6.13}$$

requiring $N = 1 + 2n$ function evaluations. The elements ± 1 are shorthand notation for indicating two function evaluations, one at the $+1$ level, and one at the -1 level. This design can be used to assess the linearity of the main effects and obtain better approximations of first-order sensitivities for nonlinear models. It does not include the interaction effects that are almost always present in compliant mechanisms.

6.3.2 Second-Order Designs

There are many possible designs for second-order metamodels. A design that corresponds to the function evaluations used to evaluate second-order sensitivities using central difference formulae is

$$\mathbf{D}_{\text{BBD}} = \begin{bmatrix} 0 & 0 & 0 \\ \pm 1 & 0 & 0 \\ 0 & \pm 1 & 0 \\ 0 & 0 & \pm 1 \\ \pm 1 & \pm 1 & 0 \\ \pm 1 & 0 & \pm 1 \\ 0 & \pm 1 & \pm 1 \end{bmatrix} \tag{6.14}$$

This design is formed by augmenting Equation (6.13) with a Box-Behnken design (BBD), where each row containing $(\pm 1, \pm 1)$ represents four function evaluations corresponding to a 2^2 factorial design for each pair of parameters. The full design requires $N = 1 + 2n^2$ function evaluations.

One of the benefits of this design is that the simulation can be performed in stages as the need for greater accuracy arises. Another design that has this same benefit is the central composite design (CCD), which is formed by augmenting Equation (6.13) with a 2^n full factorial design. Both the BBD and CCD families of designs are commonly used for fitting second-order response surfaces.

The disadvantage of second-order metamodels is that they are only practical for problems involving a small number of variables (less than 10). However, for compliant MEMS, the uncertainty is usually dominated by only a few significant variables, and these variables can usually be identified and screened via sensitivity analysis.

It is not always necessary to use integer values of ± 1 in the scaled design matrices. For convenience, it is often useful to evaluate the axial points or main effects at ± 1 and the interactions at ± 2 or vice versa. Although not necessarily optimal designs[3], the results of the computer experiment can help provide intuition about how the model is behaving at the extreme levels and to help determine whether there are discontinuities in the model. As an example, Figure 6.2 shows a plot of the simulated force vs. displacement curves for a

3. It is not within the scope of this dissertation to discuss the details of choosing optimal design matrices. However, it is important to realize that using different design matrices and even different factor levels can lead to differences in the accuracy of a surrogate model.

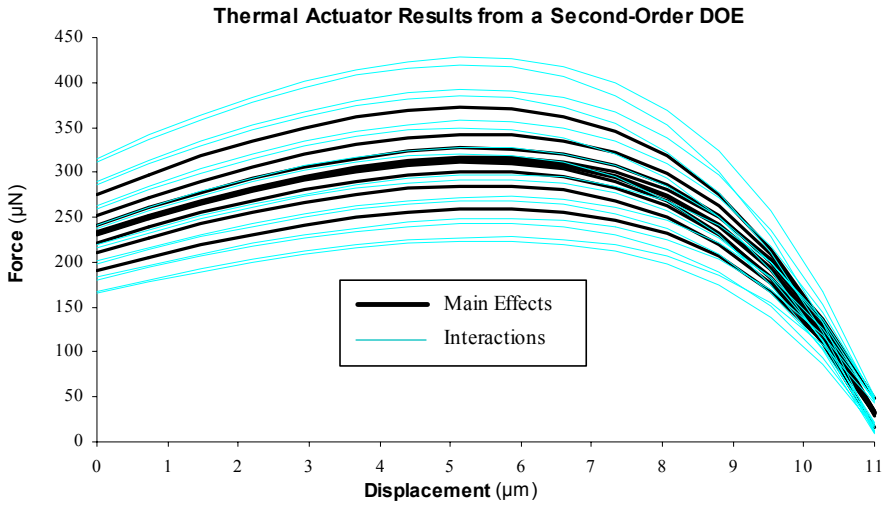

Figure 6.2 Plot of the simulated force vs. displacement curves for a thermal microactuator using a second-order design of experiments.

thermal microactuator using a second-order design of experiments (varying stiffness, beam width, beam thickness, and residual stress). Graphing the results is an extremely important step in analyzing the results of a computer experiment.

6.3.3 Sampling-Based Designs

Sampling-based simulation methods like pseudo-Monte Carlo (MC) sampling, Latin hypercube sampling (LHS), and orthogonal array (OA) sampling, also make use of a design matrix. In Monte Carlo sampling, each row of the matrix represents a "draw" from the individual marginal distributions of the inputs. MC simulations often involve more than 10,000 function evaluations in order to obtain accurate results.

Latin hypercube sampling provides a more efficient sample of the design space while preserving the probabilistic characteristics of the inputs. OA is similar to LHS and can be used to generate Latin hypercube samples (LHS can be considered a special case of OA). LHS and OA are both more complex than Monte Carlo simulation and will not be

discussed in this dissertation. However, these methods warrant further investigation for use in MEMS and compliant mechanisms due to their superior accuracy and computational efficiency (Guinta *et al*., 2003).

6.4 Multivariate Polynomial Regression

Multivariate polynomial regression can be used to estimate the coefficients of polynomial metamodels for multiple response variables, thereby determining the sensitivities with respect to individual input parameters (Jin *et al*., 2003; Simpson *et al*., 1997; Myers and Montgomery, 1995). Polynomial regression is particularly convenient for analysis of nonlinear finite element models, where we may want to estimate error bands for force-displacement curves.

If we have stored the results of the computer experiment in a matrix $\mathbf{Y}$ of size N x p, we can use multivariate multiple linear regression (Rencher, 1995) to evaluate the coefficients in Equations (6.4) and (6.7), because the polynomial response surface is of the form $\mathbf{Y} = \mathbf{XB}$. The estimates of the coefficients are found using a least-squares fit, or

$$\mathbf{B} = (\mathbf{X}^{\mathrm{T}}\mathbf{X})^{-1}\mathbf{X}^{\mathrm{T}}\mathbf{Y} \tag{6.15}$$

6.4.1 Example: Area Properties of a Rectangle

To demonstrate how this approach is applied, assume we want to determine the uncertainties in the area properties of a rectangle due to variations in the width and height. We start with the parameterization, $\mathbf{x} = [w, t]^{\mathrm{T}}$, where $w = 2$ is the width in the y-direction and $t = 5$ is the thickness in the z-direction. The standard deviations for w and t are

specified as $\mathbf{s} = [0.08, 0.02]^{\mathrm{T}}$. The model calculates the outputs, $\mathbf{y} = [A, I_y, I_z]$, where $A = wt$ is the area, and $I_y = wt^3/12$ and $I_z = tw^3/12$ are the centroidal moments of inertia about the y and z axes, respectively.

The next step is to decide on a design matrix. For this example, we use the BBD design, which for 2 variables is identical to a central composite design. The scaled design matrix is

$$\mathbf{D}_s = \begin{bmatrix} 0 & 0 \\ \pm 1 & 0 \\ 0 & \pm 1 \\ 1 & 1 \\ 1 & -1 \\ -1 & 1 \\ -1 & -1 \end{bmatrix} \tag{6.16}$$

resulting in $N = 9$ function evaluations. We then use Equation (6.10) to define the design matrix, **D**, and Equation (6.10) to define the input perturbation matrix, $\Delta\mathbf{X}$.

At this point, the model is run by looping through the design matrix **D** and evaluating **y** for each set of inputs. The result is an N x 3 matrix **Y**. Subtracting the nominal value for the response **y** from each row of **Y** results in the error response, $\Delta\mathbf{Y}$.

The next step is to create the matrix **X** based upon the type of model that we want to fit. In this case, we use a second-order error surface using the model given in Equation (6.8). For this model, the **X** matrix, or matrix of regressors, is

$$\mathbf{X} = [\Delta\mathbf{w}, \Delta\mathbf{t}, (\Delta\mathbf{w})^2, (\Delta\mathbf{t})^2, \Delta\mathbf{w}*\Delta\mathbf{t}] \tag{6.17}$$

where $\mathbf{w}$ and $\mathbf{t}$ are the first and second columns of $\mathbf{D}$, respectively, and element-wise multiplication is used for $(\Delta\mathbf{w})^2$ and $\Delta\mathbf{w}*\Delta\mathbf{t}$.

Solving for the regression coefficients using Equation (6.15) results in

$$\mathbf{B} = \begin{bmatrix} 5 & 10.417 & 5.003 \\ 2 & 12.5 & 0.669 \\ 0 & 0 & 2.5 \\ 0 & 2.5 & 0 \\ 1 & 6.25 & 1.001 \end{bmatrix} \tag{6.18}$$

The first two rows of $\mathbf{B}$ are the transpose of the sensitivity matrix, θ, where the elements θ_{ij} are estimates of $\partial y_i / \partial x_j$. The remaining rows can be parsed to form the Hessian matrix for each individual response variable y_i. The MATLAB code for this example problem can be found in Appendix A.5.

6.4.2 Application to Nonlinear Finite Element Analysis

This approach can be extended to nonlinear finite element analysis of compliant mechanisms to obtain a metamodel for force vs. displacement. For this type of problem, the "black box" becomes the finite element code that accepts $\mathbf{x}$ as input and returns as output the force evaluated at discrete displacements. The displacements, defined as the vector $\mathbf{d} = [d_1, d_2, \ldots, d_p]^T$, correspond to the output $\mathbf{y} = [y_1, y_2, \ldots, y_p]^T$. Each model evaluation results in a single force-displacement curve, plotted as $\mathbf{y}$ vs. $\mathbf{d}$.

6.4.3 Application to Kinematics

In kinematics, it is common to evaluate the coordinates of a coupler point along the path of the mechanism, given the angular displacement of one of the links as the input. In this case, we could define $\mathbf{d} = [\theta_1, \theta_2, \ldots, \theta_{10}]^T$ to be the angular displacements at 10 discrete points, $[y_1, y_2, \ldots, y_{10}]^T$ to be the *x*-position of the coupler point, and $[y_{11}, y_{12}, \ldots, y_{20}]^T$ to be the *y*-position of the coupler point. Formulating the problem in this manner and using first-order variance propagation described below (Section 6.5.2), one could evaluate the covariance between the *x*-position and *y*-position as described in Wittwer *et al*. (2004).

6.4.4 Metamodel Accuracy

It is important to point out that test statistics used in regression for evaluating goodness of fit and other parameters usually do not apply to deterministic computer models, because there is no random component (see Simpson *et al*., 1997). The BBD and CCD designs described above usually provide "just enough" function evaluations to create second-order response surfaces. Therefore, the R-Squared metric for regression (model sum of squares divided by the total sum of squares) is often insufficient. Creating residual plots after testing the metamodel at different data points is important for verifying the accuracy of the metamodel.

6.5 Uncertainty and Sensitivity Analysis

This section describes analysis procedures that make use of the first-order uncertainty and sensitivity analysis, including correlation in **x**. This approach is often sufficient

for most small-scale problems (less than 30 variables), but the example in Section 6.8 demonstrates a case in which second-order methods are required.

6.5.1 The Covariance Matrix, $\mathbf{S}_x$

For first-order parametric uncertainty analysis, the uncertainties in the inputs are described using a covariance matrix $\mathbf{S}_x$. In general uncertainty analysis, random and systematic uncertainties are grouped together and treated as random (Coleman and Steele, 1999, pg. 48), although we can define a separate covariance matrix for random and systematic uncertainties in order to perform detailed uncertainty analysis (this does not affect the number of function evaluations).

If the uncertainties associated with each of the inputs in $\mathbf{x}$ is independent, then we can define a vector $\mathbf{s} = [s_1, s_2, \ldots, s_n]^T$ where s_i is the standard deviation of x_i. If the inputs are correlated, then we can define a covariance matrix $\mathbf{S}_x$ that can be used to take into account linear correlation. If all x's are independent, then $\mathbf{S}_x$ is a diagonal matrix where each element s_{ii} is the variance of x_i, or $s_{ii} = s_i^2$.

Feature geometries in MEMS are usually correlated due to the effects of edge bias and layer deposition and conformity (see Chapter 7). When inputs are correlated, it is often convenient to work with the correlation matrix, $\mathbf{R}_x$, which is analogous to $\mathbf{S}_x$ through the relationships

$$\mathbf{S}_x = \mathbf{D}_s \mathbf{R}_x \mathbf{D}_s \tag{6.19}$$

and

$$\mathbf{R}_x = \mathbf{D}_s^{-1}\mathbf{S}_x\mathbf{D}_s^{-1} \tag{6.20}$$

where $\mathbf{D}_s$ is a diagonal matrix with elements $d_{ii} = \sqrt{s_{ii}} = s_i$ (see Rencher, 1995, pg. 69).

The elements of $\mathbf{R}_x$ are known as correlation coefficients, defined as

$$r_{ij} = r_{ji} = \frac{s_{ij}}{\sqrt{s_{ii}s_{jj}}} \tag{6.21}$$

The diagonal elements of $\mathbf{R}_x$ are all equal to 1, and if all x's are independent, the off-diagonal elements are zero. An exact linear relationship between two inputs results in r_{ij} equal to either 1 or -1, depending on the slope of the line. If the exact linear relationship is known, then including the functional relationship in the model can reduce the number of inputs and the complexity of the analysis (see Chapter 7).

6.5.2 First-Order Variance Propagation

First-order approximations of the uncertainty in **y** are almost always useful. It is not unreasonable to say that the majority of design problems can be greatly enhanced through first-order sensitivity and uncertainty analysis techniques (also known as first-order second-moment, FOSM, methods). More advanced methods may be applied to a particular problem when greater accuracy is needed, or when the problem involves discontinuities or an extremely large number of variables. In practice, the designer must consider the issue of diminishing return on investments made to implement more advance methods in design.

The estimate of the covariance of **y** can be found using

$$\mathbf{S}_y = \theta \mathbf{S}_x \theta^{\mathrm{T}} \tag{6.22}$$

which is derived from a first-order multivariate Taylor series expansion about the nominal values of **x** and **y**. θ is the sensitivity matrix of size p x n where the elements θ_{ij} represent $\partial y_i / \partial x_j$. In order to see how this equation relates to univariate notation, note that the variance of y_i is calculated as

$$\mathrm{var}(y_i) = \sum_{j=1}^{n} \left(\frac{\partial y_i}{\partial x_j}\right)^2 s_{jj} + 2 \sum_{j=1}^{n-1} \sum_{k=j+1}^{n} \left(\frac{\partial y_i}{\partial x_j}\right)\left(\frac{\partial y_i}{\partial x_k}\right) s_{jk} \tag{6.23}$$

It is usually advisable to develop a model such that the inputs are uncorrelated (see Saltelli *et al*., 2000, pg. 134). When the inputs are independent, then $s_{jk} = 0$ and all the covariance terms involving s_{jk} are zero. It is then straightforward to determine the relative effects of the individual parameter uncertainties s_j on the total variance of y_i. When uncertainties are not independent, it is not as straightforward to determine the effects of individual variables on the overall variance because correlation could have either the effect of increasing or decreasing the total variance.

For systems of implicit equations, the sensitivity matrix can be found as described in Chapter 3 (also Wittwer *et al*. 2002b), but an approach more amenable to automation is to estimate the sensitivities using finite-difference techniques or regression as described in Section 6.4. In other words, the sensitivities are obtained directly from the metamodel.

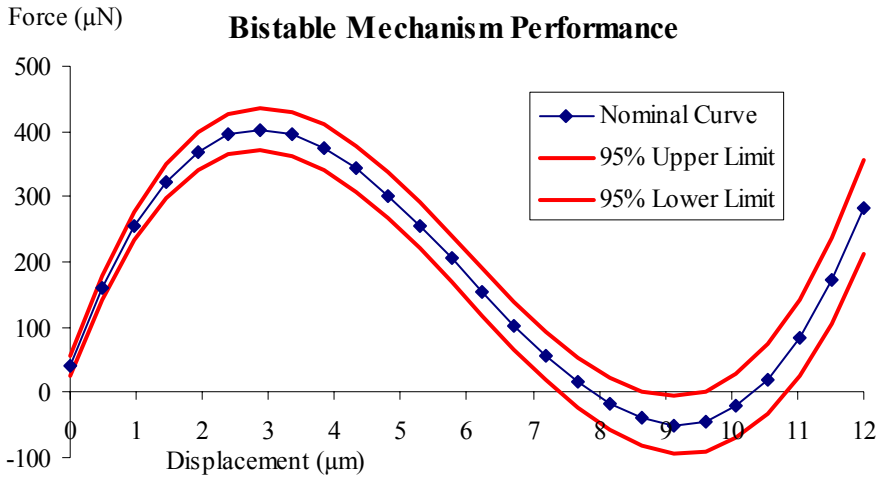

Figure 6.3 Force vs. displacement relationship for a bistable mechanism, including estimates of the 95% confidence limits.

Figure 6.3 shows the uncertainty in the force of a bistable micromechanism evaluated at discrete displacements. The 95% confidence level is estimated by multiplying the standard deviation by a factor of ±2. This assumes the distribution is Normal, but even as an approximation, visualization of the uncertainty in this manner can be useful. Note that in this example, the response variable $\mathbf{y} = [y_1, y_2, \ldots, y_{26}]^T$ consisted of $p = 26$ points, corresponding to the discrete displacements $\mathbf{d} = [d_1, d_2, \ldots, d_{26}]^T$ where $d_1 = 0$ and $d_{26} = 12$.

6.5.3 Sensitivity Analysis

It is often helpful to evaluate a design based upon the sensitivity of performance with respect to variations. There are many methods for sensitivity analysis, with a good overview provided by Saltelli *et al.* (2000)[4].

In order to judge which parameters contribute the most to the uncertainty, the sensitivities must first be scaled or normalized appropriately. This can be accomplished using uncertainty percentage contributions (UPCs) and uncertainty magnification factors (UMFs) as described by Coleman and Steele (1999). Neglecting correlation (an important assumption), the UPCs can be found using

$$[\text{UPC}] = \mathbf{D}_{S_y}^{-1} \theta \mathbf{D}_{S_x} \tag{6.24}$$

where the diagonals of $\mathbf{D}_{S_x}$ and $\mathbf{D}_{S_y}$ are the diagonals of the $\mathbf{S}_x$ and $\mathbf{S}_y$ matrices, respectively. The [UPC] matrix is a p x n matrix where each element represents $\partial y_i / \partial x_j$ normalized by multiplying by s_{xj} / s_{yi} or

$$[\text{UPC}]_{ij} = \left(\frac{\partial y_i}{\partial x_j}\right)\left(\frac{s_{xj}}{s_{yi}}\right) \tag{6.25}$$

If the uncertainties of **x** are not known, the sensitivities can be compared using UMFs (see also Saltelli *et al*., 2000, pg. 87) which are found by

$$[\text{UMF}] = \mathbf{D}_y^{-1} \theta \mathbf{D}_x \tag{6.26}$$

where $\mathbf{D}_y$ is the diagonal matrix of **y** and $\mathbf{D}_x$ is the diagonal matrix of **x**. The [UMF] matrix is a p x n matrix where each element represents $\partial y_i / \partial x_j$ normalized by multiplying by x_j / y_i or

$$[\text{UMF}]_{ij} = \left(\frac{\partial y_i}{\partial x_j}\right)\left(\frac{x_j}{y_i}\right) \tag{6.27}$$

4. The approach in this section would be described as a first-order *local* sensitivity analysis method because it is based upon an expansion at a specific design point. Although the analysis can be applied to a vector **y** and not just a single response variable, global sensitivity analysis is used to describe a method that investigates the effects of the uncertainty over the full range of the design parameters.

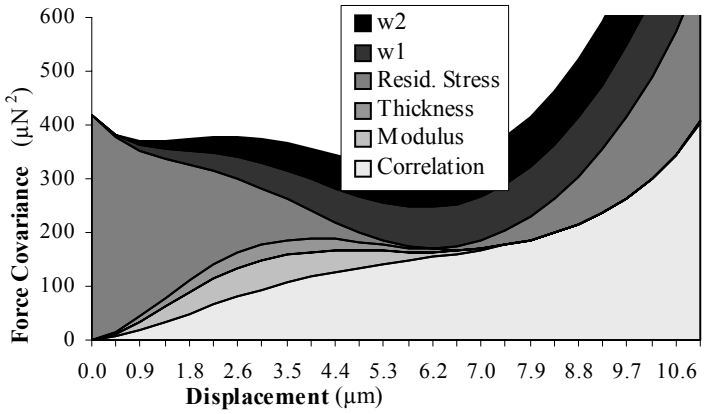

Figure 6.4 Uncertainty contributions visualized using an area chart (including correlation).

A problem with using UMFs for normalizing sensitivities is that for when y_i is equal to zero, the UMF is undefined.

Sensitivity analysis often involves the creation of bar charts to visualize and rank the effects of individual uncertainties on the total variance. For nonlinear finite element models, sensitivities may change with time or displacement. In these cases, area charts are useful for graphing the uncertainty contributions (Wittwer *et al*., 2002a). An area chart provides a visual representation of Equation (6.23), where the magnitude of each individual term is represented by the thickness of the shaded area in the chart (see Figure 6.4). The total variance is represented as the sum of the stacked areas. Effects of individual input correlations cannot be visualized with these types of area charts, because the areas overlap if the covariance is negative. Therefore, a single area, included as the lower area in the chart, is used to represent the sum of the terms in which the covariance is non-zero ($s_{jk} = 0$). Figure 6.4 shows an example area chart for a bistable mechanism that is used as a case study in Chapter 7.

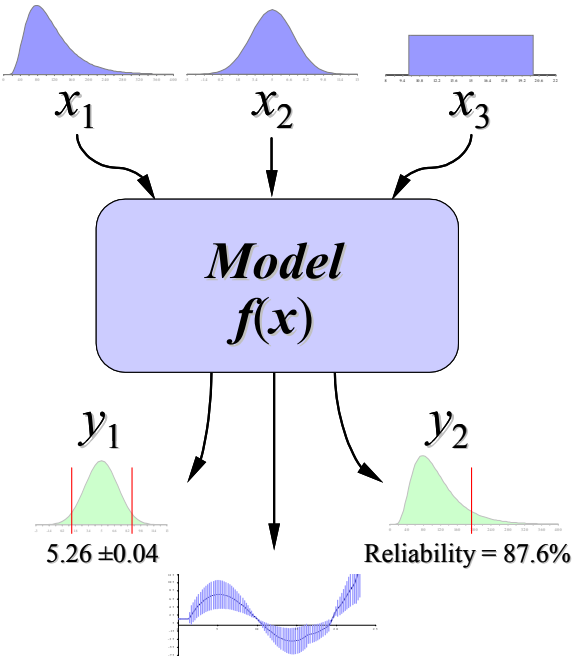

Figure 6.5 Schematic showing stochastic uncertainty propagation (the basic principle behind Monte Carlo simulation).

6.6 Monte Carlo Simulation

One of the main benefits of metamodeling is that Monte Carlo (MC) simulation can be run using the surrogate model to benefit from the dramatic increase in computational efficiency. Inclusion of non-normal distributions and the analysis of the results is straight forward and intuitive. In practice, the principles behind MC simulation are easily explained and understood by even those without an extensive background in statistics. Figure 6.5 shows a schematic of how stochastic simulation and uncertainty propagation work.

The Monte Carlo method is just one of many sampling-based methods for analyzing uncertainty propagation, where the goal is to determine how random variation, lack of knowledge, or error affects the sensitivity, performance, or reliability of the system that is

being modeled. Monte Carlo simulation is categorized as a sampling method because the inputs are randomly generated from probability distributions to simulate the process of sampling from an actual population. It is important to choose a distribution for the inputs that most closely matches existing data, or best represents the current state of knowledge.

The only additional error associated with a surrogate-based MC simulation as opposed to a simulation using the original computer model, is the error of approximation in the metamodel. Many error metrics exist to help estimate this error, and this is an active area of research (Doebling *et al*., 2002; Jin *et al*., 2001; Simpson *et al*., 1997). It could be argued that the validity of using surrogate-based approaches requires the determination of the error in the metamodel, making these techniques not necessarily more efficient for design. However, just as with most design, modeling, and simulation tasks, the experience and understanding contributed by the designer is essential for determining the validity and value of the approach and for determining what level of experimental validation may be required.

A full second-order metamodel is not required to perform surrogate-based Monte Carlo simulation. Any computationally efficient metamodel should work, provided the model parameterization correctly propagates sources of uncertainty and variation. If a first-order model is sufficiently accurate, then MC can be performed to take into account non-Normal distribution information.

The data generated from the simulation can be represented as probability distributions (or histograms) or converted to error bars, reliability predictions, tolerance zones, and confidence intervals. Methods for analyzing the data can be found in most basic statis-

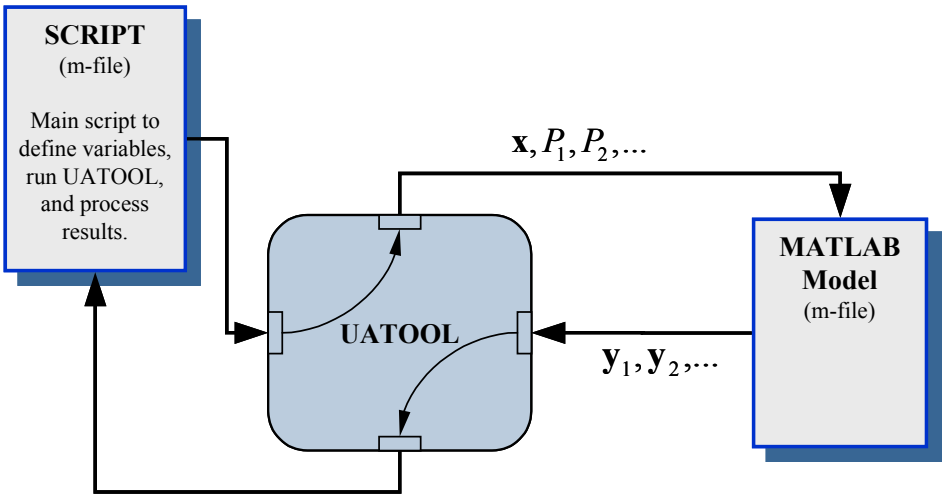

Figure 6.6 Schematic showing how the uncertainty analysis toolkit function (UATOOL) interfaces with a parametric MATLAB model.

tics textbooks (see Vardeman, 1994). A good overview of Monte Carlo simulation is provided in the thesis by David Larsen (1989).

6.7 Implementation

In order to facilitate methods for uncertainty analysis, optimization, and design and analysis of computer experiments, a quasi-object-oriented toolkit has been developed in MATLAB based upon the interface used by the existing optimization toolkit. Although other software exists, the motivation for developing this tool was the fact that many of the MEMS models used as case studies for this research were developed using MATLAB. In addition, MATLAB provides a powerful base of mathematical and graphing functions that make implementing various computer experiments straightforward.

Figure 6.6 shows a schematic of how the toolkit interfaces with an existing parametric model in MATLAB. The model is simply a function that accepts a vector **x** as input and returns any number of output vectors. After the parametric model is created, a sepa-

rate script file is created to define the input parameters and uncertainties, set parameters for telling the UATOOL function what type of analysis to perform, and processing the results (creating graphs and reports). Any number of design parameters P_1, P_2, … can be passed from the script to the model. Only the values in **x** are modified by UATOOL.

The model can be defined entirely within MATLAB, or the function can act as an interface between MATLAB and some other commercial or custom simulation software. Many analysis packages provide the ability to run an analysis in "batch" mode using command line input and text files. For this research, the ANSYS Parametric Design Language (APDL) is used to create a parametric finite element models that can be run in batch mode from MATLAB.

To take the analysis a step further, the entire uncertainty model can be nested inside of a separate function that is called by an optimization routine in order to perform robust design under uncertainty. This procedure has been applied to the design of a fully compliant bistable mechanism, described in the next chapter.

6.8 Example: Thermal Actuator Uncertainty

To demonstrate how the procedures discussed in this chapter can be used in compliant MEMS, the thermal microactuator model described in the previous chapter will be used. This example demonstrates a two-stage procedure involving both an analytical model to calculate the area and moment of inertia of the beams (Stage 1) and a finite ele-

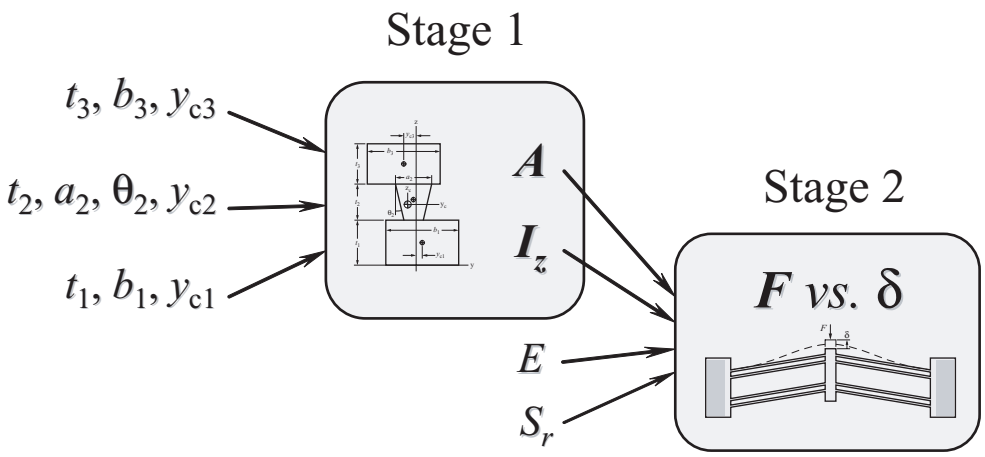

Figure 6.7 Diagram of the thermal actuator uncertainty model. Stage 1 evaluates cross-section properties and Stage 2 evaluates the force vs. displacement curve using FEA.

ment model to determine the force vs. displacement relationship (Stage 2). Figure 6.8 shows a diagram depicting these two stages and the variables that are used as inputs.

One of the reasons for performing the analysis in two stages has to do with the number of uncertain parameters. In Stage 1, there are 10 variable parameters and in stage 2, there are 2 more (E and S_r). With 12 variables, a second-order method would result in $1 + 2k^2 = 289$ function evaluations (using the $\mathbf{D}_{\text{BBD}}$ design matrix). The TIM model takes about 25 seconds to run, so the experiment would take about 1.6 hours to complete. With the staged analysis, the TIM model has only 4 uncertain variables, and the time can be cut to 11 minutes (33 function evaluations).

Another reason for performing the analysis in stages is that it can help determine how errors or variations are propagating through the different models. Other MEMS devices may use similar beam cross-section models, so the first stage of the analysis can provide information useful to many other design problems.

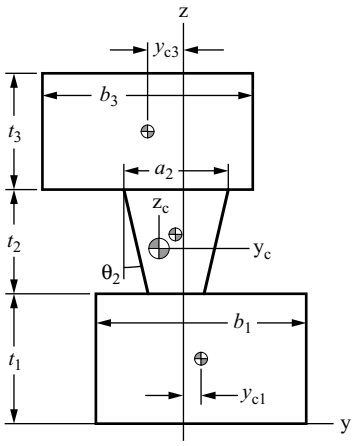

Figure 6.8 Cross-section of a thermal actuator beam.

6.8.1 Stage 1: Uncertainty Analysis for Cross-Section Area Properties

The first stage of the analysis involves determining the area (A) and moment of inertia (I_{z_c}) of the beam based upon the cross-section described in Figure 6.8. The areas in the diagram correspond to the Poly3, Oxide4, and Poly4 layers in the SUMMiT process. (The second area is actually formed by etching Oxide4, and the conformity of the Poly4 deposition fills in the hole, forming a via.)

Some correlation exists between A and I_{z_c} because variations in widths and thicknesses affect both of these area properties. The model calculates the results using equations for a set of stacked rectangles and trapezoids (see Appendix B). These equations can be found in most strength of materials (Gere and Timoshenko, 1997) and machine design textbooks.

The sources of uncertainty affecting the area and moment of inertia are variations in line widths, layer thicknesses, mask alignment, and uncertainty associated with the

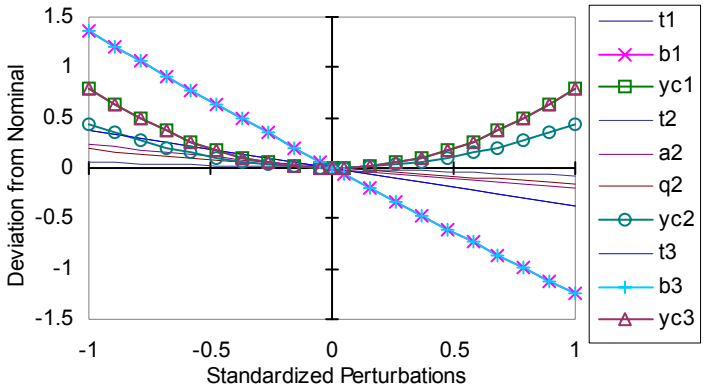

Figure 6.9 A spider graph showing the relationship between input perturbations and deviations in moment of inertia.

slope of the sidewalls for the web. The variables and their associated uncertainties and assumed distributions are summarized in Table 6.1. The thicknesses are assumed to follow a normal (N) distribution because the fabrication process targets specific layer thicknesses. The other variables are assumed to follow a uniform (U) distribution to provide a conservative estimate of variation (due to the lack of data).

6.8.2.1 Investigating Nonlinearity

Figure 6.9, sometimes called a "spider graph", shows the deterministic relationship between the individual sources of uncertainty and the moment of inertia. To create this type of plot, the model is run by changing a single variable at a time, but at multiple incre-

Table 6.1 Cross-section parameter values.

Variable	Units	Nominal	St.Dev.	Dist.
t_1	µm	2.25	0.041	N
t_2	µm	2	0.181	N
t_3	µm	2.25	0.042	N
y_{ci}	µm	0	0.2	U
b_1	µm	3.8	0.08	U
b_3	µm	3.8	0.08	U
a_2	µm	2	0.08	U
θ_2	degrees.	10	2	U

ments in order to investigate nonlinearity. The equation for the moment of inertia is nonlinear with respect to the input variables, so this type of plot helps to determine whether linear (first-order) uncertainty analysis methods are appropriate. The plot shows that for a small portion of the domain (i.e. the deviation space), I_{z_c} may be linearized[5] with respect to all variables except for y_{c1}, y_{c2}, and y_{c3}. To properly account for uncertainty associated with these variables (which is due to mask misalignment and/or differences in edge bias between the left and right side of the beam), a quadratic or second-order method would have to be used, because the first derivative of I_{z_c} with respect to y_{ci} is zero, or $\partial I_{z_c} / \partial y_{ci} = 0$ for i = 1, 2, and 3.

Another use for the spider graph is to show the relative contributions of the uncertainties on the response (i.e. the sensitivities). To compare the sensitivities, the uncertainties are normalized using the standard deviations (σ) of the inputs such that [-2σ,2σ] scales to [-1,1]. The graph shows that the variation in b_1 and b_3 (the widths of the first and third layer) are affecting I_{z_c} more than the other uncertainties.

The MATLAB code for generating the design matrices and creating the spider graph is listed in Appendix A.4.

6.8.3.2 Uncertainty Analysis

The results of the uncertainty analysis using both the second-order Monte Carlo (SOMC) method and direct Monte Carlo Simulation (MCSIM), using a sample size of

5. This assumes that the interactions between the variables are not significant. The spider graph does not take into account interactions. It is only meant to assess linearity with respect to main effects.

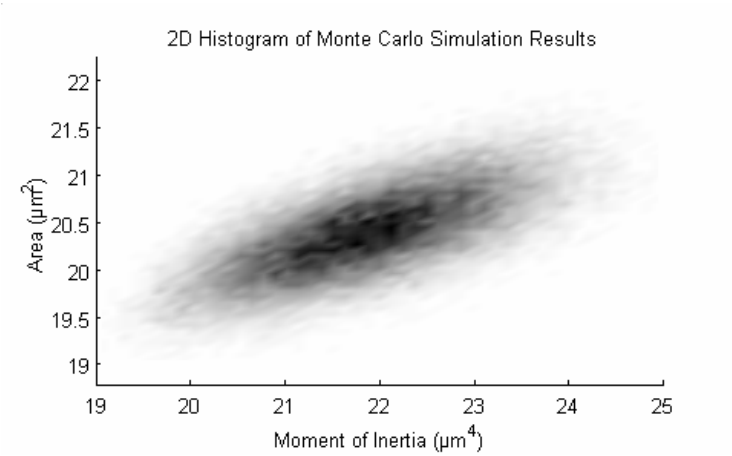

Figure 6.10 2-D histogram showing results of the Monte Carlo simulation for the area and moment of inertia.

50000 function evaluations, are summarized in Table 6.2 for a number of different area properties. The standard deviation estimated with a first-order second-moment method (FOSM) using central difference derivatives is also included, but as mentioned above, this method cannot correctly account for variation in mask alignment when calculating I_{z_c}. One of the interesting results is that variations in y_{ci} can lead to a non-zero product of inertia $I_{y_c z_c}$ which may be undesirable if out-of-plane motion must be avoided.

Figure 6.10 shows the results of the Monte Carlo simulation for A and I_{z_c} as a shaded 2-D histogram. (The MATLAB code for the 2-D histogram can be found in Appen-

Table 6.2 Cross-section uncertainty analysis results.

Property	Nominal	FOSM	SOMC		MCSIM	
		St.Dev.	Mean	St.Dev.	Mean	St.Dev.
A	20.40 μm^2	0.46	20.38	0.47	20.38	0.47
I_{y_c}	85.53 μm^4	7.36	85.67	7.34	85.67	7.35
I_{z_c}	21.36 μm^4	0.97	21.89	1.06	21.89	1.06
$I_{y_c z_c}$	0 μm^4	5.14	0.02	5.15	0.02	5.15
t_{total}	6.5 μm	0.19	6.50	0.19	6.50	0.19

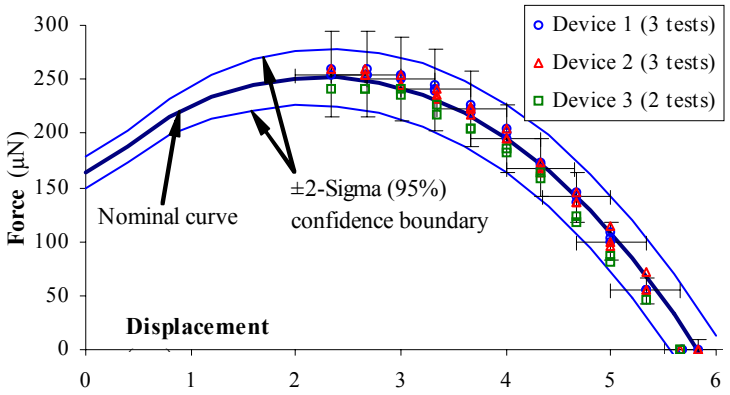

Figure 6.11 Model validation for Design II of the thermal microactuator.

dix A.1.) As expected, these results show that the variation in area and moment of inertia are linearly correlated. The correlation coefficient is 0.68. Because the TIM force model takes as input the area and moment of inertia of the beams, we can use the correlation in the uncertainty analysis rather than assuming that variations in area and moment of inertia are independent.

6.8.4 Stage 2: Force vs. Displacement

To evaluate the force vs. displacement curve for the thermal actuator requires a nonlinear finite element model. The model was discussed in detail in the previous chapter, and the ANSYS batch file can be found in Appendix C.1. The method discussed in Section 6.5.2 is used to estimate the uncertainty due to variations in A, I_{z_c}, E, and S_r.

The results of the first-order uncertainty analysis are shown in Figure 6.11, along with the data obtained from multiple tests of three different devices as described in the previous chapter. The estimated uncertainty from the computer simulation is shown as a 95% confidence boundary. The data is well within the confidence boundary, so we can use this as evidence that our model is valid. For statistical model validation as described in

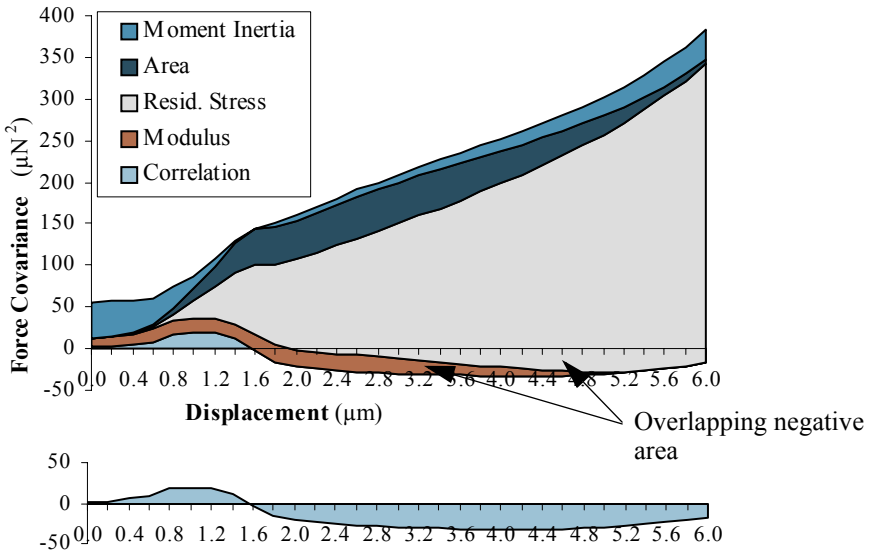

Figure 6.12 Uncertainty contributions for Design II of the thermal microactuator showing the effect of negative covariance.

Baghdasaryan *et al*. (2002), it is important to consider errors that are not included in the simulated uncertainty propagation. This is done by including error bars on the data points. In Figure 6.11 the error bars represent the measurement error associated with the uncertainty in displacement measurements and the force gauge spring constant. Because the confidence regions for both the simulation and the error bars overlap, there is not enough evidence to declare the model invalid.

The sensitivity analysis of the thermal actuator, shown in Figure 6.12, provides more insight into the behavior of the device with respect to the uncertainties. Residual stress is a major contributor to uncertainty in force, with the effect increasing with displacement. It is also interesting that for displacements larger than 1.6 μm, the correlation between the area and moment of inertia (the only inputs with non-zero covariance) results in a negative force covariance term. Because this is a stacked area chart, the positive vari-

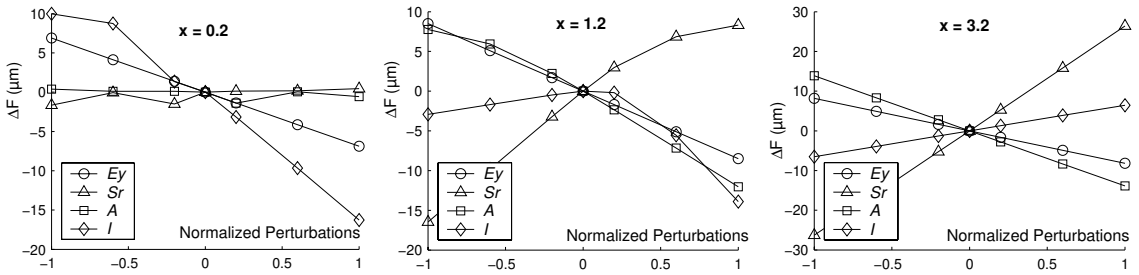

Figure 6.13 Spider graphs at three displacements (x) of the thermal actuator.

ance contributions overlap the negative covariance, so the area corresponding to the correlation is shown separately below the chart.

For the thermal actuator, a negative covariance is beneficial because it means that the effects of the uncertainty are being reduced. To understand what is happening, it is helpful to analyze the covariance term associated with the correlation between A and I_{z_c},

$$2\left(\frac{\partial F}{\partial A}\right)\left(\frac{\partial F}{\partial I_{z_c}}\right)s_{AI} \tag{6.28}$$

The analysis in Stage 1 showed that the correlation is positive, so s_{AI} is positive. The sensitivities, $\partial F/\partial A$ and $\partial F/\partial I_{z_c}$, must have opposite signs in order to result in a negative covariance term. The spider graph in Figure 6.13 verifies that for a displacement of 3.2, where the covariance is negative, $\partial F/\partial A$ is negative and $\partial F/\partial I_{z_c}$ is positive.

The spider graphs also show that the effects of A, I_{z_c}, and S_r are not linear for displacements of 0.2 and 1.2. According to the simulations in the previous chapter, these displacements are in the region of the force-displacement curve where non-ideal buckling occurs. A first-order metamodel may not be sufficient for accurate uncertainty predictions in this region.

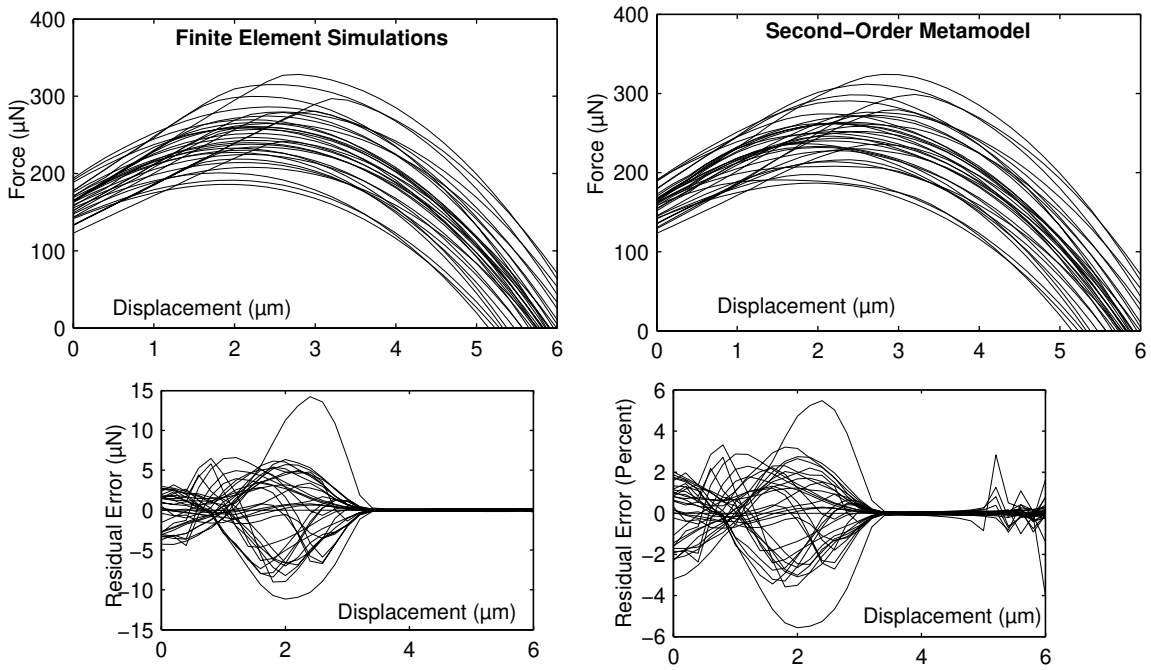

Figure 6.14 Comparison of finite element simulations to the second-order metamodel.

6.8.5 Second-Order Monte Carlo Simulation

To obtain a more accurate estimate of the uncertainty including distribution information, we can try a second-order Monte Carlo simulation. This is done in two steps. The first step is to create a second-order metamodel. The design matrix is created using the vectors **x** and Δ**x** shown in Table 6.3. For this example, a Box Behnken design is used. Figure 6.14 shows a comparison between the finite element simulations and the second-order metamodel. The residual error, or difference between the metamodel and the FEA simulations is less than 15 μN or 6% over the entire range of displacement.

Table 6.3 Stage 2 metamodel parameters.

Variable	Units	**x**	Δ**x**
E	MPa	164000	3200
S_r	MPa	-10	5
A	μm^2	20.40	0.5
I_Z	μm^4	21.36	1.1

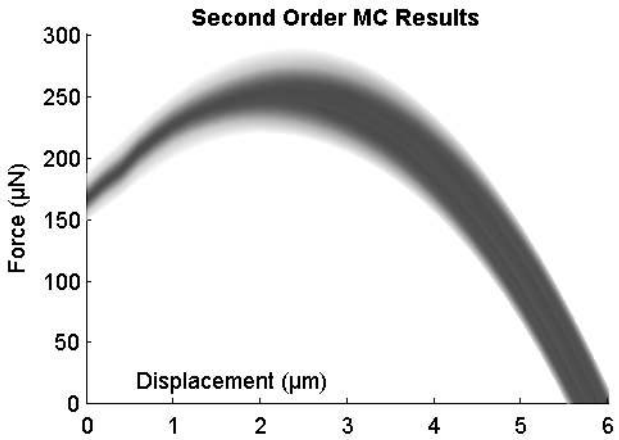

Figure 6.15 Shaded probability plot for visualizing Monte Carlo simulation results.

The second step is to perform a Monte Carlo simulation using the metamodel. To create the design matrix for the Monte Carlo simulation, the results from the simulation in Stage 1 are combined with independent random samples for E and S_r. This ensures that the we are taking into account the correlation between A and I_z. After assembling the matrix of regressors, **X**, as explained in Section 6.4.1, evaluating the results using the metamodel is simply a matter of performing a matrix multiplication

$$\Delta\mathbf{Y} = \mathbf{XB} \tag{6.29}$$

where **B** is a 14 x 4 matrix of regression coefficients calculated using Equation (6.15), and $\Delta\mathbf{Y}$ is a 50000 x 31 matrix where each row represents a single force-displacement curve.

To visualize the results of the simulation, a quantile function (Appendix A.3) can be used to generate probabilities contours. Figure 6.15 shows a probability plot in which

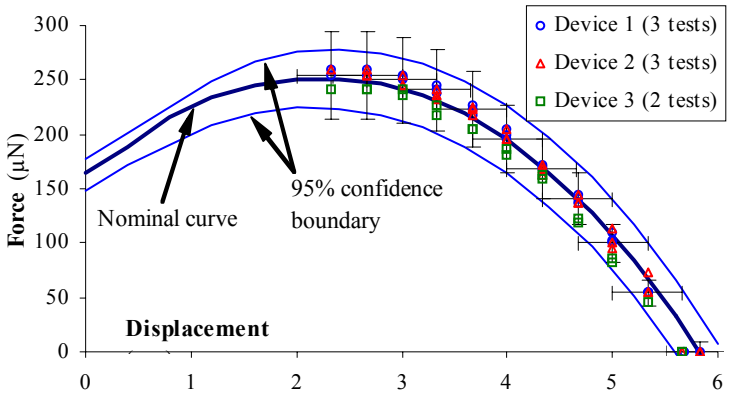

Figure 6.16 Model validation using a 95% confidence region from Monte Carlo simulation.

the higher density is represented as a darker grayscale value. Figure 6.16 shows the 95% confidence region, calculated using the 0.025 and 0.975 quantiles. For this problem, there is actually very little difference between the confidence regions shown in Figure 6.11 and Figure 6.16. However, if the distribution of the results is required, surrogate-based Monte Carlo simulation may provide a practical solution for cases involving computationally expensive finite element models.

CHAPTER 7 ROBUST DESIGN AND MODEL VALIDATION OF NONLINEAR COMPLIANT MEMS

Unless a device is designed as a sensor in which high sensitivity to variation is desired, the next logical step after quantifying the uncertainty via simulation is to find ways to reduce the uncertainty in order to improve reliability. In order to reduce the uncertainty, there are two main approaches. The first is to identify which sources of uncertainty are the most significant and attempt to reduce these variations. Since this is usually an expensive approach, an alternative method is to decrease the *sensitivity* of the device to variations.

This chapter proposes an approach for design stage uncertainty analysis, model validation, and robust optimization of nonlinear MEMS to account for critical process uncertainties including residual stress, layer thicknesses, edge bias, and material stiffness (based on the techniques described in Chapter 6). A fully compliant bistable micromechanism (FCBM) is used as an example, demonstrating that the approach can be used to handle complex devices involving nonlinear finite element models. The general shape of the force-displacement curve is validated by comparing the uncertainty predictions to measurements obtained from *in-situ* force gauges. A robust design is presented, with experimental results to verify that the performance is less sensitive to process variations, leading to an increase in reliability and yield.

7.1 Introduction

Research and development in the field of microelectromechanical systems (MEMS) usually involves fabrication processes that push the limits of technology or processes that are under development. In such cases, it is common to deal with large uncertainties due to lack of data, inherent variation in material properties and feature dimensions, variable loading conditions, adverse environmental effects, and other reliability issues (Tanner *et al*., 2000a; Gupta, 2000).

The use of compliant or flexible mechanisms has helped minimize the effects of friction, wear, and backlash in MEMS (Kemeny *et al*., 2002; Ananthasuresh *et al*., 1994). However, compliant MEMS can be highly sensitive to variations in material properties and geometry (Wittwer *et al*., 2002b).

Due to the high cost and slow turn-around during the prototyping stage of micro mechanism design, it is important to take uncertainty into account in order to increase first-pass success and shorten the product development cycle. Perhaps an even more important consideration is that profitable commercial production of batch-fabricated MEMS relies on high reliability and high yield (Delauche *et al*., 2002). If devices are not designed to be robust to variations, exhaustive post-fabrication screening or calibration is often required.

Considering uncertainty in simulation-based design of MEMS can aid in accomplishing a variety of objectives. These include:

- Increased first-pass success to shorten the product development cycle

- Model validation using both computer simulation and experimental data
- Improved understanding of device behavior
- Identification of important parameters for in-process monitoring (Muchow *et al*., 2002)
- Evaluation of device performance and reliability for feasibility studies
- Improved device performance through robust or reliability-based design optimization (Han and Kwak, 2001)
- Increased yield for reduction of production costs (Delauche *et al*., 2002)

This chapter proposes an approach for design stage uncertainty analysis, model validation, and robust optimization of nonlinear MEMS to account for critical process uncertainties including residual stress, layer thicknesses, edge bias, and material stiffness. A fully compliant bistable micromechanism (FCBM) is used as an example to demonstrate that the approach can be used to handle complex devices involving nonlinear finite element models in which the effects of uncertainties may vary with displacement. Experimental results are used for model validation and to verify that the performance of the robust design is less sensitive to uncertainties.

Methods for uncertainty analysis (Coleman and Steele, 1999), reliability-based design (Kuo *et al*., 2001; Haldar and Mahadevan, 2000a, 2000b), robust optimization (Parkinson *et al*., 1993), and sensitivity analysis (Saltelli *et al*., 2000) are well-established, and there is increasing interest in applying these methods in MEMS. Much of the existing literature pertaining to uncertainty analysis in MEMS has to do with microsystem metrology, where geometries and basic structural material properties, such as Young's modulus, fracture strength, and residual stress are extracted from other measurable quantities or electronic probing (Wittwer *et al*., 2002a; Baker *et al*., 2002; Pryputniewicz *et al*., 2002;

Jensen *et al*., 2001a; Allen and Johnson, 2001; Tanner *et al*., 2000a; Gupta, 2000; Johnson *et al*., 1999; Gianchandani and Najafi, 1996; Mirfendereski *et al*., 1993). In most of these cases, basic uncertainty and sensitivity analysis methods are used to determine measurement error and compare which process variations contribute the most to measurement uncertainty. Schenato *et al*. (2001) discussed other approaches for variation analysis in MEMS, including the use of Monte Carlo simulation for probabilistic analysis and a robust optimization approach for deterministic (worst-case) analysis. Monte Carlo simulation is a useful approach for tolerance analysis in MEMS (Muchow *et al*., 2002; Germer *et al*., 2002) particularly for analytical or computationally efficient models. A variety of software tools for statistical simulation and optimization are in development, with much of the emphasis on integration with existing MEMS analysis tools (Germer *et al*., 2002, Delauche *et al*., 2002; Schenato *et al*., 2001).

Designing for reliability and robustness is becoming an important topic in MEMS as the field matures and more emphasis is placed on developing reliable commercial applications. Han and Kwak (2001) presented the use of robust optimization in the design of a microgyroscope using Monte Carlo simulation to compare predicted yields. Delauche *et al*. (2002) are evaluating a variant of the Taguchi industrial approach for parametric yield optimization. Liu *et al*. (2002) used analytical equations to determine the effects of feature width variation on MEMS resonators and developed analytical equations for making resonators robust to width variations. Mawardi and Pitchumani (2004) later applied a more general robust optimization approach to the design of MEMS resonators. Maute and Frangopol (2003) combined topology and reliability-based design optimization, providing a

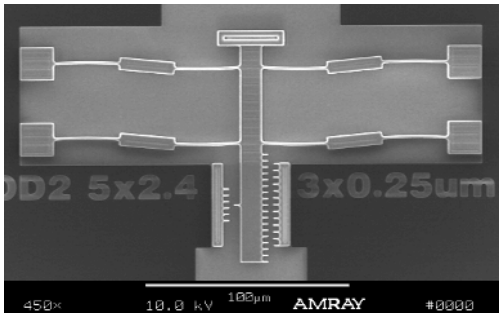

Figure 7.1 Scanning electron micrograph of a fully compliant bistable mechanism in its second stable position. Position measurements are made using the attached vernier.

stochastic method for compliant MEMS design. This technique takes advantage of modern reliability-based design methods.

Reliability assessment requires an accurate knowledge of the distributional form of the uncertainties, clearly defined metrics and performance specifications, and a valid model. In MEMS, these conditions are rarely ever met, so the reliability or probability of success can be a subjective metric. More work is needed to characterize uncertainties, validate models, and demonstrate the importance of considering uncertainty during design.

7.2 FCBM Model and Uncertainties

Bistable mechanisms are advantageous for use in microsystems because power is only required during actuation of the device. This makes them useful in a wide range of applications, including components in switches and relays (Gomm *et al*., 2002; Kruglick and Pister, 1998), optical switches (Hoffman *et al*., 1999b; Jang *et al*., 1996), nonvolatile memory (Hälg, 1990), and discrete sensors (Saif, 2000).

Figure 7.1 shows a scanning electron micrograph of a fully compliant bistable mechanism (FCBM) fabricated using the SUMMiT V™ process. The device is shown in

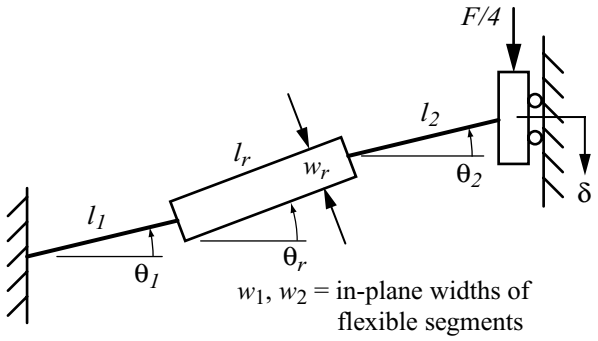

Figure 7.2 Schematic showing the parameterization of the FCBM quarter-model.

its second stable position with the attached vernier used to make position measurements. The schematic in Figure 7.2 shows the design parameters that define the mechanism topology. The topology is similar to that presented by Jensen *et al*. (2001b), but without side springs at the anchor points. The device is planar, consisting of three layers of polycrystalline silicon (polysilicon) that together form an out-of-plane thickness, t = 4.75 μm. The nominal parameters for the three designs discussed in this chapter are summarized in Table 7.1. The values for residual stress (S_r), Young's modulus (E), Poisson's ratio (ν), and profile offset (p_{offset}) are discussed in detail in Sections 7.2.2 and 7.2.3.

Table 7.1 Parameter values for three designs.

Variable	Design 1 (high force)	Design 2 (sensitive)	Design 3 (optimal)
l_1 (μm)	13.7	15.5	29
l_2 (μm)	13.7	15.5	29
l_r (μm)	103.3	100	25
θ_1 (deg)	2.44	2	4.12
θ_2 (deg)	2.44	2	4.71
θ_r (deg)	2.44	3	2.42
w_1 (μm)	1.4	2.5	1.4
w_2 (μm)	1.4	2.5	1.4
w_r (μm)	6.2	6.2	6.2
p_{offset} (μm)	0.1	0.1	0.1
t (μm)	4.75	4.75	4.75
E (MPa)	164000	164000	164000
v	0.23	0.23	0.23
S_r (MPa)	-10	-10	-10

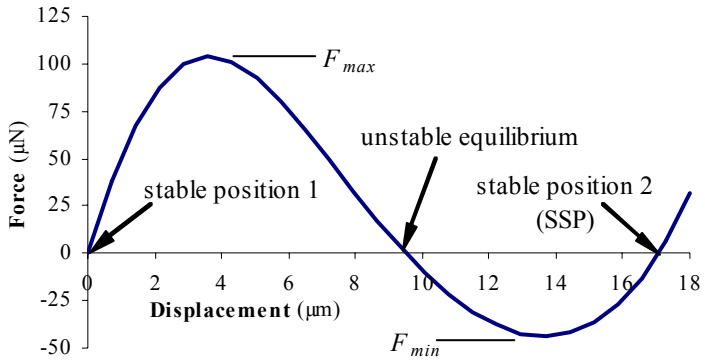

Figure 7.3 Force vs. displacement curve for a bistable mechanism.

The force vs. displacement relationship for this mechanism is nonlinear due to large deflections and stress stiffening, or the complex relationship between longitudinal and transverse deformation of the flexible segments. Therefore, a nonlinear finite-element model using beam elements was created to analyze the mechanism. Figure 7.3 shows the graph of the applied force F required to maintain static equilibrium at 25 discrete displacements, δ. These displacements correspond to the load steps used in the nonlinear solution. The maximum force, minimum force, and x-intercepts are found through interpolation.

A variety of force-displacement curves can be generated using the FCBM topology, but the mechanism is bistable only when the minimum force $F_{\min}$ is negative. For bistable switches, it is desirable to maintain an adequate contact force, so the contact is usually placed at the position corresponding to $F_{\min}$. For discrete positioning, a contact or mechanical stop can be used, but friction and wear problems can be avoided by using the second stable position (SSP). When choosing an actuator, the forces and the displacement required to toggle the mechanism must also be considered.

7.2.1 Modeling Assumptions

An important aspect of finite-element modeling of compliant MEMS is the choice of boundary conditions and other assumptions. The boundary conditions, element type, element size, plane stress or plane strain conditions, and material properties (i.e. linear elasticity, isotropy, and homogeneity) can affect the systematic error, making it important to experimentally validate the model.

Using symmetry and two beam-pairs as shown in Figure 7.1 helps constrain the second buckling mode by preventing rotation of the shuttle. This is an important requirement to achieve bistability as discussed by Que *et al*. (2004) for curved-beam bistable mechanisms. Symmetry enables the use of a quarter-model where the shuttle is treated as a slider with only one degree of freedom. This model assumes that the only significant force on the mechanism is the in-plane applied force, *F*. In order to prevent deflection and buckling perpendicular to the desired plane of motion, the moment of inertia for in-plane bending must be kept smaller than that for out-of-plane bending or buckling.

Support compliance can be an important factor in some MEMS devices (Jensen *et al*., 2001a). The schematic shown in Figure 7.2 assumes a perfectly rigid support, but techniques based upon those in Gill *et al*. (1998) and Baker *et al*. (2002) have been used to minimize bending in the support.

Additional compliance due to local elasticity at the junctures of flexible beams and supports and at discontinuities in cross-sections can affect the behavior of compliant MEMS (Wittwer and Howell, 2004; Allen and Johnson, 2001). In the case of in-plane bending, the effect can be mitigated by using optimally sized fillets (Wittwer and Howell,

2004), making the idealized beam element model more accurate. The alternative would be to use 2D plane elements or a full 3D model, with a loss in computational efficiency. Besides computation efficiency, an advantage of using beam elements is the simplicity in creating *parametric* models that are important for design-stage uncertainty analysis.

7.2.2 Residual Stress and Material Properties

Residual stress. Residual stress in polysilicon can be an important factor to consider in the design of compliant MEMS, particularly those with fixed-fixed boundary conditions. With these boundary conditions, residual stress is known to induce buckling (Masters *et al*., 2001). Baker *et al*. (2002) have presented some data for the SUMMiT V™ process which gives a rough idea of an amount of residual stress to consider. For this chapter, a residual stress of S_r = -10 MPa (compressive) is used, with a standard deviation of 5 MPa[1] (see Table 7.2).

Young's modulus. A significant amount of research has been done to measure the modulus of polysilicon (Sharpe *et al*. 2001; Sharpe *et al*. 1998), with reported values ranging from 135 to 173 GPa. Since the material properties of polycrystalline materials are known to be dependent upon grain size, isotropy, and homogeneity, the actual value for the mod-

Table 7.2 Summary of uncertainties.

Parameter	Nominal	St. Dev.	Reference
S_r	-10 MPa	5	Baker *et al*., 2002
E	164 GPa	3.2	Jensen *et al*., 2001
t	4.75 µm	0.065	Limary *et al*., 1999
p_{offset}	0.1 µm	0.04	Sandia ..., 2004

1. Baker *et al*. (2002) found that the residual stress varied across three adjacent die locations on a wafer by 2.5 MPa. It is reasonable to assume that variation across the entire wafer would be larger, but more data is needed.

ulus is dependent upon the specific fabrication process. For the SUMMiT V™ process, Jensen *et al*. (2001a) measured the modulus to be $E = 164$ GPa, with a standard deviation of 3.2 GPa (see Table 7.2). A value of $\nu = 0.23$ is used for Poisson's ratio.

Fracture strength. The fracture strength of polysilicon has been shown to vary significantly (Sharpe *et al*., 1998; Sharpe *et al*., 1999) with measurements ranging from 1 to 3 GPa. The strength can be affected by specimen size, with larger specimens having lower strength, likely due to the higher probability of defects (Sharpe *et al*. 2001). A conservative design approach uses a maximum stress of 1 GPa, unless sufficient data is available to make more accurate reliability predictions.

7.2.3 Geometric Variations

Layer thicknesses. Uncertainty in film thicknesses of polysilicon deposited using LPCVD is a result of variations in deposition rates, run-to-run drifts in the equipment, and uniformity across a wafer (Elbrecht and Binder, 1999). Limary *et al*. (1999) presents data for polysilicon film thicknesses and uniformity for the SUMMiT V™ process. The mechanisms described in this paper are planar, consisting of two layers of polysilicon, with a nominal overall thickness of $t = 4.75$ μm. Based upon the reported data for SUMMiT V™, we assume the overall thickness to have a standard deviation of 0.065 μm (see Table 7.2).[2]

2. The thickness of sacrificial oxide layers planarized using chemical-mechanical polishing (CMP) can also be affected by pattern density (Hetherington and Sniegowski 1998). These layers are ignored in the FCBM model because the in-plane force vs. displacement behavior is only significantly affected by the structural polysilicon layers.

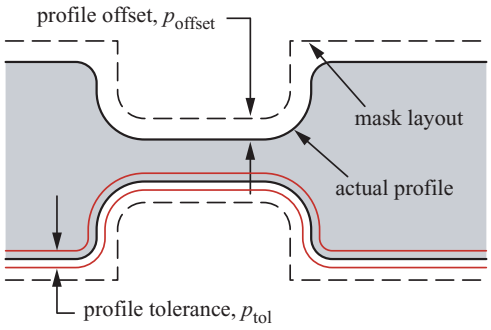

Figure 7.4 Profile offset and tolerance zone resulting from surface micromachining of polysilicon features (effect is exaggerated for visualization purposes).

Profile offset. Surface micromachining of polysilicon features is known to result in a profile offset, or edge bias, due to photolithography exposure, etch undercut, proximity and pattern density (Tanner *et al*., 2003; Wittwer *et al*., 2002b; Gupta, 2000; Limary *et al*., 1999; Liebmann *et al*., 1997). This effect, shown exaggerated in Figure 7.4, can affect both line widths and the lengths of flexible segments. The nominal profile offset, p_{offset}, is commonly assumed to be 0.1 µm in the SUMMiT V™ process, but values ranging from 0.05 µm (Limary *et al*., 1999) to 0.15 µm (Tanner *et al*., 2003) have been used. From the reproducibility data for SUMMiT V™, available in the Sandia MEMS Advanced Design Short Course, the profile tolerance zone shown in Figure 7.4 (at 95% confidence) is taken to be ±0.08 µm based upon a pooled standard deviation of 0.04 µm (combining measurements from wafer-to-wafer and lot-to-lot). This means that the uncertainty for the width of a flexible beam is about ±0.16 µm, even after taking into account the nominal profile offset. In addition to the reproducibility data, Tanner *et al*. (2003) have shown that line widths can vary significantly across a wafer, generally in a radial pattern from the center to the edge, with a difference in the line width as much as 0.2 µm.

An important point to consider when dealing with uncertainty in line widths is that the profile offset results in a correlation between line widths of different beams within a mechanism. Although the profile offset may vary across a wafer, local variation within a wafer is usually much smaller than the stated ±0.08 μm tolerance. More data is needed to determine the actual die-level and device-level variation. For the purposes of this chapter, the variation in beam widths and lengths of flexible segments within a device are assumed to be linearly correlated, based upon the relationship

$$\Delta w_1 = \Delta w_2 = \Delta w_r = \Delta l_r = -\Delta l_1 = -\Delta l_2 \tag{7.1}$$

where $\Delta w = 2p_{\text{offset}}$ represents the difference between the fabricated and as-drawn width of a beam due to the profile offset.

Fillets and rounding. In addition to a profile offset, photolithography and etching processes are known to result in fillets and rounded corners. Rounding of corners usually has very little effect on the stress distribution of compliant mechanisms, but fillets are known to affect the stiffness and stress concentrations (Wittwer and Howell, 2004; Pilkey, 1997). As mentioned in Section 7.2.1, adding optimally sized fillets to the mask layout helps mitigate the effect of local elasticity, making beam element models more accurate. The increase in size of the fillet due to the profile offset can be taken into account in the design and layout. However, since most flexible segments in MEMS are fairly slender, the effect of the local elasticity and fillet will often be negligible compared to other uncertainties.

Cross-sections. The cross-sections of polysilicon beams are rarely perfectly rectangular, but rather trapezoidal due to tapered side walls (Mirfendereski *et al*., 1993; Sharpe *et al*.,

2001; Wittwer *et al*., 2002b). This can be important when calculating moments of inertia and other area properties. The side walls of etched polysilicon features in SUMMiT V™ are close to vertical, so it is usually sufficient to assume that the beams are rectangular. Surface roughness, tapering, and bowing along the length of flexible beams can lead to non-constant cross-sections, but uncertainty in the width due to edge bias is typically much larger than these effects.

7.3 Uncertainty and Sensitivity Analysis

7.3.1 Uncertainty analysis

Since we are using a parametric finite element model, uncertainty analysis is performed by treating the model as a generic function that takes a vector of uncertain or variable inputs $\mathbf{x} = [x_1, x_2, \ldots, x_n]^T$ and returns a vector of output (response) variables $\mathbf{y} = [y_1, y_2, \ldots, y_p]^T$. For the bistable mechanism, the vector **y** represents the force evaluated at discrete displacements. Additional outputs such as the maximum force, minimum force, and *x*-intercepts can also be included in the analysis.

The approach used in this chapter is based upon the general uncertainty analysis method described by Coleman and Steele (1999). This method involves creating a first-order Taylor series expansion about the nominal values of **x** and **y**, followed by the use of the propagation of variance equation. Stating this equation in matrix notation, the estimate of the covariance of **y** can be found using

$$\mathbf{S}_y = \theta \mathbf{S}_x \theta^T \tag{7.2}$$

where θ is the sensitivity matrix of size p x n and $\mathbf{S}_x$ is the covariance of **x**. If the input uncertainties are independent (i.e. no correlation), then $\mathbf{S}_x$ is a diagonal matrix where each element s_{ii} is the variance of x_j. The elements θ_{ij} represent the sensitivities $\partial y_i / \partial x_j$ from the coefficients of the Taylor series expansion. These sensitivities can be found numerically using finite-difference (Glancy and Chase, 1999) or multivariate polynomial regression (Jin *et al*., 2003; Simpson *et al*., 1997; Myers and Montgomery, 1995).

To determine the relative effects of the uncertainties on the total variance, Equation (7.2) can be written in expanded form as

$$\mathrm{var}(y_i) = \sum_{j=1}^{n} \left(\frac{\partial y_i}{\partial x_j}\right)^2 s_{jj} + 2 \sum_{j=1}^{n-1} \sum_{k=j+1}^{n} \left(\frac{\partial y_i}{\partial x_j}\right)\left(\frac{\partial y_i}{\partial x_k}\right) s_{jk} \tag{7.3}$$

where $s_{jk} = 0$ if the inputs are independent. To compare the variance contributions, the individual terms in Equation (7.3) are normalized by dividing by the total variance, $\mathrm{var}(y_i)$.

The simplest approach for uncertainty analysis of the FCBM is to ensure that the vector **x** is an independent set of parameters, such as $\mathbf{x} = [E, t, S_r, p_{offset}]^{\mathrm{T}}$. We would then define a corresponding vector $\mathbf{s} = [3200, 0.065, 5, 0.04]^{\mathrm{T}}$ as the vector of standard deviations of **x**. The covariance matrix $\mathbf{S}_x$ is then formed by setting $s_{ii} = s_i^2$.

An alternate approach that allows us to observe the relative contributions of the lengths and widths is to use $\mathbf{x} = [E, t, S_r, w_1, w_2, w_r, L_1, L_2, L_r]^{\mathrm{T}}$, where the lengths and

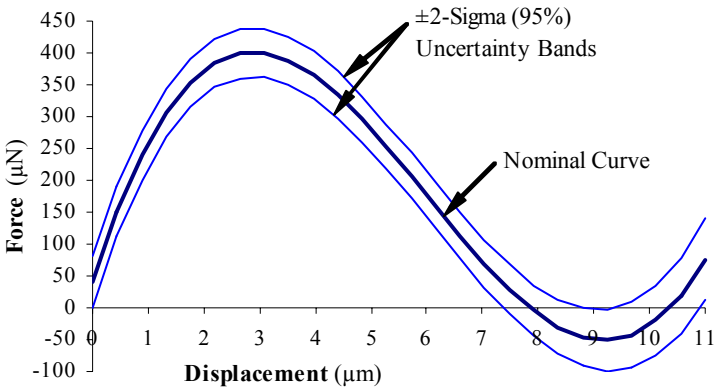

Figure 7.5 Force uncertainty for design 2 represented as 2-sigma error bands.

widths are correlated. It can be shown that L_1, L_2, L_r, and w_r are not significant compared to w_1 and w_2, so for this chapter we use $\mathbf{x} = [E, t, S_r, w_1, w_2]^{\mathrm{T}}$. Due to the profile offset described in Section 7.2.3, the standard deviations of w_1 and w_2 are twice that of the profile offset, with a correlation coefficient of 1. This leads to the covariance matrix

$$\mathbf{S}_x = \begin{bmatrix} 3200^2 & 0 & 0 & 0 & 0 \\ 0 & 0.065^2 & 0 & 0 & 0 \\ 0 & 0 & 5^2 & 0 & 0 \\ 0 & 0 & 0 & 0.08^2 & 0.08^2 \\ 0 & 0 & 0 & 0.08^2 & 0.08^2 \end{bmatrix} \tag{7.4}$$

A detailed discussion of covariance and correlation matrices can be found in Rencher *et al*. (1995, pp. 65-70).

When using Equation (7.2) to estimate the uncertainty in the force, we typically only use the diagonal elements of $\mathbf{S}_y$ which represent the force variance at each discrete displacement. Using the variance, we can plot an estimate of the 95% confidence band based upon limits of $\pm 2\sqrt{s_{ii}}$, as shown in Figure 7.5 for Design 2 of the FCBM.

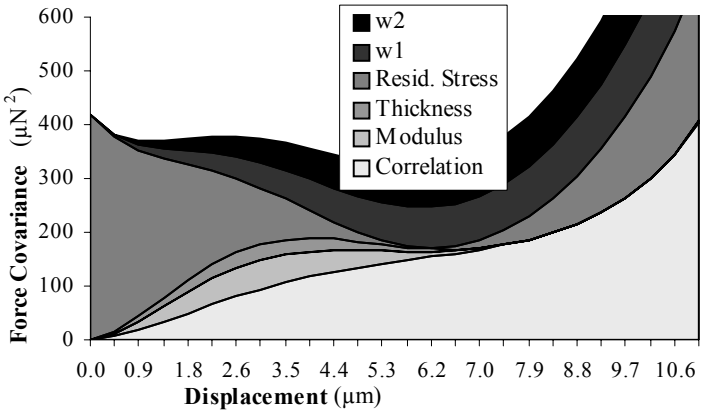

Figure 7.6 Uncertainty contributions for Design 2 visualized using an area chart (including correlation).

For the intended application of the FCBM as a component in a discrete sensor, it was desirable to have the minimum force be as close to zero as possible, while remaining reasonably certain that the fabricated devices would be bistable. In addition, the force output of the electrostatic actuator used by the sensor was limited to 50 μN. The problem with Design 2 is that the uncertainty in the minimum force and second stable positions is very large, so without fabricating multiple versions of the device, we could not be confident that all the devices would be bistable and have a minimum force between 0 and −50 μN.

7.3.2 Sensitivity Analysis

It is often helpful to evaluate a design based upon the sensitivity of performance with respect to individual variations. There are many methods for sensitivity analysis, with a good overview provided by Saltelli *et al*. (2000).

Sensitivity analysis often involves the creation of pie graphs or bar charts to visualize and rank the effects of individual uncertainties on the total variance. For nonlinear finite element models, these sensitivities may change with time or displacement, so area

charts (or stacked line graphs) can provide a helpful visualization tool (Wittwer *et al*., 2002a). Figure 7.6 shows a graph of the force covariance for Design 2 of the FCBM, including the individual effects of modulus, thickness, residual stress, beam widths, and correlation in the beam widths.

The area chart is a graphical representation of Equation (7.3), with the magnitude of each term in the equation represented by the thickness of a shaded region in the chart. The total force variance is the sum of the stacked areas. A single area, included as the lower area in the chart, is used to represent the sum of the terms in which the input covariance is non-zero ($s_{jk} = 0$). For this example, the only non-zero input covariance is the one associated with the beam widths.

Figures 7.5 and 7.6 provide valuable information about the behavior of the FCBM. Figure 7.6 shows that the uncertainty in the minimum force and SSP is due mainly to variations in the beam widths, with correlation compounding the problem. We have not included additional independent random variation in the widths, so the sum of the contributions of the widths and the covariance represents the total contribution of the profile offset uncertainty. It is interesting that unlike the *thickness* and *modulus*, the variance due to *width* uncertainty is not necessarily a function of the magnitude of the force, as one might expect from results obtained from the analysis of linear springs (Wittwer and Howell, 2002). Another point of interest is that the residual stress is the dominant source of variation at the initial position, but the device is practically insensitive to residual stress at a displacement of 6.0 μm^3. This displacement does not correspond to the unstable equilibrium position (7.9 μm), nor does it correspond exactly to the sum of the vertical components of

the beams (6.3 μm) from Figure 7.2. The peculiarities in these results led to an investigation of whether robust optimization could be used to find a design that would be less sensitive to process variations for a specific set of design constraints.

7.4 Model Validation

Obtaining experimental measurements is essential for validating the FCBM model, discovering possible lurking variables, and gaining confidence in the simulation. Traditional statistical model validation methods involve the replication of an experiment to gather a sufficient amount of data to estimate uncertainty and test whether the model agrees with the data. Due to the cost and difficulty of obtaining experimental data in MEMS, it is often not practical to obtain a sufficient amount of data required for statistical model validation.

A number of researchers have described how simulation-based uncertainty models can aid in model validation when experiments are expensive or time-consuming to repeat (Hills and Trucano, 1999; Doebling *et al*., 2002; Baghdasaryan *et al*., 2002). First, the model is used to predict the uncertainty based upon parameter variations and other measurement uncertainties. In this way, even a single experimental data point can be used to help validate models, by determining whether the measurement falls within the confidence region predicted by the uncertainty analysis[4]. This approach was used to validate the FCBM force-displacement prediction.

---

3. Found through quadratic interpolation of the variance contribution vs. displacement. From the graph, the minimum appears to be at 6.2 μm.
4. Statistical hypothesis testing can then be used to decide whether the model should be rejected, or whether it is consistent with the experimental results. Baghdasaryan *et al*. (2002) applied this approach to a sheet metal flanging process, showing that reducing the number of physical tests to one and using efficient computational uncertainty analysis techniques, the model could be validated over more design settings.

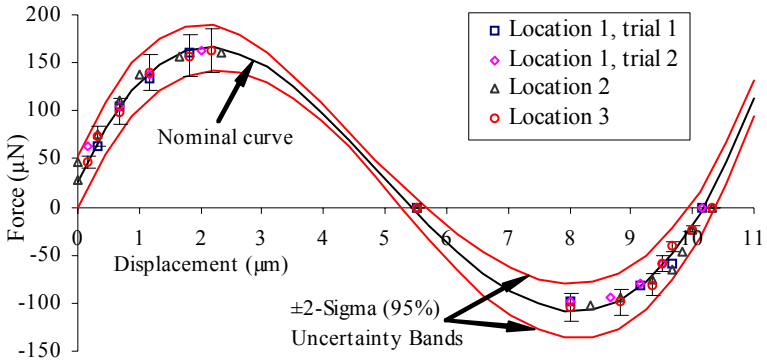

Figure 7.7 Model validation of Design 1 using experimental data obtained from *in-situ* micro force gauges. The data is contained within the estimated 95% uncertainty bands.

7.4.1 Force-Displacement Model Validation

To obtain force-displacement data for the FCBM, *in-situ* micro force gauges similar to those described in Wittwer and Howell (2002a) were used. Force measurements were obtained by measuring the displacements of the gauge and backing out the force based on the material properties and dimensions of the gauge. Tests were performed for Design 1 at three different locations on the wafer, and repeated at one of these locations. The results are shown in Figure 7.7 along with the 95% uncertainty bands representing the systematic uncertainty in the fabricated mechanism as estimated from the design-stage simulation. The measurement uncertainty for the force was ±14% (shown as error bars on the data from location 3). The uncertainty in the displacements from vernier measurements was ±0.17 μm. This data provides an adequate validation of the general shape of the force-displacement curve.

7.4.2 Uncertainty Model Validation

Because edge bias and residual stress are known to vary significantly across a wafer, measurements were taken at multiple locations in order to determine if the spread

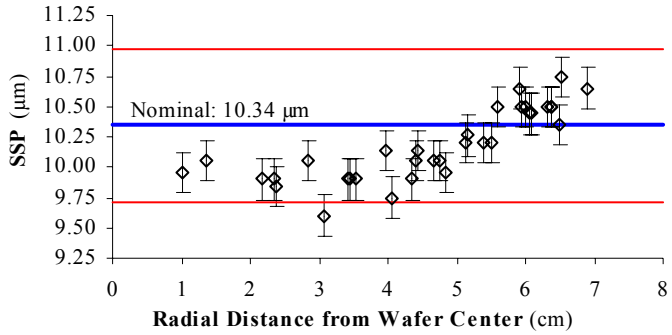

Figure 7.8 Measurements of the second stable position (SSP) for Design 2 vs. the radial distance from the wafer center. Uncertainty model predictions shown as 10.34 ±0.32 µm.

of data was similar to the predicted uncertainty. When using *in-situ* force gauges, the force measurement uncertainty can be correlated with the uncertainty in the device being characterized. Therefore, without measuring the actual dimensions and properties of each gauge that is used, one cannot make good statistical comparisons between identical devices at different locations on the wafer. A more practical approach for validating the uncertainty predictions was to measure the second stable position (SSP), which involved toggling the mechanism and reading the displacement directly from verniers on the device.

Figure 7.8 shows measurements of the SSP taken at 34 locations across a wafer, plotted vs. the radial distance of the device from the wafer center. The nominal SSP was 10.34 µm with an estimated 95% uncertainty interval of [9.71, 10.90] µm, shown as horizontal lines in Figure 7.8. The error bars on the data points represent 95% confidence in the displacement measurements, or ±0.17 µm from the vernier readings. The repeatability of the measurements was less then the resolution of the vernier, resulting in identical measurements of the SSP for repeated tests.

The spread of the data compared to the predicted uncertainty in Figure 7.8 suggests that our uncertainty model, or the assumed process variations and the manner in which these variations affected the performance of the device, was reasonable[5]. The effects of residual stress and edge bias variation cannot be separated, but the plot in Figure 7.8 shows a definite radial trend. Given that Design 2 is theoretically more sensitive to edge bias variation and the fact that an increase in the profile offset leads to an increase in the SSP, the trend is consistent with that found in Tanner *et al*. (2003) where the profile offset was found to be largest at the edge of the wafer.

7.5 Robust Design Optimization

The next logical question after analyzing uncertainty and sensitivities is whether the variation in the device performance can be reduced. Although reducing the variation in the residual stress and profile offset would be one solution, it may be too expensive or not currently possible to do so. Another approach is to make the device more robust to variation by modifying design parameters, an approach made popular in the 1980s by Genichi Taguchi (Taguchi *et al*., 1989).

Designing for robustness is often an optimization problem, particularly when the relationship between the output performance and the input parameters is complex. In order to design for robustness, we used a nested approach, where the full uncertainty model was wrapped inside of a gradient-based optimization routine. While not necessarily the most efficient optimization formulation, it was highly practical since no modifications had to be

5. These results do not directly validate the uncertainty estimations at every location along the force-displacement curve, but we can infer from these results and Section 7.4.1 that the uncertainty model is reasonable.

made to the uncertainty model. Eldred *et al*. (2002) provide other formulations for surrogate-based optimization under uncertainty that may be more efficient.

7.5.1 Optimization Formulation

The objective function for the optimization problem was to minimize the variance of the minimum force, or minimize$(\mathrm{var}(F_{\min}))$. The design variables and limits are given in Table 7.3 The constraints, summarized in Table 7.4, included the requirements necessary for a specific application as a component in a discrete sensor. The maximum force $F_{\max}$ was chosen based upon the output capabilities of a specific thermal microactuator. The requirements for $F_{\min}$ and the displacement at the point of minimum force $x(F_{\min})$ were chosen to ensure bistability while remaining within the force output capabilities of a specific electrostatic actuator. The maximum stress $S_{\max}$ in the device had to be low enough to prevent failure.

Although uncertainty in maximum stress could be included in the analysis, using a deterministic safety factor for the constraint was sufficient for this problem. The con-

Table 7.3 Design variables for optimization.

Variable(s)	Min	Max
w_1, w_2	1.4 μm	2.0 μm
$\theta_1, \theta_2, \theta_r$	1 deg	10 deg
l_1, l_2	10 μm	30 μm
l_r	25 μm	75 μm

Table 7.4 Optimization constraints.

Constraint	Min	Max	Result
$F_{\min}$	-25 μN	-15 μN	-15.6 μN
$F_{\max}$	75 μN	125 μN	121 μN
$x(F_{\min})$	6 μm	8 μm	6.3 μm
$S_{\max}$	-	1000 MPa	870 MPa

straints for the other variables were also soft constraints chosen as guidelines and not hard specification limits. For problems in which it is desirable to ensure that the design remains within the constraint boundaries even under uncertainty, an alternative reliability-based or robust optimization formulation (Eldred *et al*. 2002; Parkinson *et al*., 1993) could be used, such as specifying a stochastic interval for a 3-sigma level reliability on $F_{\max}$ as

$$[50 + n\sqrt{\text{var}(F_{\max})} \leq F_{\max} \leq 150 - n\sqrt{\text{var}(F_{\max})}] \tag{7.5}$$

where $\text{var}(F_{\max})$ is the variance estimated from the nested uncertainty analysis, and $n = 3$ represents the 3-sigma or 99.73% reliability level (assuming a normal distribution).

Optimization of the FCBM resulted in Design 3 with the parameters given in Table 7.1. The force-displacement curve and uncertainty bands are shown in Figure 7.9(b) compared to Design 2 in Figure 7.9(a). The simulation predicts that the minimum force and second stable position are much less sensitive to process variation than Design 2, and this is validated experimentally in the next section.

It is interesting that the optimization resulted in the widths of the flexible segments binding on the minimum value. These results are counterintuitive, since the general approach for reducing sensitivity to variations is to reduce the *relative* uncertainty by increasing the beam width, rather than decreasing it[6]. While it is reasonable to hypothesize that a nonlinear mechanism could have such behavior, the fact that an actual device has

6. Part of the reason for the narrow beams compared to Design 2 is the constraint on the maximum force and the stress. However, neither the maximum force nor the length of the flexures were binding constraints. Intuitively, one might expect the length and the force to be binding since using a wider beam reduces the relative (percent) uncertainty in the beam width.

been shown to have this effect opens up the question of whether there are not other micro devices that may exhibit such behavior.

7.5.2 Robust Design Validation

One of the first steps taken to validate the robust design was to use a more accurate simulation. The approach described in Section 7.3 is based upon a linear expansion at the nominal design point. For a more precise estimate of the uncertainty, we used a surrogate-based (metamodeling) method in which a second-order surface response was first created, followed by a Monte Carlo simulation (Doebling *et al*., 2002; Baghdasaryan *et al*., 2002; Iman and Helton, 1984). The 95% uncertainty bands shown in Figure 7.9 come directly from the results of the Monte Carlo simulation, assuming normal distributions for the inputs. The differences between these results and those from Section 7.3.1 were insignificant.

To experimentally validate that Design 3 is more robust, a subsequent experiment to that described in Section 7.4.2 was performed in which Design 2 and Design 3 were fabricated side-by-side on the same die. Figure 7.9 shows the measurements of the SSP for both devices at multiple locations across the wafer. Using verniers, it was possible to resolve displacement measurements to 0.125 μm, so the number of data points shown in Figure 7.9 is actually 29 points for the sensitive device (Design 2) and 32 points for the

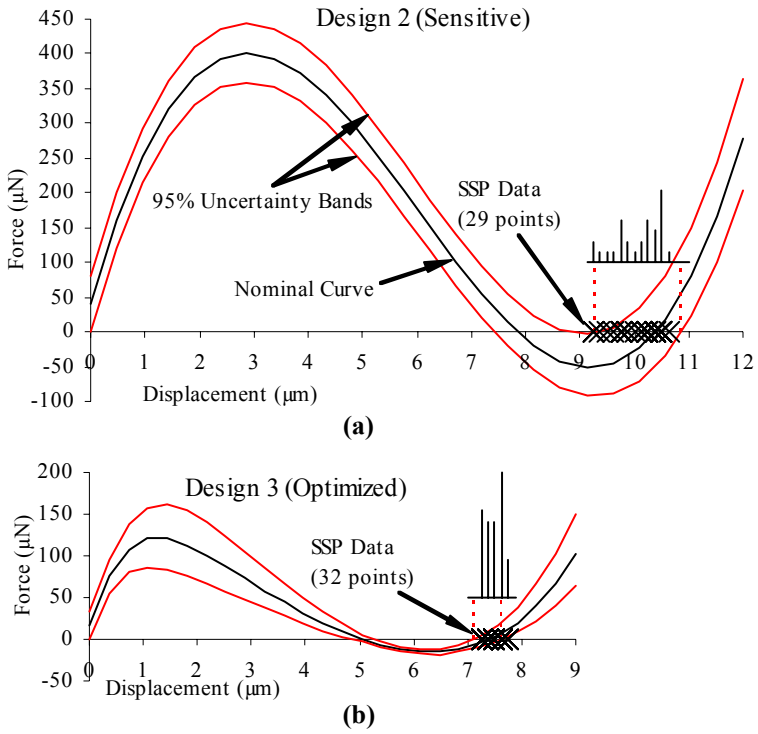

Figure 7.9 Measurements of the SSP for (a) Design 2 and (b) Design 3, with histograms to show the distribution of the data.

optimized device (Design 3). The distribution of the data is shown using histograms, since many of the data points overlap.

The spread of the SSP measurements in the optimized device is clearly less than that of Design 2, showing that the optimized device is indeed more robust. The fact that the spread of the data is close to the prediction provides further evidence that the uncertainty model is reasonable. The significance of this is further demonstrated by the bistable behavior of the devices. Although the nominal minimum force for Design 2 was much farther from zero than Design 3, it is also more sensitive to variation. This resulted in 3 of the Design 2 devices not being bistable, while *all* of the Design 3 devices were bistable. The location of the minimum force, $x(F_{\min})$, for the 3 non-bistable devices relative to the

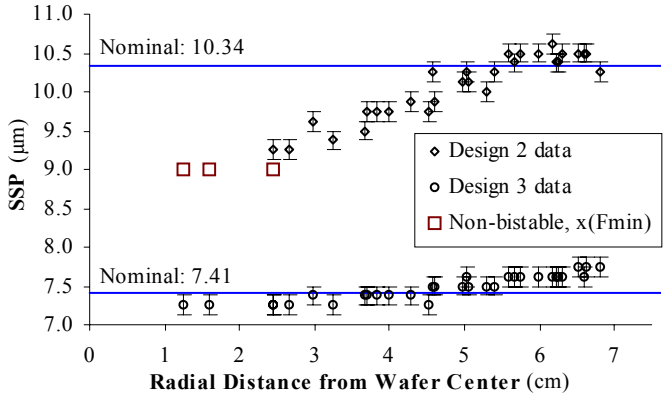

Figure 7.10 Measurements of the second stable position (SSP) for Design 2 and Design 3 vs. the radial distance from the wafer center.

wafer center is shown in Figure 7.10. The spread of the SSP data for the two designs is consistent with the trend observed in the previous experiment (see Figure 7.8).

7.6 Conclusions

An approach for uncertainty and sensitivity analysis of nonlinear micromechanisms was described that can provide valuable information about the behavior of a device with respect to both process variations and design variables. The uncertainty model of the FCBM shows that the sensitivities can change with displacement, and that correlation in geometric variations due to edge bias can be a significant factor to consider. In addition to visualizing the uncertainty in force vs. displacement for nonlinear finite element models, this approach could also be applied to position vs. voltage for electrostatic switches, or amplitude vs. frequency for dynamic models.

This work demonstrates the value of using process variation data in the design of MEMS. Robust design optimization does not necessarily require exact knowledge of actual process variations, but it is necessary to know what factors may be important to

consider in the analysis. The sources of uncertainty summarized in this chapter are highly process and design dependent, and since MEMS technologies improve and change over time, there will continue to be a need for uncertainty analysis, model validation, and design for reliability and robustness.

This chapter demonstrates the experimental validation of robust optimization for nonlinear compliant MEMS using a fully compliant bistable micromechanism as an example. Prior to the design of the robust device, the general shape of the force-displacement model was validated using *in-situ* force gauges on a mechanism with the same topology designed for use as a micro relay component (Design 1). Measurements of the second stable position on another design (Design 2) were taken at multiple locations on a wafer in order to help validate the uncertainty model. The uncertainty model was then nested inside of an gradient-based optimization algorithm using the variation in the minimum force as the objective function. A final experiment comparing Design 2 to the optimized device (Design 3) showed that although each device was subject to the same process variations, the performance of the optimized device was less sensitive to these variations. This demonstrates the importance of design stage uncertainty analysis and the feasibility of designing MEMS that are robust to the uncertainties associated with the fabrication process. The device used to demonstrate this approach has potential for use in force-threshold switches and discrete sensors, where robustness to variations can lead to an increase in reliability.

CHAPTER 8 CONCLUSIONS AND RECOMMENDATIONS

8.1 Conclusions and Contributions

The purpose of this dissertation was to develop approaches for simulation-based design of compliant micromechanisms to evaluate design performance under uncertainty, increase first-pass design success, validate models, and increase device yield.

A generalized analytical method was presented for uncertainty analysis of compliant MEMS where models consist of implicit systems of equations (Chapter 3). The approach was applied to a linear displacement bistable micromechanism and included a detailed discussion of the sources of uncertainty common in compliant MEMS. It demonstrated how performing design-stage uncertainty analysis could aid in achieving first-pass design success.

Much of the work in simulation-based design has to do with investigating non-idealities in order to reduce modeling error and identify causes for differences in model predictions and experimental results. Listed below are the main issues presented in this dissertation related to modeling of compliant MEMS:

- **Joint clearances.** (Chapter 3) A method for modeling the effects of clearances in compliant micromechanisms was developed, enabling first-pass design success of a linear displacement bistable micromechanisms. Com-

pliance results in a force-closed condition which makes clearance vectors dependent upon reaction forces at the joints.

- **Semi-rigid supports.** (Chapter 4) Localized elasticity at the junctures of flexible beams and semi-rigid supports can lead to significant modeling error when supports are assumed to be perfectly rigid. A method was developed to mitigate the effects of local elasticity in planar compliant mechanisms through the use of optimally sized fillets. This allows beam elements or classical analytical methods to be used without a significant loss of accuracy.
- **Non-ideal loading.** (Chapter 5) It was observed through experiment and demonstrated through simulation that non-ideal loading of thermal micro-actuators can lead to a significant decrease in the force output due to non-ideal buckling. Simulations were used to develop design rules to avoid this problem.
- **Asymmetry.** (Chapter 5) Monte Carlo simulation was used to show that asymmetry due to small variations in the cross-sectional properties of beams is a plausible cause for non-ideal buckling observed in some thermal microactuators.

An approach for uncertainty analysis of compliant MEMS was developed (Chapter 6) that can account for large relative uncertainties in complex models, while maintaining simplicity and transparency (ease of interpretation). Some of the specific contributions related to this approach are listed below:

- Use of multivariate multiple linear regression to create first and second-order surrogate models
- Visualization of relative uncertainty contributions via area charts, including correlation
- Inclusion of distribution information via surrogate-based Monte Carlo simulation

- Application of the approach for uncertainty analysis and model validation of nonlinear compliant mechanisms, including a thermal microactuator (Chapter 6) and a fully compliant bistable micromechanism (Chapter 7)

A quasi-object-oriented toolkit was developed in MATLAB to enable the implementation of various uncertainty, sensitivity, optimization, and computer experiment methods while treating the model as a "black box".

The main contribution of this dissertation was the demonstration that simulation-based design under uncertainty can enable the development of MEMS devices that are less sensitive to existing process variations. This approach was experimentally validated in a case study involving a nonlinear, fully compliant, bistable, micromechanism. Such an approach is particularly important for new technologies where there is little control over process tolerances. Not all devices can be made insensitive to variations in micro fabrication processes, and there are almost always trade-offs in performance. However, design-stage uncertainty analysis can provide valuable information about complex systems that might otherwise only be attainable through extensive testing.

8.2 Recommendations for Further Work

As explained in the introduction, simulation-based design under uncertainty requires (1) an understanding of the sources of errors and variation, (2) a parametric model that can be used for simulating effects of variation, and (3) an efficient means for running the computer experiment and analyzing the data. These three requirements are often more difficult to meet than designing based upon the prototype-testing-redesign cycle. This dissertation has demonstrated the value of design-stage uncertainty analysis in MEMS, and

additional work related to meeting the above requirements will be beneficial to compliant MEMS design.

8.2.1 Parametric Data

The amount of information available to MEMS designers regarding the types of errors and amount of variations within a given micro fabrication process is usually quite limited. This is due in part to the fact that a process may be in early developmental stages and sufficient data is not available to provide accurate measures of uncertainty. Intellectual property concerns can also play a significant role in limiting the amount of information available to external customers or vendors that submit designs for fabrication either for academic or commercial research. Where data is not available, conservative uncertainties may be assumed based upon expert opinion in order to justify the collection of more data and identify areas that warrant further research.

8.2.2 Investigation of Non-Idealities

Non-idealities in MEMS will continue to be an issue for design and model validation. When experimental results fail to follow expectations, investigation into the reasons for the difference between model predictions and the data could lead to the discovery of physical phenomena that may potentially be exploited in some beneficial way.

8.2.3 Model Parameterization

One of the roles of a design engineer is to develop physical models of a system in order to improve a design, customize a device for a given application, and to gain a better understanding of the system or device behavior. In order to enable the use of automated

design-stage uncertainty analysis, a model must be parametric with respect to both design variables and uncertainties in order to correctly simulate the propagation of error. However, parameterizing a model with respect to uncertainties can dramatically increase the complexity, particularly when certain assumptions can no longer be made to increase computational efficiency. Analysis software that allows custom function or relation definitions along with parametric feature geometry may help simplify the process of creating models.

8.2.4 Metamodeling

Creation of simplified models from more complex simulations can enable more rapid design of MEMS. As compliant components and elements become commonplace in a variety of MEMS, development of metamodels and design tools that can be used to quickly customize devices for specific applications may prove valuable. Development of metamodeling methods is an active area of research and one that warrants further investigation as applied to compliant mechanisms, MEMS, uncertainty analysis, and design optimization. Some specific techniques to investigate are the use of radial basis functions, kriging, nonlinear regression, and orthogonal arrays.

8.2.5 Global Model Validation

Model validation will continue to be an important aspect of research and devepment. As our ability to model more complex systems increases, particularly in fields where experimentation is expensive or not yet possible, there will be a tendency to rely more on simulation. When effects of uncertainty can be accounted for through simulation, it may be more advantageous to perform experiments covering a larger design space rather than spend most of the time and resources on obtaining repeated measurements. More

research is needed to determine proper procedures for setting up global model validation experiments, including consideration of cost and time.

8.2.6 Reliability and Yield Predictions

Making estimates of reliability and yield for MEMS through simulation is largely dependent upon the accuracy of the distributions assumed for various inputs and parameters. This requires a continual collection of parametric process data. Assuming that the data can be collected, what is the best way to archive and retrieve the data so that it can be used for model validation, uncertainty analysis, and reliability-based design?

8.2.7 Taking Advantage of Correlation

Although correlation can substantially increase the complexity of uncertainty analysis techniques, it is one of the only aspects of probabilistic design that allows input uncertainties to effectively cancel each other out. The idea of robust design has been around for many years, but this usually involves tuning design variables. Is there some way to take an inherently sensitive device that cannot be modified and add some feature or system so that the overall system is more robust? Could correlation in feature geometries be a key to accomplishing this?

8.2.8 Additional Sources of Uncertainty

The sources of uncertainty discussed in this dissertation represent only a small number of the many factors that can contribute to the reliability of MEMS. Human factors, operational variation, modeling errors, and other issues are all important to consider in designing for reliability and first-pass success. In addition, a designer must consider the

life cycle and how environmental and operational variations affect the life of the device. What is the best way to consider these errors and sources of uncertainty during design, without causing the simulation to be more expensive than testing?

8.2.9 MEMS Component Simulations

Many models can be divided into components that can be analyzed separately from the overall system. Simulations on sub-components may help improve computational efficiency, aid in design of other devices, and provide greater design intuition.

For example, in Chapter 6 the analysis of the cross-sectional properties of the thermal microactuator beams was separated from the force-displacement model. The cross-section model could be used to investigate the effects of mask alignment and edge bias on the product of inertia for layered cross-sections (which may affect the out-of-plane displacement of planar compliant mechanisms). It could also be used to determine the advantages and disadvantages of using multiple layers to mitigate the effects of edge bias variation.

8.2.10 Practical/Political Issues

Accounting for uncertainty in design is not trivial. As in tolerance analysis at the macro level, it requires collaboration between design, analysis, fabrication, and testing groups. Organizations are not always set up to encourage such interaction. Tasks are often accomplished not only by separate individuals, but also different organizations within a company. From a practical stand-point, the discussion of uncertainty and process variation is often a delicate subject. How does a designer get the information required to account for

variability without causing legal or intellectual property concerns for suppliers or foundries? What is the best way to capture, store, and retrieve uncertainty data for processes and technologies that are constantly under development?

8.2.11 Modern Computer Simulations

Parallel processing provides a means for running multiple model evaluations simultaneously, enabling the use of uncertainty quantification and optimization for computationally expensive models. As parallel computing becomes commonplace (i.e. in desktop computers or readily available via networks), there will continue to be a need for advanced uncertainty analysis approaches since the growing computational power available for simulation allows the modeling of more complex systems. However, Monte Carlo simulation will become practical for more and more engineering design problems. Particular emphasis should be placed on the development of stochastic methods and simulation tools that can be easily implemented without the need for an advanced understanding of statistics.

REFERENCES

ANSI/ASME, 1998, *Test Uncertainty*, PTC 19.1-1998, ASME, New York.

Allen, A.M., and Johnson, G.C., 2001, "Resonating Microelectromechanical Structures for Metrology," *Materials Research Society Symposium - Proceedings*, Vol. 657, pp. EE141-EE146.

Ananthasuresh, G.K., Kota, S., and Gianchandani, Y., 1994 "A Methodical Approach to the Design of Compliant Micromechanisms," *IEEE Solid-State Sensor and Actuator Workshop*, Hilton Head Island, South Carolina, pp. 189-192.

Ayyub, B.M. (editor), 1998, *Uncertainty Modeling and Analysis in Civil Engineering*, Boca Raton: CRC Press.

Ayyub, B.M., and Gupta, M.M. (editors), 1997, *Uncertainty Analysis in Engineering and Sciences: Fuzzy Logic, Statistics, and Neural Network Approach*, Boston: Kluwer Academic Publishers.

Baghdasaryan, L., Chen, W., Buranathiti, T., and Cao, J., 2002, "Model Validation via Uncertainty Propagation Using Response Surface Models," *Proceedings of the 2002 ASME Design Engineering Technical Conferences,* DETC2002/DAC-34140.

Baker, M. S., and Howell, L. L., 2002, "On-chip actuation of an in-plane compliant bistable micromechanism," *Journal of Microelectromechanical Systems*, Vol. 11, No. 5, pp. 566-573.

Baker, M.S., Lyon, S.M., and Howell, L.L., 2000, "A Linear Displacement Bistable Micromechanism," *Proceedings of the 2000 ASME Design Engineering Technical Conferences*, DETC2000/MECH-14117, pp. 1-7.

Baker, M.S., de Boer, M.P., Smith, N.F., Warne, L.K., and Sinclair, M.B., 2002, "Integrated Measurement-Modeling Approaches for Evaluating Residual Stress Using Micromachined Fixed-Fixed Beams," *Journal of Microelectromechanical Systems*, Vol. 11, No. 6, pp. 743-753.

Behi, F., Mehregany, M., and Gabriel, K.J., 1990, "A Microfabricated Three-Degree-Of-Freedom Parallel Mechanism," *Proceedings - IEEE Micro Electro Mechanical Systems: An Investigation of Micro Structures, Sensors, Actuators, Machines and Robots*, pp. 159-165.

Bisshopp, K.E., and Drucker, D.C., 1945, "Large Deflection of Cantilever Beams," *Quarterly of Applied Mathematics*, Vol. 3, No. 3, pp. 272-275.

Capanu, M., Boyd, J.G. IV, and Hesketh, P.J., 2000, "Design, Fabrication, and Testing of a Bistable Electromagnetically Actuated Microvalve," *Journal of Microelectromechanical Systems*, Vol. 9, No. 2, pp. 181-189.

Chan, E.K. and Dutton, R.W., 2000, "Electrostatic Micromechanical Actuator with Extended Range of Travel," *Journal of Microelectromechanical Systems*, Vol. 9, No. 3, pp. 321-328.

Chandrashekar, N., and Krishnamurty, S., 2002, "Bayesian Evaluation of Engineering Models," *Proceedings of the 2002 ASME Design Engineering Technical Conferences*, DETC2002/DAC-34141.

Chang, H., Tsay, J., and Sung, C., 2001, "Design of a fully compliant bistable micromechanism for switching devices," *Proceedings of SPIE - The International Society for Optical Engineering*, Vol. 4593, pp. 97-108.

Chase, K. W., Gao, J., and Magleby, S. P., 1995, "General 2-D Tolerance Analysis of Mechanical Assemblies with Small Kinematic Adjustments," *Journal of Design and Manufacturing*, Vol. 5, pp. 263-274.

Chen, J., Zou, J., Liu, C., Schutt-Ainé, J.E., and Kang, S.-M., 2003, "Design and Modeling of a Micromachined High-Q Tunable Capacitor With Large Tuning Range and a Vertical Planar Spiral Inductor," *IEEE Transactions on Electron Devices*, Vol. 50, No. 3, pp. 730-739.

Cherry, M.S., Roach, G.M., Wittwer, J.W., Howell, L.L., and Cox, J.J., 2003, "Reducing Cycle Time and Errors in the Design and Layout of MEMS," *Proceedings of the 2003 ASME Design Engineering Technical Conferences*, DETC2003/DAC-48740.

Choi, J.-H., Lee, S.J., and Choi, D.-H., 1998, "Stochastic Linkage Modeling for Mechanical Error Analysis of Planar Mechanisms," *Mechanics of Structures and Machines*, Vol. 26, No. 3, pp. 257-276.

Chu, L.L., and Gianchandani, Y.B., 2003, "A Micromachined 2D Positioner with Electrothermal Actuation and Sub-Nanometer Capacitive Sensing," *Journal of Micromechanics and Microengineering*, Vol. 13, No. 2, pp. 279-285.

Coleman, H.W., and Steele, W.G., 1999, *Experimentation and Uncertainty Analysis for Engineers*, New York: John Wiley & Sons, Inc., 2nd Ed.

Comtois, J.H., Bright, V.M., and Phipps, M.W., 1995, "Thermal microactuators for surface-micromachining processes," *Proceedings of SPIE - The International Society for Optical Engineering*, Vol. 2642, pp. 10-21.

Comtois, J.H., and Bright, V.M., 1997, "Applications for Surface-Micromachined Polysilicon Thermal Actuators and Arrays," *Sensors and actuators, A: Physical*, Vol. 48, pp. 19-25.

Contreras, H., 1980, "The Stochastic Finite-Element Method," *Computers and Structures*, Vol. 12, pp. 341-348.

Cox, N.D., 1979, "Tolerance Analysis by Computer," *Journal of Quality Technology*, Vol. 11, No. 2, pp. 80-87.

Cragun, R., and Howell, L.L., 1998, "A New Constrained Thermal Expansion Micro-Actuator," *Proceedings of the 1998 ASME International Mechanical Engineering Congress and Exposition, Micro-Electro-Mechanical Systems (MEMS),* DSC-Vol. 66, pp. 365-371.

Cragun, R., and Howell, L.L., 1999, "Linear Thermomechanical Microactuators," *Proceedings of IMECE 1999, ASME International Mechanical Engineering Congress & Exposition*, Nov, 1999, pp. 181-188.

de Boer, M.P., Redmond, J.M., and Michalske, T.A., 1998b, "A Hinged-Pad Test Structure for Sliding Friction Measurements in Micromachining," *Proceedings of SPIE - The International Society for Optical Engineering*, Vol. 3512, 1998. p. 241-250.

de Boer, M.P., Clews, P.J., Smith, B.K., and Michalski, T.A., 1998a, "Adhesion of Polysilicon Microbeams in Controlled Humidity Ambients," *Materials Research Society Symposium - Proceedings*, Vol. 518, 1998. p. 131-136.

Delauche, F., Affour, B., and Dufaza, C., 2002, "Parametric yield optimization of MEMS," *Proceedings of SPIE - The International Society for Optical Engineering*, Vol. 4755, pp. 126-135.

Doebling, S.W., Hemez, F.M., Schultze, J.F., and Cundy, A.L., 2002, "A Metamodel-Based Approach to Model Validation for Nonlinear Finite Element Simulations," *Proceedings of SPIE - The International Society for Optical Engineering*, Vol. 4753, pp. 671-678.

Eastman, F.S., 1937, "The Design of Flexure Pivots," *Journal of the Aerospace Sciences*, Vol. 5, No. 1, pp. 16-21.

Elbrecht, L., and Binder J., 1999, "Repeatability Aspects in Surface Micromachining - Investigations on Polycrystalline Silicon Films," *Journal of Micromechanics and Microengineering*, Vol. 9, No. 2, pp. 130-134.

Eldred, M.S., Giunta, A.A., Wojtkiewicz, S.F., Jr., and Trucano, T.G., 2002, "Formulations for Surrogate-Based Optimization Under Uncertainty," *Proceedings of the 9th AIAA/ISSMO Symposium on Multidisciplinary Analysis and Optimization*, Atlanta, GA, Sept. 4-6, AIAA-2002-5585.

Figliola, R.S., and Beasley, D.E., 2000, *Theory and Design For Mechanical Measurements*, 3rd Ed., New York: John Wiley & Sons, Inc.

Gandhi, M.V., and Thompson, B.S., 1981, "The Finite Element Analysis of Flexible Components of Mechanical Systems Using a Mixed Variational Principle," *ASME Design Engineering Technical Conference*, September 28-October 1, Beverly Hills, CA, pp.1-9.

Garrett, R.E. and Hall, A.S., 1969, "Effect of Tolerance and Clearance in Linkage Design," *ASME Journal of Engineering for Industry*, Vol. 91, No. 1, pp. 198-202.

Gere, J.M., and Timoshenko, S.P., 1997, *Mechanics of Materials*, 4th Ed., New York: PWS Publishing Company.

Germer, C., Hansen, H.-J., Franke, S., and Buttgenbach, S., 2002, "Tolerance analysis and synthesis in micro systems," *Proceedings of SPIE - The International Society for Optical Engineering*, Vol. 4755, pp. 355-364.

Ghanem, R.G., and Red-Horse, J., 1999, "Propagation of Probabilistic Uncertainty in Complex Physical Systems Using a Stochastic Finite Element Approach," *Physica D*, Vol. 133, pp. 137-144.

Ghanem, R.G., and Spanos, P.D., 1991, "Stochastic Finite Elements: A Spectral Approach," *Applied Mechanics Reviews*, New York: Springer-Verlag.

Gianchandani, Y.B., and Najafi, K., 1996, "Bent-Beam Strain Sensors," *Journal of Microelectromechanical Systems*, Vol. 5, No. 1, pp. 52-58.

Gill, J.J.-Y., Ngo, L.V., Nelson, P.R., and Kim, C.-J., 1998, "Elimination of Extra Spring Effect at the Step-Up Anchor of Surface-Micromachined Structure," *Journal of Microelectromechanical Systems*, Vol. 7, No. 1, pp. 114-121.

Giunta, A.A., 2002, "Use of Data Sampling, Surrogate Models, and Numerical Optimization in Engineering Design," *Proceedings of the 40th AIAA Aerospace Sciences Meeting and Exhibit*, Reno, NV, Jan., AIAA-2002-0538.

Giunta, A.A., Wojtkiewicz, S.F., Jr., and Eldred, M.A., 2003, "Overview of Modern Design of Experiments Methods for Computation Simulations," *Proceedings of the 41st AIAA Aerospace Sciences Meeting and Exhibit*, Reno, NV, Jan. 6-9, AIAA-2003-0649.

Glancy, C.G., Chase, K.W., 1999, "A Second-Order Method for Assembly Tolerance Analysis," *Proceedings of the 1999 ASME Design Engineering Technical Conferences*, DETC99/DAC-8707.

Goll, C., Bacher, W., Bstgens, B., Maas, D.,Menz W., and Schomburg, W.K., 1996, "Microvalves with bistable buckled polymer diaphragms," *Journal of Micromechanics and Microengineering*, Vol. 6, No. 1, pp. 77-79.

Gomm, T., Howell, L.L., and Selfridge, R.H., 2002, "In-plane linear-displacement bistable microrelay," *Journal of Micromechanics and Microengineering*, Vol. 12, No. 3, pp. 257-264.

Gorski, W., 1976, "A Review of Literature and a Bibliography on Finite Elastic Deflections of Bars," *Transactions of the Institution of Engineers, Australia, Civil Engineering Transactions*, Vol. 18, No.2, pp. 74-85.

Gupta, R.K., 2000, "Electronically Probed Measurements of MEMS Geometries," *Journal of Microelectromechanical Systems*, Vol. 9, No. 3, pp. 380-389.

Haldar, A., and Mahadevan, S., 2000a, *Probability, Reliability and Statistical Methods in Engineering Design*, New York: John Wiley & Sons, Inc.

Haldar, A., and Mahadevan, S., 2000b, *Reliability Assessment Using Stochastic Finite Element Analysis*, New York: John Wiley & Sons, Inc.

Hälg, B., 1990, "On a Nonvolatile Memory Cell Based on Micro-Electro-Mechanics," *Proceedings - IEEE Micro Electro Mechanical Systems: An Investigation of Micro Structures, Sensors, Actuators, Machines and Robots*, Feb 11-14 1990, Napa Valley, CA, pp. 172-176.

Han, J.S., and Kwak, B.M., 2001, "Robust Optimal Design of a Vibratory Microgyroscope Considering Fabrication Errors," *Journal of Micromechanics and Microengineering*, Vol. 11, No. 6, pp. 662-671.

Han, J.S., and Kwak, B.M., 2004, "Robust Optimization Using a Gradient Index: MEMS Applications," *Structural and Multidisciplinary Optimization*, Vol. 27, pp. 469-478.

Hartenberg, R.S., and Denavit, J., 1964, *Kinematic Synthesis of Linkages*, McGraw-Hill.

Hetherington, D.L., and Sniegowski, J.J., 1998, "Improved Polysilicon Surface-Micromachined Micromirror Devices Using Chemical-Mechanical Polishing," *Proceedings of SPIE - The International Society for Optical Engineering*, Vol. 3440, pp. 148-153.

Hills, R.G., and Trucano, T.G., 1999, "Statistical Validation of Engineering and Scientific Models: Background," *Sandia National Laboratories*, Sandia Report, SAND99-1256.

Hoffmann, M., Kopka, P., and Voges, E., 1999a, "Bistable Micromechanical Fiber-Optic Switches on Silicon With Thermal Actuators," *Sensors and Actuators, A: Physical*, No. 78, pp. 28-35.

Hoffmann, M., Kopka, P., Gross, T., and Voges, E., 1999b, "Optical fibre switches based on full wafer silicon micromachining," *Journal of Micromechanics and Microengineering*, Vol. 9, n.2, June 1999. p. 151-155.

Hong, Y. S., and Chang, T.-C., 2002, "A Comprehensive Review of Tolerancing Research," *International Journal of Production Research*, Vol. 40, No. 11, pp. 2425-2459.

Huang, Q.-A., and Lee, N.K.S., 2000, "A simple approach to characterizing the driving force of polysilicon laterally driven thermal microactuator," *Sensors and Actuators*, Vol. 80, pp. 267-272.

Howell, L.L., 2001, *Compliant Mechanisms*, John Wiley & Sons, Inc., New York.

Howell, L. L., Rao, S. S., and Midha, A., 1994, "Reliability-Based Optimal Design of a Bistable Compliant Mechanism," *Journal of Mechanical Design*, Vol. 116, No. 1, pp. 1115-1121.

Howell, L.L., and Midha, A., and Murphy, M.D., 1994d, "Dimensional Synthesis of Compliant Constant-Force Slider Mechanisms," *American Society of Mechanical Engineers, Design Engineering Division (Publication) DE*, DE-Vol. 71, 23rd Biennial Mechanisms Conference, pp. 509-515.

Iman, R.L., and Helton, J.C., 1984, "A Comparison of Uncertainty and Sensitivity Analysis Techniques for Computer Models," *Sandia National Laboratories*, Sandia Report, SAND84-1461.

Internatational Organization for Standardization, *Guide to the Expression of Uncertainty in Measurement*, ISO, Geneva, 1993.

Jaecklin, V.P., Linder, C., De Rooji, N.F., and Moret, J.-M., 1993, "Comb Actuators for XY-Microstages," *Sensors and Actuators, A: Physical*, Vol. 39, No. 1, pp. 83-89.

Jang, W.I., Choi, C.A., Lee, M.L., Jun, C.H., and Kim, Y.T., 1996, "Fabrication of MEMS devices by using anhydrous HF gas-phase etching with alcoholic vapor," *Journal of Micromechanics and Microengineering*, Vol. 12, No. 3, pp. 297-306.

Jensen, B.D., Bitsie, F., and de Boer, M., 1999a, "Interferometric Measurement for Improved Understanding of Boundary Effects in Micromachined Beams," *Proceedings of SPIE - The International Society for Optical Engineering*, Vol. 3875, 1999. pp. 61-72.

Jensen, B.D., de Boer, M.P., Masters, N.D., Bitsie, F., and LaVan, D.A., 2001a, "Interferometry of Actuated Microcantilevers to Determine Material Properties and Test Structure Nonidealities in MEMS," *Journal of Microelectromechanical Systems*, Vol. 10, No. 3, Sept. 2001. pp. 336-346.

Jensen, B.D., Howell, L.L., and Salmon, L.G., 1998, "Introduction of Two-Link In-Plane, Bistable Compliant MEMS," *Proceeding of the 1998 ASME Design Engineering Technical Conferences*, DETC98/MECH-5837.

Jensen, B.D., Howell, L.L., and Salmon, L.G., 1999b, "Design of Two-Link In-Plane, Bistable Compliant Micro-Mechanisms," *Journal of Mechanical Design*, Vol. 121, pp. 416-423.

Jensen, B.D., Parkinson, M.B., Kurabayashi, K., Howell, L.L., and Baker, M.S., 2001b, "Design Optimization of a Fully-Compliant Bistable Micro-Mechanism," *Proceedings of IMECE 2001, ASME International Mechanical Engineering Congress & Exposition*, Nov. 11-16, 2001, New York, New York.

Jin, R., Chen, W., and Simpson, T., 2001, "Comparative Studies of Metamodeling Techniques Under Multiple Modeling Criteria," *Structural and Multidisciplinary Optimization*, Vol. 23, pp. 1-13.

Jin, R., Du, X., and Chen, W., 2003, "The Use of Metamodeling Techniques for Optimization Under Uncertainty," *Structural and Multidisciplinary Optimization*, Vol. 25, pp. 99-116.

Johnson, G.C., Jones, P.T., and Howe, R.T., 1999, "Materials Characterization for MEMS - A Comparison of Uniaxial and Bending Tests," *Proceedings of SPIE - The International Society for Optical Engineering*, Vol. 3874, pp. 94-101.

Jones, R.V., 1951, "Parallel and Rectilinear Spring Movements," *Journal of Physics E: Scientific Instruments*, Vol. 28, pp. 38-41.

Jones, R.V., and Young, I.R., 1956, "Some Parasitic Deflections in Parallel Spring Movements," *Journal of Physics E: Scientific Instruments*, Vol. 33, , pp. 11-15.

Jonsmann, J., Sigmund, O., and Bouwstra, S., 1999, "Compliant Electro-Thermal Microactuators," *Proceedings of the IEEE Micro Electro Mechanical Systems (MEMS)*, pp. 588-593.

Juvinall, R.C., 1967, *Stress, Strain, and Strength*, New York: McGraw-Hill, Inc.

Kam, T.Y., and Lin, S.C., 1990, "A Procedure for Probabilistic Analysis of Nonlinear Structures," *Computers and Structures*, Vol. 36, No. 4, pp. 647-652.

Kemeny, D.C., Howell, L.L., and Magleby, S.P., 2002, "Using Compliant Mechanisms to Improve Manufacturability in MEMS," *Proceedings of the 2002 ASME Design Engineering Technical Conferences*, DETC2002/DFM-34178.

Kim, C., and Kota, S., 2002, "Design of a Novel Compliant Transmission for Secondary Microactuators in Disk Drives," *Proceedings of the 2002 ASME Design Engineering Technical Conferences*, DETC2002/MECH-34208.

Kleiber, M., 1980, "An Error Estimation Method in Finite Element Structural Analysis," *Computers and Structures*, Vol. 11, pp. 343-347.

Kobrinsky, M.J., Deutsch, E.R., and Senturia, S.D., 2000, "Effect of Support Compliance and Residual Stress on the Shape of Doubly Supported Surface-Micromachined Beams," *Journal of Microelectromechanical Systems*, Vol. 9, No. 3, pp. 361-369.

Koester, D.A., Mahadevan, R., Hardy, B., and Markus, K.W., 2001, *MUMPs® Design Handbook* revision 7.0 (Research Triangle Park, NC: Cronos Integrated Microsystems).

Kosuge, K., Fukuda, T., and Mehregany, M., 1991, "Kinematic Analysis of Precision Planar Manipulator on Silicon," *Transducers '91 International Conference on Solid-State Sensors and Actuators*, pp. 618-621.

Kota, S., Joo, J., Li, Z., Rodgers, S.M., and Sniegowshi, J., 2001, "Design of Compliant Mechanisms: Application to MEMS," *Analog Integrated Circuits and Signal Processing-An International Journal*, Vol. 29, pp. 7-15.

Kruglick, E.J.J., and Pister, K.S.J., 1998, "Bistable MEMS Relays and Contact Characterization," *IEEE Solid-State Sensor and Actuator Workshop*, Hilton Head Island, South Carolina, June 8-11, pp. 333-337.

Kuo, W., Prasad, V.R., Tillman, F.A., Hawang C.-L., 2001, *Optimal Reliability Design*, Cambridge University Press.

Lai, Y., McDonald, J., Kujath, M., and Hubbard, T., 2004, "Force, deflection and power measurements of toggled microthermal actuators," *Journal of Micromechanics and Microengineering*, Vol. 14, pp. 49-56.

Larsen, D.V., 1989, "An Efficient Method for Iterative Tolerance Design Using Monte Carlo Simulation," M.S. Thesis, Brigham Young University, Provo, Utah.

Legtenberg, R., Groeneveld, A.W., and Elwenspoek, M., 1996, "Comb-drive actuators for large displacements," *Journal of Micromechanics and Microengineering*, Vol. 6, No. 3, pp. 320-329.

Lerch, P., Slimane, C.K., Romanowicz, B., and Renaud, P., 1996, "Modelization and characterization of asymmetrical thermal micro-actuators," *Journal of Micromechanics and Microengineering*, Vol 6, pp. 134-137.

Lews, L.K., 1993, "A Second Order, Non-Normal Statistical Tolerance Model for Robust Optimal Design," *M.S. Thesis*, Brigham Young University, Provo, Utah.

Li, J., and Ananthasuresh, G.K., 2001, "A Quality Study on the Excimer Laser Micromachining of Electro-Thermal-Compliant Micro Devices," *Journal of Micromechanics and Microengineering*, Vol. 11, pp. 38-47.

Liebmann, L.W., Molless, A.F., Ferguson, R.A., Wong, A.K., and Mansfield, S.M., 1997, "Understanding across chip line width variation: the first step toward optical proximity correction," *Proceedings of SPIE - The International Society for Optical Engineering*, Vol. 3051, pp. 124-136.

Lim, M.G., Chang, J.C., Schultz, D.P., Howe, R.T., and White, R.M., 1990, "Polysilicon Microstructures to Characterize Static Friction," *Proceeding of the IEEE Workshop on MEMS*, pp. 82-88.

Limary, S., Stewart, H.D., Irwin, L.W., McBrayer, J., Sniegowski, J.J., Montague, S., Smith, J.H., de Boer, M.P., and Jakubczak, J.F., 1999, "Reproducibility data on SUMMiT," *Proceedings of SPIE - The International Society for Optical Engineering*, Vol. 3874, pp. 102-112.

Liu, R., Paden, B., and Turner, K., 2002, "MEMS Resonators That Are Robust to Process-Induced Feature Width Variations," *Journal of Microelectromechanical Systems*, Vol. 11, No. 5, pp. 505-51.

Lobontiu, N., 2003, *Compliant Mechanisms: Design of Flexure Hinges*, New York: CRC Press.

Lott, C.D., Harb, J.N., McLain, T.W., and Howell, L.L., 2001, "Dynamic Modeling of a Surface-micromachined Linear Thermomechanical Actuator," *Technical Proceedings of the Fourth International Conference on Modeling and Simulation of Microsystems*, MSM 2001, Hilton Head Island, South Carolina, March 2001, pp. 374-377.

Ma, A., Chen, S., and Han, W., 1996, "Statistical Properties of Response for Nonlinear Structural Systems with Random Parameters," *Computers and Structures*, Vol. 58, No. 6, pp. 1139-1144.

Mali, R.K., Bifano, T., Koester, D., 1999, "A Design-based Approach to Planarization in Multilayer Surface Micromachining," *Journal of Micromechanics and Microengineering*, Vol. 9, No. 4, pp. 294-299.

Maloney, J.M., Schreiber, D.S., and DeVoe, D.L., 2004, "Large-Force Electrothermal Linear Micromotors," *Journal of Micromechanics and Microengineering*, Vol. 14, pp. 226-234.

Masters, N. D., de Boer, M. P., Jensen, B. D., Baker, M. S., and Koester, D., 2001, "Side-by-Side Comparison of Passive MEMS Residual Strain Test Structures under Residual Compression," *Mechanical Properties of Structural Films, ASTM STP 1413*, C. L. Muhlstein and S. B. Brown, Eds., American Society for Testing and

Materials, West Conshohocken, PA, Online, Available: www.astm.org/STP/1413/1413_23.

Masters, N.D., and Howell, L.L., 2002, "A Three Degree of Freedom Pseudo-Rigid-Body Model for the Design of a Fully Compliant Bistable Micromechanism," *Proceedings of the 2002 ASME Design Engineering Technical Conferences*, DETC2002/MECH-34202.

Matusz, J.M., O'Donnell, W.J., and Erdlac, R.J., 1969, "Local Flexibility Coefficients for the Built-In Ends of Beams and Plates," *Journal of Engineering for Industry*, Vol. 91, No. 3, pp. 607-614.

Maute, K., and Frangopol, D.M., 2003, "Reliability-based design of MEMS mechanisms by topology optimization," *Computers and Structures*, Vol. 81, pp. 813-824.

Mawardi, A., and Pitchumani, R., 2004, "Design of Microresonators Under Uncertainty," *Journal of Microelectromechanical Systems*, Vol. 14, No. 1, pp. 63-69.

Meng, Q., Mehregany, M., and Mullen, R.L., 1993, "Theoretical Modeling of Microfabricated Beams with Elastically Restrained Supports," *Journal of Microelectromechanical Systems*, Vol. 2, No. 3, pp. 128-137.

Mirfendereski, D., Lin, L., Kiureghian, A.D., and Pisano, A.P., 1993, "Probabilistic Response of Micro-Fabricated Polysilicon Beam Structures: Comparison of Analysis and Experiments," *ASME, Dynamic Systems and Control Division*, Vol. 46, pp. 77-80.

Montgomery, D.C., and Evans, D.M., 1975, "Second-Order Response Surface Designs in Computer Simulation," *Simulation*, Vol. 29, No. 6, pp. 169-178.

Morris, M.D., 2000, "Class of Three-Level Experimental Designs for Response Surface Modeling," *Technometrics*, Vol. 42, No. 2, pp. 111-121.

Muchow, J., Kretschmann, A., Henn, R., Skrobanek, K., Finkbeiner, S., and Krauss, H.R., 2002, "Influence of process variation on the functionality of a high pressure sensor," *Proceedings of SPIE - The International Society for Optical Engineering*, Vol. 4755, pp. 143-148.

Myers, R.H., Khuri, A.I., and Carter, W.H., 1989, "Response Surface Methodology: 1966-1988," *Technometrics*, Vol. 21, No. 2, pp. 137-157.

Myers, R.H., and Montgomery, D.C., 1995, *Response Surface Methodology: Process and Product Optimization Using Designed Experiments*, New York: John Wiley & Sons, Inc.

Nikolaidis, E., Chen, S., Cudney, H., Haftka, R.T., and Rosca, R., 2004, "Comparison of Probability and Possibility for Design Against Catastrophic Failure Under Uncertainty," *Journal of Mechanical Design*, Vol. 126, pp. 386-394.

Nguyen, H.D., Hah, D., Patterson, P.R., Chao, R., Piyawattanametha, W., Lau, E.K., and Wu, M.C., 2004, "Angular Vertical Comb-Driven Tunable Capacitor With High-Tuning Capabilities," *Journal of Microelectromechanical Systems*, Vol. 13, No. 3, pp. 406-413.

O'Donnell, W. J., 1963, "Stresses and Deflections in Built-In Beams," *Journal of Engineering for Industry*, Vol. 85, No. 3, pp. 265-273.

O'Donnell, W. J., 1960, "The Additional Deflection of a Cantilever Due to the Elasticity of the Support," *Journal of Applied Mechanics*, Vol. 27, No. 3, pp. 461-464, Trans. ASME, Series E, Vol. 82.

Opdahl, P., Jensen, B.D., and Howell, L.L., 1998, "An Investigation into Compliant Bistable Mechanisms," *Proceedings of the 1998 ASME Design Engineering Technical Conferences*, DETC09/DAC-3763.

Park, J.-S., Chu, L. L., Oliver, A. D., and Gianchandani, Y.B., 2001, "Bent-beam electrothermal actuators—Part II: Linear and rotary microengines," *Journal of Microelectromechanical Systems*, Vol. 10, No. 2, pp. 255-262.

Park, J.-S., Chu, L.L., Siwapornsathain, E., Oliver, A.D., and Gianchandani, Y.B., 2000, "Long Throw and Rotary Output Electro-Thermal Actuators Based on Bent-Beam Suspensions," *Proceedings of the IEEE Micro Electro Mechanical Systems (MEMS)*, pp. 680-685.

Parkinson, A.R., Sorensen, C., and Pourhassan, N., 1993, "A General Approach for Robust Optimal Design," *Journal of Mechanism Design: Transactions of the ASME*, Vol. 115, No. 1, pp. 74-80.

Parkinson, M.B., Jensen, B.D., and Roach, G.M., 2000, "Optimization-Based Design of a Fully-Compliant Bistable Micromechanism," *2000 ASME Design Engineering Techical Conferences and Computer and Information in Engineering Conference*, Sept. 10-13, 2000, Baltimore, Maryland.

Peroulis, D., Pacheco, S.P., Sarabandi, K., and Katehi, L.P.B., 2003, "Electromechanical Considerations in Developing Low-Voltage RF MEMS Switches," *IEEE Transactions on Microwave Theory and Techniques*, Vol. 51, No. 1, pp. 259-270.

Pilkey, W.D., 1997, *Peterson's Stress Concentration Factors*, New York: John Wiley & Sons, Inc.

Pryputniewicz, R.J., Furlong, C., and Pryputniewicz, E.J., 2002, "Design by Analysis of a MEMS Pressure Sensor," *Proceedings of SPIE - The International Society for Optical Engineering*, Vol. 4931, pp. 81-86.

Qiu, J., Lang, J.H., and Slocum, A.H., 2001, "A Centrally-Clamped Parallel-Beam Bistable MEMS Mechanism," *Proceedings of the IEEE Micro Electro Mechanical Systems (MEMS)*, pp. 353-356.

Qiu, J., Lang, J.H., and Slocum, A.H., 2004, "A Curved-Beam Bistable Mechanism," *Journal of Microelectromechanical Systems*, Vol. 13, No. 2, pp. 137-146.

Que, L., Otradovec, L., Oliver, A.D., and Gianchandani, Y.B., 2001, "Pulse and DC Operation Lifetimes of Bent-Beam ElectroThermal Actuators," *Proceedings of the IEEE Micro Electro Mechanical Systems (MEMS)*, pp. 570-573.

Que, L., Park, J.-S., and Gianchandani, Y.B., 1999, "Bent-Beam Electro-Thermal Actuators for High Force Applications," *Proceedings of the IEEE Micro Electro Mechanical Systems (MEMS)*, pp. 31-36.

Rao, S. S., 1992, *Reliability-Based Design*, New York: McGraw-Hill, Inc.

Reid, J.R., Bright, V.M., and Comtois, J.H., 1996, "Force Measurements of Polysilicon Thermal Micro-Actuators," *Proceedings of SPIE - The International Society for Optical Engineering*, Vol. 2882, pp 296-306.

Rencher, A.C., 1995, *Methods of Multivariate Analysis*, New York: John Wiley & Sons, Inc.

Rosing, R., Lechner, A., Richardson, A., and Dorey, A., 2000, "Fault Simulation and Modelling of Microelectromechanical Systems," *Computing and Control Engineering Journal*, Vol. 11, No. 5, pp. 242-250.

Ruan, A., Tse, M.S., Chong, G.Y., 2001a, "Simulation and optimization of a micromachined gyroscope using high-aspect-ratio micromachining fabrication process," *Proceedings of SPIE - The International Society for Optical Engineering*, Vol. 4593, pp. 176-185.

Ryu, J.W., and Gweon, D.-G., 1997, "Error Analysis of a Flexure Hinge Mechanism Induced by Machining Imperfection," *Precision Engineering*, Vol. 21, No. 2-3, pp. 83-89.

Sacks, E., and Allen, J., 1998, "Computer-Aided Micro-Mechanism Design," *Proceedings of the 1998 ASME IMECE, Micro-Electro-Mechanical Systems (MEMS)*, DSC-Vol. 66, pp. 313-316.

Sadler, D.J., Liakopoulos, T.M., and Ahn, C.H., 2000, "A Universal Electromagnetic Microactuator Using Magnetic Interconnection Concepts," *Journal of Microelectromechanical Systems*, Vol. 9, No. 4, pp. 460-468.

Saif, M., 2000, "On a Tunable Bistable MEMS -- Theory and Experiment," *Journal of Microelectromechanical Systems*, Vol. 9, n2, 2000. p. 157-170.

Saltelli, A., Chan, K., and Scott, E.M., 2000, *Sensitivity Analysis*, New York: John Wiley & Sons, Inc.

Sandia MEMS Advanced Design Short Course, 2004, *Reproducibility Data on SUMMiT V™*.

Schenato, L., Wu, W.-C., Ghaoui, L.E., and Pister, K., 2001, "Process Variation Analysis for MEMS Design," *Proceedings of SPIE - The International Society for Optical Engineering*, Vol. 4236, pp. 272-279.

Sevak, N.M., and McLarnan, C.W., 1974, "Optimal Synthesis of Flexible Link Mechanisms with Large Static Deflections," ASME Paper No. 74-DET-83.

Shapiro, S.S., and Gross, A.J., 1981, *Statistical Modeling Techniques*, New York: Marcel Dekker, Inc.

Sharpe, W.N., Brown, S., Johnson, G.C., and Knauss, W., 1998, "Round-Robin Tests of Modulus and Strength of Polysilicon," *Material Research Society Symposium Proceedings*, Vol. 518, pp. 57-65.

Sharpe, W.N., Jackson, K.M., Hemker, K.J., and Xie, Z., 2001, "Effect of Specimen Size on Young's Modulus and Fracture Strength of Polysilicon," *Journal of Microelectromechanical Systems*, Vol. 10, No. 3, pp. 317-326.

Sharpe, W.N., Turner, K.T., and Edwards, R.L., 1999, "Tensile Testing of Polysilicon," *Experimental Mechanics*, Vol. 39, No. 3, pp. 162-170.

Simpson, T.W., Peplinkski, J., Koch, P.N., and Allen, J.K., 1997, "On the Use of Statistics in Design and the Implications for Deterministic Computer Experiments," *Proceeding of the 1997 ASME Design Engineering Technical Conferences, Design Theory and Methodology*, Sacramento, CA, Paper DETC97/DTM-3881.

Sinclair, M.J., 2000, "A High Force Low Area MEMS Thermal Actuator," *Thermomechanical Phenomena in Electronic Systems -Proceedings of the Intersociety Conference*, pp. 127-132.

Sinclair, M.J. and Wang, K., 2003, "Thermal Actuator Improvements: Tapering and Folding," *Proceedings of SPIE - The International Society for Optical Engineering*, Vol. 5116, pp. 237-251.

Small, N.C., 1961, "Bending of a Cantilever Plate Supported From an Elastic Half Space," *Journal of Applied Mechanics*, Vol. 28, pp. 387-394, Trans. ASME, Vol. 83.

Smith, N.F., Eaton, W.P., Tanner, D.M., and Allen, J.J., 1999, "Development of Characterization Tools for Reliability Testing of MicroElectroMechanical System Actuators," *Proceedings of SPIE - The International Society for Optical Engineering*, Vol. 3880, 1999. p. 156-164.

Smith, S.T., 2000, *Flexures: Elements of Elastic Mechanisms*, Gordon and Breach Science Publishers.

Smith, S.T., and Chetwynd, D.G., 1992, *Foundations of Ultraprecision Mechanism Design*, Gordon and Breach Science Publishers.

Sniegowski, J.J., and Rodgers, M.S., 1997, "Multi-Layer Enhancement to Polysilicon Surface-Micromachining Technology," *Technical Digest - International Electron Devices Meeting*, pp. 903-906.

Sniegowski, J.J., and de Boer, M.P., 2000, "IC-compatible polysilicon surface micromachining," *Annu. Rev. Mater. Sci.*, Vol. 30, pp. 299-333.

Stamatis, D.H., 1995, *Failure Mode and Effect Analysis: FMEA from Theory to Execution*, Milwaukee; ASQC Quality Press.

Taguchi, G., Elsaed, E., and Hsiang, T., 1989, *Quality Engineering in Production Systems*, McGraw-Hill.

Tanner, D.M., et al., 2000a, "MEMS Reliability: Infrastructure, Test Structures, Experiments, and Failure Modes," Sandia National Laboratories, Sandia Report SAND2000-0091.

Tanner, D.M., Owen, A.C., Jr., and Rodriguez, F., 2003, "Resonant Frequency Method for Monitoring MEMS Fabrication," *Proceedings of SPIE - The International Society for Optical Engineering*, Vol. 4980, pp. 220-228.

Vangbo, M., 1998, "An Analytical Analysis of a Compressed Bistable Buckled Beam," *Sensors and Actuators A*, Vol. 69, No. 3, pp. 212-216.

Vardeman, S.B., 1994, *Statistics for Engineering Problem Solving*, Boston: PWS Publishing Company.

Wadsworth, H.M., 1990, *Handbook of Statistical Methods for Engineers and Scientists*, New York: McGraw-Hill.

Wagner,B., Quenzer,H.J., Hoerschelmann,S., Lisec,T., and Juerss, M., 1996, "Bistable Microvalve with Pneumatically Coupled Membranes," *Proceedings of the IEEE Micro Electro Mechanical Systems (MEMS)*, Feb 11-15 1996, San Diego, CA, pp. 384-388.

Wang, N., and Ge, P., 1999, "Study of Metamodeling Techniques and Their Applications in Engineering Design," *Manufacturing Science and Engineering*, MED-Vol. 10, pp. 89-95.

Welch, W.J., Buck, R.J., Sacks, J., Wynn, H.P., Mitchell, T.J., and Morris, M.D., 1992, "Screening, Predicting, and Computer Experiments," *Technometrics*, Vol. 34, No. 1, pp. 15-25.

Wittwer, Jonathan W., 2001, "Predicting the Effects of Dimensional and Material Property Variations in Micro Compliant Mechanisms," *M.S. Thesis*, Brigham Young University, Provo, Utah.

Wittwer, J.W., Howell, L.L., Chase, K.W., 2001, "Modeling the Effects of Joint Clearances in Planar Micromechanisms," *Technical Proceedings of the Fourth International Conference on Modeling and Simulation of Microsystems, MSM 2001*, Hilton Head Island, SC, March 2001, pp. 374-377.

Wittwer, J.W., Chase, K.W., and Howell, L.L., 2004, "The Direct Linearization Method Applied to Position Error in Kinematic Linkages," *Mechanism and Machine Theory*, Vol. 39, No. 7, pp. 681-693.

Wittwer, J.W., and Howell, L.L., 2002, "Design of a Functionally Binary Pinned-Pinned Segment For Use as a Tension-Compression Spring in Compliant Mechanisms," *Proceedings of IMECE 2002, ASME International Mechanical Engineering Congress & Exposition*, Nov. 17-22, 2002, New Orleans, Louisiana, IMECE2002-33982.

Wittwer, J.W., and Howell, L.L., 2004, "Mitigating the Effects of Local Elasticity at the Built-In Ends of Beams and Flexures," *Journal of Applied Mechanics*, Vol. 71, No. 5, pp. 748-751.

Wittwer, J.W., Howell, L.L., Wait, S.M., Cherry, M.S., 2002b, "Predicting the Performance of a Bistable Micro Mechanism Using Design-Stage Uncertainty Analysis," *Proceedings of IMECE 2002, ASME International Mechanical Engineering Congress & Exposition*, Nov. 17-22, 2002, New Orleans, Louisiana, IMECE2002-33262.

Wittwer, J.W., Gomm, T., and Howell, L.L., 2002a, "Surface Micromachined Force Gauges: Uncertainty and Reliability," *Journal of Micromechanics and Microengineering*, Vol. 12, pp. 13-20.

Wojtkiewicz, S.F., Jr., Eldred, M.S., Field, R.V., Jr., Urbina, A., and Red-Horse, J.R., 2001, "Uncertainty Quantification In Large Computational Engineering Models," *Proceedings of the 42nd AIAA/ASME/ASCE/AHS/ASC Structures, Structural Dynamics, and Materials Conference*, Seattle, WA, April 16-19, AIAA-2001-1455.

Xiao, Z., Peng, W., Wolffenbuttel, R.F., and Famer, K.R., 2002, "Micromachined Variable Capacitor with Wide Tuning Range," *Solid-State Sensor, Actuator and Microsystems Workshop*, Hilton Head Island, South Carolina, June 2-6, pp. 346-349.

Yang, Y.-J., and Kim, C.-J., 1995a, "Dynamics of a Bistable Snapping Microactuator," *Proceedings of SPIE*, Vol. 2443, pp. 754-762.

Yang, Y.-J., and Kim, C.-J., 1995b, "Testing and Characterization of a Bistable Snapping Microactuator Based on Thermo-Mechanical Analysis," *Digest of Technical Papers / International Conference on Solid-State Sensors and Actuators*, Vol. 2, pp. 337-340.

Yin, L., and Ananthasuresh, G.K., 2002, "A Novel Topology Design Scheme for the Multi-Physics Problems of Electro-Thermally Actuated Compliant Micromechanisms," *Sensors and Actuators, A: Physical*, Vol. 97-98, pp. 599-609.

Young, W.C., 1989, *Roark's Formulas for Stress and Strain*, 6th Ed., London: McGraw-Hill.

Zhou, G., Low, D., and Dowd, P., 2001, "Method to Achieve Large Displacements Using Comb Drive Actuators," *Proceedings of SPIE - The International Society for Optical Engineering*, Vol. 4557, pp. 428-435.

APPENDIX

APPENDIX A MATLAB CODE

A.1 hist2d.m - 2D Histogram Function

The following code is a self-documented MATLAB m-file used to create a 2D histrogram with various shading and graphics options. It requires the use of the optionget function in Appendix A.2.

```
function freq2d = hist2d (XY, Xbins, Ybins, options)
%---------------------------------------------------------------------
% hist2d.m - 2 Dimensional Histogram
%
% USAGE:
%  freq2d = hist2d ([X, Y], Xbins, Ybins, options)
%       Counts number of points in the bins defined by vYEdge, vXEdge.
%       size(freq2d) == [length(Ybins)-1, length(Xbins)-1]
%
%  freq2d = hist2d ([X, Y])     % Use default Xbins, Ybins, options
%  freq2d = hist2d ([X, Y], options)    % Use default Xbins, Ybins
%  freq2d = hist2d ([X, Y], Xbins, Ybins)   % Use default options
%
% INPUT:
%   XY = [X, Y] = n x 2 Matrix consisting of two n x 1 vectors
%   Xbins = Vector defining X bins
%   Ybins = Vector defining Y bins
%   options = graphing options (see below)
%
% OUTPUT:
%   freq2d = 2d frequency matrix
%
% OPTIONS:
%   .graph = [0=false] Create a 2D histogram graph
%            Otherwise, just return the freq2d matrix
%   .type = ['surf']
%            Use 'pcolor' or 'surf' 3D plot
%   .shade = [1=true] use: shading interp
%       .colormap = ['ibone'] colormap to use for shading
%          Choices: 'bone','ibone','gray'
%       .colorbar = [1=true] add a colorbar
%
% EXAMPLE
%   XY = randn(10000,2);
```

```
%   Xbins = linspace(-3,3,40)';
%   Ybins = linspace(-3,3,50)';
%   freq2d = hist2d(XY,Xbins,Ybins);
%
%   nXBins = length(Xbins);
%   nYBins = length(Ybins);
%   xLab = 0.5*(Xbins(1:(nXBins-1))+Xbins(2:nXBins));
%   yLab = 0.5*(Ybins(1:(nYBins-1))+Ybins(2:nYBins));
%   pcolor(xLab, yLab, freq2d); shading interp; colorbar;
%   surf(xLab, yLab, freq2d); shading interp; colorbar;
%   colormap(gray);  %See: help graph3d
%
% (c) 2004, 2005 Jon Wittwer
%-------------------------------------------------------------

% The following default options will be used if not set
defaultopt = struct( ...
    'graph',0,...
    'type','surf',...
    'shade',1,...
    'colormap','pcolor',...
    'colorbar',1);

if nargin == 1 | nargin == 3
    options = defaultopt;
end
if nargin == 2
    options = Xbins
end

[points,cols] = size(XY);
if cols ~= 2
    error ('XY must have at least two columns');
end

Y = XY(:,2);    %Row
X = XY(:,1);    %Col

if nargin < 3
   % Set default number of bins based upon the number of points.
   % Max 50 bins
   Xbins = linspace(min(X),max(X),min(ceil(points/10),50))';
   Ybins = linspace(min(Y),max(Y),min(ceil(points/10),50))';
end

nRow = length(Ybins)-1;
nCol = length(Xbins)-1;

freq2d = zeros(nRow,nCol);

for iRow = 1:nRow
    rRowLB = Ybins(iRow);
    rRowUB = Ybins(iRow+1);

    [mIdxRow] = find (Y > rRowLB & Y <= rRowUB);
    XFound = X(mIdxRow);

    if (~isempty(XFound))
        vFound = histc (XFound, Xbins);
```

```
        nFound = (length(vFound)-1);

        if (nFound ~= nCol)
            [nFound nCol]
            error ('hist2d error: Size Error')
        end

        [nRowFound, nColFound] = size (vFound);

        nRowFound = nRowFound - 1;
        nColFound = nColFound - 1;

        if nRowFound == nCol
            freq2d(iRow, :)= vFound(1:nFound)';
        elseif nColFound == nCol
            freq2d(iRow, :)= vFound(1:nFound);
        else
            error ('hist2d error: Size Error')
        end
    end
end

if optionget(options,'graph',defaultopt)
    nXBins = length(Xbins);
    nYBins = length(Ybins);
    xLab = 0.5*(Xbins(1:(nXBins-1))+Xbins(2:nXBins));
    yLab = 0.5*(Ybins(1:(nYBins-1))+Ybins(2:nYBins));

    switch optionget(options,'type',defaultopt);
    case 'pcolor'
        pcolor(xLab, yLab, freq2d);
    case 'surf'
        surf(xLab, yLab, freq2d);
        view(0,90);
    otherwise
        error(sprintf('"%s" graph type not recognized',...
            optionget(options,'type',defaultopt)));
    end

    if optionget(options,'shade',defaultopt)
        shading interp;
        switch optionget(options,'colormap',defaultopt)
        case 'bone'
            colormap(bone);
        case 'ibone'
            z = linspace(length(bone),1,length(bone))';
            ibone = [z, bone];
            ibone = sortrows(ibone,1);
            ibone = ibone(:,2:4);
            colormap(ibone);
        case 'gray'
            colormap(gray);
        case 'igray'
            z = linspace(length(gray),1,length(gray))';
            ibone = [z, gray];
            ibone = sortrows(ibone,1);
            ibone = ibone(:,2:4);
            colormap(ibone);
        end
```

```
    end
    if optionget(options,'colorbar',defaultopt)
        colorbar;
    end
end
```

A.2 optionget.m - Get values from structures

```
function value = optionget(options,name,default)
%-----------------------------------------------------------------
%optionget.m  -  Get parameters from an options-type structure.
%
% USAGE:
%   value = optionget(OPTIONS,'name')
%   value = optionget(OPTIONS,'name',DEFAULT)
%
%   Returns the value of the structure field 'name' from the
%   OPTIONS structure. If OPTIONS is empty or does not have a
%   field named 'name', then optionget returns the value of
%   the structure field 'name' from he DEFAULT structure. If
%   DEFAULT is not a structure, then if no matching field is
%   found in OPTIONS, optionget returns DEFAULT (value=DEFAULT).
%
% EXAMPLE:
%   opts.label = 'xdata';
%   opts.value = [1 2 3];
%   default.ydata = [45 57 68];
%
%   optionget(opts,'lab',20)        % returns 20
%   optionget(opts,'label')         % returns 'xdata'
%   optionget(opts,'ydata',default) % returns [45 57 68]
%   optionget(opts,'lab')           % returns []
%   optionget(opts,'lab',default)   % returns []
%   optionget([],'ydata',default)   % returns [45 57 68]
%
% (c) 2004, 2005 Jon Wittwer
%-----------------------------------------------------------------

if nargin < 2
  error('Not enough input arguments.');
end
if nargin < 3
  default = [];
end

if ~isempty(options)
    if ~isa(options,'struct')
        error('OPTIONS must be a structure.');
    end
    if isfield(options,name)
        value = getfield(options,name);
    else
        value = [];
    end
else
    value = [];
```

```
end

if isempty(value)
    if isa(default,'struct')
        if isfield(default,name)
            value = getfield(default,name);
        else
            value = [];
        end
    else
        value = default;
    end
end
```

A.3 quantile.m

```
function [q] = quantile(x,probs,rmnan)
%-----------------------------------------------------------------------
% quantile.m - Generic Quantile Function
%     Produces sample quantiles corresponding to the given
%     probabilities. The smallest observation corresponds to a
%     probability of 0 and the largest to a probability of 1.
%
%SYNTAX:
%   [q] = quantile(x,probs,rmnan)
%
%INPUTS:
%
%       x = numeric vectors whose sample quantiles are wanted.
%   probs = numeric vector with values in [0,1].
%   rmnan = logical; if TRUE, any NaNs values are removed from X
%           before the quantiles are computed. Default is FALSE.
%
%OUTPUTS:
%       Q = vector of length 'length(probs)'
%
%Details:
%
%     After ordering the vector x ...
%     Basic quantile is based upon prob = (i-0.5)/n
%     This function is based upon prob = (i-1)/(n-1)
%
%     The value is found by linearly interpolating between the two
%     points surrounding the desired quantile level.
%
%     NaNs in PROBS are propagated to the result.
%
%EXAMPLES:
%
%   quantile(x,[0.025,0.975]') % gives a 95% confidence interval
%
%TO TEST:
%       This example uses the quantile as an inverse normal distribution
%       function. Note that quantile is not accurate in the 'tails', so for
%       a Normal distribution, it is only accurate within +/- 3 sigma.
%   x = randn(1000000,1);
%   probs = [pnorm(-6),pnorm(-3),pnorm(-2),pnorm(2),pnorm(3),pnorm(6)]';
```

```
%   quantile(x,probs)
%-------------------------------------------------------------------------

if nargin < 2
    error('Not enough input arguments.');
end

% Remove NaNs from Vector
try
    if rmnan
        x = x(~isnan(x));
    end
end
n = length(x(:,1));
ox = sort(x);
% Need to add one more point to make interpolation work
ox(n+1) = ox(n);

% Force probs to be a column vector
[zzz1,zzz2] = size(probs);
if zzz2 > 1
    probs = probs';
end

r = 1 + (n-1)*probs;
r1 = floor(r);
f = r - r1;
q = ox(r1) + f.*(ox(r1+1)-ox(r1));
```

A.4 Spider Graph Functions

The dcespider.m and gspider.m functions can be used to create spider graphs which help evaluate the nonlinearity of a model with respect to input perturbations. The dcespider.m function creates the design and input matrices based upon a vector of inputs and perturbations. After evaluating a function at each design point, the gspider.m function can be used to create the spider graph.

A.4.1 dcespider.m

```
function [D,X,dX] = dcespider(x,dxmin,dxmax,options)
%-------------------------------------------------------------------
% dcespider.m - Creates a design matrix for a spider graph
%   This is used for evaluating a model at evenly spaced
%   points for the creation of spider graphs.
%
% USAGE:
%   [D, X, dX] = dcespider(x,dxmin,dxmax,options)
```

```
%   [D, X, dX] = dcespider(x,dxmin,dxmax) uses default options
%
%   [D, X, dX] = dcespider(x,dx,options) evaluates at ±dx
%   [D, X, dX] = dcespider(x,dx) uses default options
%
%   [D, X, dX] = dcespider(x,options) dx is a percent of x
%   [D, X, dX] = dcespider(x) uses default options
%
% INPUTS:
%   x - Vector of k parameters: Nominal Values
%   dxmin - Vector of k parameters: Backward perturbation
%   dxmax - Vector of k parameters: Forward perturbation
%   options - Structure (see below)
%
% OUTPUTS:
%   D - (N+1) x k design matrix representing N experimental runs
%   X - (N+1) x k matrix of input values
%   dX - (N+1) x k matrix of perturbations from nominal
%
% OPTIONS:
%   Use OPTIONS = [] as a place holder if no options are set.
%   .points = [4] Vector for specifying the number of points
%             for each input variable. A single integer can be
%             used to indicate the same number points for all variables.
%             Minimum (default) is 3 (dxmin, nominal, dxmax)
%   .percent = [10] If dx is empty, dx is set to percent*x
%   .nonom = [0=false] If true, nominal is not included
%
% INFO:
%   k - Number of parameters
%   N+1 - Number of runs + nominal: sum(points)+1
%         or points*length(x)+1
%
% EXAMPLE:
%   x = [ 1 2 3 ]';
%   dx = 0.5*x;
%   [D, X, dX] = dcespider(x,dx);
%
%   opts.points = 10;
%   [D, X, dX] = dcespider(x,-dx,dx,opts);
%   [D, X, dX] = dcespider(x,dx,opts);
%
% (c) 2004, 2005 Jon Wittwer
%-------------------------------------------------------------------------
defaultopt = struct( ...
    'points',4,...
    'nonom',0,...
    'percent',10);

if nargin < 1
    error('dcespider: Not Enough Input Arguments');
end

if nargin == 1
    options = defaultopt;
    dxmax = optionget(options,'percent',defaultopt)/100*x;
    dxmin = -dxmax;
end
if nargin == 2
```

```
    if isa(dxmin,'struct')
        options = dxmin;
        dxmax = optionget(options,'percent',defaultopt)/100*x;
        dxmin = -dxmax;
    else
        options = defaultopt;
        dxmax = dxmin;
        dxmin = -dxmax;
    end
end
if nargin == 3
   if isa(dxmax,'struct')
       options = dxmax;
       dxmax = dxmin;
       dxmin = -dxmax;
   else
       options = defaultopt;
   end
end

points = optionget(options,'points',defaultopt);
if length(points) == 1
    points = points*ones(length(x),1);
end

[k,z] = size(x);
if z > 1 & k > 1
    error('x must be a column vector (k x 1)');
elseif z > 1
    % change row vector to column vector
    x = x';
end
k = length(x);

% Set Up Design Matrix
row = 1;
if ~optionget(options,'nonom',defaultopt)
    D(row,:) = zeros(k,1)';  % Nominal
    row = 2;
    N = sum(points)+1;
else
    N = sum(points);
end

jn = ones(N,1);
dX = zeros(N,k);
for i = 1:k
    dxnorm = linspace(-1,1,points(i))';
    dxactual = interp1([-1 1],[dxmin(i) dxmax(i)],dxnorm);
    D(row:(row+points(i)-1),i) = dxnorm;
    dX(row:(row+points(i)-1),i) = dxactual;
    row = row+points(i);
end

% Create Input Matrix
X = (x*jn')' + dX;
```

A.4.2 gspider.m

```
function [xplot,yplot] = gspider(D,y,options)
%-------------------------------------------------------------------------
% gspider.m - Create a Spider Graph
%
% USAGE:
%   gspider(D,y)
%   gspider(D,y,options)
%
%   [X,Y] = gspider(...) returns the data used to create the plot
%           (X and Y are sorted in ascending order)
%
%   Note: This function uses the plot3() function, allowing you to
%         rotate the graph in 3D to see whether lines are overlapping.
%
% INPUTS:
%   D = n x k Scaled design matrix
%   y = n x 1 Output vector
%
% OPTIONS:
% Use OPTIONS = [] as a place holder if no options are set.
%   options.format = ['o-'] Format for lines in graph
%   options.legend = {xLABELS} where xLABELS is an array of
%                    strings: xLABELS={'var1','var2','var3'}
%
% EXAMPLE:
%   x = [ 1 2 3 ]';
%   dx = 0.2*x;
%   [D, X, dX] = dcespider(x,dx);
%
%   %y = sum function to evaluate the model at each design point
%   y = [ X(:,1) + X(:,2).^3 + X(:,3).^2 ];
%
%   gspider(D,y);
%
%   opts.format = 'x-';
%   opts.legend = {'var1','var2','var3'};
%   opts.error = 1;
%   gspider(D,y,opts);
%
% (c) 2004, 2005 Jon Wittwer
%-------------------------------------------------------------------------

% The following default options will be used if not set
defaultopt = struct( ...
    'format','o-',...
    'error',0);

% Check input arguments
if nargin < 2
    error('Not enough input arguments.');
end
if nargin < 3 | isempty(options)
    options = defaultopt;
end

% Determine size of input matrices
```

```
[n,k] = size(D);
[ny,p] = size(y);
if p > 1
    error('y must be a single column vector');
end
if ny ~= n
    error('length of y must match length of D');
end

gformat = optionget(options,'format',defaultopt);

% Transform y to Deviation Space
% Assumes that the first row is the nominal value
if optionget(options,'error',defaultopt)
    y = y-y(1);
    ylabstr = 'Deviation from Nominal Response';
else
    ylabstr = 'Response Value';
end

% Plot lines based upon main effects only
for i = 1:k
    cols = zeros(1,k);
    cols(i) = 1;    % set desired column to 1=true
    rows = sum(abs(D(:,cols~=1))')'==0;
    gplot(:,1) = D(rows,i);
    gplot(:,2) = y(rows);
    gplot = sortrows(gplot,[1]);
    xplot(:,i) = gplot(:,1);
    yplot(:,i) = gplot(:,2);
    zplot(:,i) = (i-1)*ones(length(xplot(:,i)),1);
end

%plot(xplot,yplot,gformat);
plot3(xplot,yplot,zplot,gformat);
view(2); %top view
title('Spider Plot');
ylabel(ylabstr);
xlabel('Normalized Perturbations');

if isfield(options,'legend')
    legend(options.legend);
end
```

A.5 Chapter 6 Example

```
% ========================================
% Define NOMINAL PARAMETERS
w = 2; w_sd = 0.08;
t = 5; t_sd = 0.02;
x = [w t]';
xmean = x; % Assume nominal = mean

% ========================================
% Define UNCERTAINTIES and PERTURBATIONS
xsd = [w_sd t_sd]';
```

```
dx = xsd;

% ==========================================
% Create the DESIGN matrices
Ds = [ 0 0; 1 0; 0 1; -1 0; 0 -1; ...
       1 1; 1 -1; -1 1; -1 -1];
[N,k] = size(Ds);
jN = ones(N,1);
dX = Ds.*(jN*dx');  % input perturbation matrix
D = jN*x'+dX;   % design matrix

% ==========================================
% Run the MODEL
b_vec = X(:,1);
h_vec = X(:,2);
A = b_vec.*h_vec;
Iy = b_vec.*h_vec.^3/12;
Iz = h_vec.*b_vec.^3/12;
Y = [A Iy Iz];
dY = [A-A(1) Iy-Iy(1) Iz-Iz(1)];

% ==========================================
% Create the Xreg MATRIX
Xreg = [ dX(:,1) dX(:,2) dX(:,1).^2 dX(:,2).^2 dX(:,1).*dX(:,2) ];

% ==========================================
% Perform Multiple Regression
B = inv(Xreg'*Xreg)*Xreg'*dY
```

APPENDIX B CROSS-SECTION MODEL IN MATLAB

The following MATLAB scripts and functions are used to calculate various cross-sectional area properties for stacked or laminated beams. The MATLAB code to calculate the cross-section properties for an I-beam created using the Poly3 and Poly4 layers in the SUMMiT V™ process is:

```
layersSUMMiT;
layers = { poly12; oxide3; poly3 };
areaprops = Xsection(layers);
```

The m-files for the layersSUMMiT and Xsection scripts are given below.

B.1 layersSUMMiT.m

This script is used as a configuration file to define the cross-section geometry for layers in the SUMMiT V™ process. Values defined in this file are subject to change depending on the current state of the technology.

```
% Layer Definitions
%
%   The widths (*.b and *.a) should be modified to match a
%   specific design. Other properties such as layer thicknesses
%   and uncertainties are process-specific. The distributions
%   should also be chosen carefully.
%
% Layer Shapes:
%   See help on Xtrap, Xtrap2, and Xrect
%
% Structure Field Names:
%   The field names are important, as they are used in other scripts
%   for defining the set of uncertainties.

edgebias = 0.1; % Sometimes 0.15 is used
```

```
edgebias_sd = 0.04; % Rule-of-thumb edge bias variation
% Note that *.b_sd takes into account edge bias variation

% Rule-of-thumb alignment variation
dx_sd = 0.1; %dx_sd = 0.25; % Design rules state 0.5 enclosure
dx_dist = 'u';

poly1.h = 1; poly1.h_sd = 0.021;
poly1.b = 4-2*edgebias; poly1.b_sd = 0.064;
poly1.shape = 'rect';
poly1.dx = 0;

poly2.h = 1.5; poly2.h_sd = 0.037;
poly2.b = 4-2*edgebias; poly2.b_sd = 0.064;
poly2.shape = 'rect';
poly2.dx = 0;

poly12.h = 2.5; poly12.h_sd = 0.05;
poly12.b = 4-2*edgebias; poly12.b_sd = 0.064;
poly12.shape = 'rect';
poly12.dx = 0;

% Oxide3 target is 1.8 with a 0.4 backfill
oxide3.h = 2.2; oxide3.h_sd = 0.350;
oxide3.a = 2; oxide3.a_sd = 0.2;
oxide3.q = -10; oxide3.q_sd = 2;
oxide3.shape = 'trap2';
oxide3.dx = 0;

poly3.h = 2.25; poly3.h_sd = 0.041;
poly3.b = 4-2*edgebias; poly3.b_sd = 0.08;
poly3.shape = 'rect';
poly3.dx = 0;

% Oxide4 target is 1.8 with a 0.2 backfill
oxide4.h = 2; oxide4.h_sd = 0.181;
oxide4.a = 2; oxide4.a_sd = 0.08;
oxide4.q = -10; oxide4.q_sd = 2;
oxide4.shape = 'trap2';
oxide4.dx = 0;

poly4.h = 2.25; poly4.h_sd = 0.042;
poly4.b = 4-2*edgebias; poly4.b_sd = 0.08;
poly4.shape = 'rect';
poly4.dx = 0;
```

B.2 Xsection.m

```
%-------------------------------------------------------------
% Area Properties for Stacked Beams
%
% USAGE:
%  areaprops = Xsection(layers)
%
% INPUTS:
%  layers = cell array of layer structures
%
```

```
% OUTPUTS:
%  Structure areaprops with the following fields:
%  .A = total Area
%  .xc = distance from y-axis to centroid
%        (y-axis is relative to chosen ex values)
%  .yc = distance from x-axis to centroid
%        (x-axis is at the bottom of the lowest layer)
%  .Ixc = centroidal moment of inertia about x-axis
%  .Iyc = centroidal moment of inertia about y-axis
%  .Ixcyc = centroidal product of inertia
%  .thetap = angle (in degrees) to principal moments
%  .htotal = total height
%
% REFERENCE:
%  More information + schematic: help Xtrap
%-------------------------------------------------------------%

function areaprops = Xsection(layers)

n = length(layers);

% Define vectors
vA = zeros(n,1);
vdyc = zeros(n,1);
vdxc = zeros(n,1);
vIxc = zeros(n,1);
vIyc = zeros(n,1);

% htotal keeps track of current height relative to bottom
htotal = 0;
for i = 1:n
    theLayer = layers{i,1};
    if strcmp(theLayer.shape,'rect')
        [vA(i,1),zzzxc,yc,vIxc(i,1),vIyc(i,1),vIxcyc(i,1),Ip] = ...
               Xrect(theLayer.b,theLayer.h);
        vdxc(i,1) = theLayer.dx;
        vdyc(i,1) = htotal + yc;
        htotal = htotal + theLayer.h;
    end
    if strcmp(theLayer.shape,'trap')
        S = Xtrap(theLayer.a,theLayer.b,theLayer.h);
        vA(i,1) = S.A;
        yc = S.yc;
        vIxc(i,1) = S.Ixc;
        vIyc(i,1) = S.Iyc;
        vIxcyc(i,1) = S.Ixcyc;
        vdxc(i,1) = theLayer.dx;
        vdyc(i,1) = htotal + yc;
        htotal = htotal + theLayer.h;
    end
    if strcmp(theLayer.shape,'trap2')
        S = Xtrap2(theLayer.a,theLayer.q,theLayer.h);
        vA(i,1) = S.A;
        yc = S.yc;
        vIxc(i,1) = S.Ixc;
        vIyc(i,1) = S.Iyc;
        vIxcyc(i,1) = S.Ixcyc;
        vdxc(i,1) = theLayer.dx;
        vdyc(i,1) = htotal + yc;
```

```
        htotal = htotal + theLayer.h;
    end
end

vec.A = vA;
vec.dyc = vdyc;
vec.dxc = vdxc;
vec.Ixc = vIxc;
vec.Iyc = vIyc;

areaprops = Xtotal(vA,vdxc,vdyc,vIxc,vIyc,vIxcyc);
areaprops.htotal = htotal;
areaprops.vec = vec;
areaprops.thetap = 180/pi*areaprops.thetap; % degrees
```

B.2.1 Xtrap.m

```
%-------------------------------------------------------------%
% Properties of Plane Areas - Y-Symmetric Trapezoid
% areaprops = Xtrap(a,b,h)
%
% INPUT:
%   a - top width
%   b - bottom width
%   h - height or thickness
%   Origin of Axes at the Centroid
%
% OUTPUT:
%   areaprops = Structure with the fields 'A', 'xc', 'yc',
%               'Ixc','Iyc','Ixcyc'
%
%           |--a--|
%     y     |  yc |
%_____|___  a/2|__|
% |   |    /   |   \
% |   |   /    |    \
% h   |  /     |     \
% |   | /      |------\--------- xc
% |   |/       |       \    yc
%_|__ /___b/2__|________\_______ x
%     |                 |
%     |----------- b ---|
%
% Example:
%   Xtrap(1.9,1,2)
%-------------------------------------------------------------%

function areaprops = Xtrap(a,b,h)
    q = 180/pi*(atan((b-a)./(2*h)));
    areaprops.a = a;
    areaprops.b = b;
    areaprops.q = q;
    areaprops.h = h;
    areaprops.A = h./2.*(a+b);
    areaprops.xc = b./2;
    areaprops.yc = h./3.*(2*a+b)./(a+b);
    areaprops.Ixc = h.^3.*(a.^2+4*a.*b+b.^2)./(36.*(a+b));
```

```
    areaprops.Iyc = h./48.*(a.^3+b.^3+a.*b.^2+a.^2.*b);
    areaprops.Ixcyc = 0;
return
```

B.2.2 Xtrap2.m

```
%-------------------------------------------------------------%
% Properties of Plane Areas - Y-Symmetric Trapezoid
% areaprops = Xtrap2(a,q,h)
%
% INPUT:
%   a - top width
%   q - (degrees) angle measured from vertical
%       Positive angle results in a < b
%   h - height or thickness
%   Origin of Axes at the Centroid
%
% OUTPUT:
%   areaprops = Structure with the fields 'A', 'xc', 'yc',
%               'Ixc','Iyc','Ixcyc'
%
%           |--a--|
%     y     |  yc |
%_____|___  a/2|__|
% |   |    /   |   \
% |   | q /    |    \
% h   |  /     |     \
% |   | /      |------\--------- xc
% |   |/       |       \    yc
%_|__ /___b/2__|________\_______ x
%     |                 |
%     |----------- b ---|
%
% Example:
%   Xtrap2(1.9,-12.6804,2)
%-------------------------------------------------------------%

function areaprops = Xtrap2(a,q,h)
    q = q*pi/180;   % convert to radians
    b = a+2*h*tan(q);
    areaprops.a = a;
    areaprops.b = b;
    areaprops.q = q;
    areaprops.h = h;
    areaprops.A = h./2.*(a+b);
    areaprops.xc = b./2;
    areaprops.yc = h./3.*(2*a+b)./(a+b);
    areaprops.Ixc = h.^3.*(a.^2+4*a.*b+b.^2)./(36.*(a+b));
    areaprops.Iyc = h./48.*(a.^3+b.^3+a.*b.^2+a.^2.*b);
    areaprops.Ixcyc = 0;
return
```

B.2.3 Xrect.m

```
%-------------------------------------------------------------
% Properties of Plane Areas - Rectangle
```

```
% [A,xc,yc,Ixc,Iyc,Ixcyc,Ip] = Xrect(bx,hy)
%
% INPUTS:
%   bx - width in the x-direction
%   hy - height in the y-direction
%   Origin of Axes at the Centroid
%
%   y    yc
%   |____|____
%   |    |    |
% h |    |    |
%   |    |----|--- xc
%   |         |
%   |_________|___ x
%        b
%
% Example:
%   [A,xc,yc,Ixc,Iyc,Ixcyc,Ip] = Xrect(3,4)
%-------------------------------------------------------------

function [A,xc,yc,Ixc,Iyc,Ixcyc,Ip] = Xrect(b,h)
    A = b.*h;
    xc = b./2;
    yc = h./2;
    Ixc = b.*h.^3/12;
    Iyc = h.*b.^3/12;
    Ixcyc = 0*b;
    Ip = b.*h/12.*(h.^2+b.^2);
return
```

B.2.4 Xtotal.m

```
%-------------------------------------------------------------%
% Stacked Area Properties
% results = Xtotal(vA,vxc,vyc,vIxc,vIyc,vIxcyc)
%
% INPUTS:
%    vA - vector of component areas
%    vxc - vector of x-coordinates of the centroids
%    vyc - vector of y-coordinates of the centroids
%    vIxc - vector of centroidal moments of inertia (about y-y)
%    vIyc - vector of centroidal moments of inertia (about x-x)
%    vIxcyc - vector of centroidal products of inertia
%
% OUTPUTS:
%    results = [Structure]
%-------------------------------------------------------------%

function results = Xtotal(vA,vxc,vyc,vIxc,vIyc,vIxcyc)
    n = length(vA);
    j = ones(n,1);
    % Total the Area
    A = sum(vA);
    % Find the Centroid
    xc = sum(vxc.*vA)/A;
    yc = sum(vyc.*vA)/A;
    % Moments of Inertia via Parallel Axis Theorem
```

```
    vdx = vxc-xc*j;
    vdy = vyc-yc*j;
    Ixc = sum(vIxc + vA.*vdy.^2);
    Iyc = sum(vIyc + vA.*vdx.^2);
    Ixcyc = sum(vIxcyc + vA.*vdx.*vdy);
    I1 = (Ixc+Iyc)/2 + sqrt(((Ixc-Iyc)/2)^2+Ixcyc^2);
    I2 = (Ixc+Iyc)/2 - sqrt(((Ixc-Iyc)/2)^2+Ixcyc^2);
    thetap = 0.5*atan(-2*Ixcyc/(Ixc-Iyc));

    % Place output into Structure
    results.A = A;
    results.xc = xc;
    results.yc = yc;
    results.Ixc = Ixc;
    results.Iyc = Iyc;
    results.Ixcyc = Ixcyc;
    results.I1 = I1;
    results.I2 = I2;
    results.thetap = thetap;
return
```

APPENDIX C THERMAL ACTUATOR FEA MODEL

C.1 ANSYS batch file

```
!================================================================
!  FileName: ansys_ta_full.inp
!  Created by Jon Wittwer, 11 Nov 2004
!  ANSYS Parametric Batch File - ADPL Language
!================================================================
FINISH
/CLEAR
/TITLE,Analysis of a Linear Thermomechanical Microactuator
/PREP7
*AFUN,DEG

!================================================================
!               INPUT VARIABLES
!================================================================
!ts = 4.5
!Ey = 164000
!Sr = -10
!Pr = 0.23
!Et = 0.000003
!Lx = 200
!Ly = 2.5
!ws = 10
!Px = 5
!Py = 10
!Tmax = 450
!getdYmax = 1
!dYmax = 8.5
!dYmin = 0
!expansionSteps = 10
!loadSteps = 20
!legpairs = 4
!saveimage = 1
!*DIM,b,ARRAY,legpairs-1,1
!b(1) = 80
!*DIM,w,ARRAY,legpairs,2  ! w(legpair, 1=left or 2=right)
!w(1,1) = 3.8
!w(2,1) = 3.8
!w(1,2) = 3.8
!w(2,2) = 3.8
!*DIM,A,ARRAY,legpairs,2  ! w(legpair, 1=left or 2=right)
!A(1,1) =
!A(2,1) =
!A(1,2) =
```

```
!A(2,2) =
!*DIM,I,ARRAY,legpairs,2  ! w(legpair, 1=left or 2=right)
!I(1,1) =
!I(2,1) =
!I(1,2) =
!I(2,2) =

! === Read from input file ===
/INPUT,ANSYS_ta_inputs,txt


!=================================================================
!               RELATIONAL PARAMETERS
!=================================================================

datapoints = expansionSteps+1+loadSteps+1

prestrain = Sr/Ey
segments=100

Is=ts*ws*ws*ws/12
As=ts*ws

!=================================================================
!               MODEL SETUP
!=================================================================

/PNUM,LINE,1
/PNUM,KP,1

K,1000,Px,Py,0
K,1,0,0,0
L,1,1000

bsum=0
*DO,n,1,legpairs-1,1
  bsum=bsum-b(n)
  K,1+n,0,bsum,0
  L,n,1+n
*ENDDO
LSEL,S,LINE,,1,legpairs
LESIZE,ALL,,,20

bsum=0
*DO,n,1,legpairs,1
  K,100+n,-Lx,bsum-Ly,0
  L,n,100+n
  *IF,n,NE,legpairs,THEN
    bsum=bsum-b(n)
  *ENDIF
*ENDDO

bsum=0
*DO,n,1,legpairs,1
  K,200+n,Lx,bsum-Ly,0
  L,n,200+n
  *IF,n,NE,legpairs,THEN
    bsum=bsum-b(n)
  *ENDIF
```

```
*ENDDO

LSEL,S,LINE,,legpairs+1,3*legpairs
LESIZE,ALL,,,segments
LSEL,ALL

! === Element Type ===
ET,1,BEAM3
type,1

! === Material Properties ===
MP,EX,1,Ey
MP,PRXY,1,Pr
MP,ALPX,1,Et
MP,REFT,1,0

! Material used for lower thermal expansion
MP,EX,2,Ey
MP,PRXY,2,Pr
MP,ALPX,2,Et/100000
MP,REFT,2,0

! === Real Constants and MESH ===
R,1,As*10,Is*1000,ws*10,,0,0
mat,2
real,1
LMESH,1

R,2,As,Is,ws,,prestrain,0
mat,1
real,2
LMESH,2,legpairs,1

mat,1
*DO,n,1,legpairs,1
  R,2+n,A(n,1),I(n,1),w(n,1),,prestrain,0
  real,2+n
  LMESH,legpairs+n
*ENDDO

*DO,n,1,legpairs,1
  R,legpairs+2+n,A(n,2),I(n,2),w(n,2),,prestrain,0
  real,legpairs+2+n
  LMESH,2*legpairs+n
*ENDDO


! === Get Node Numbers from Keypoints ===
KSEL,S,KP,,1000
NSLK,S
*GET,nkp1000,NODE,0,NUM,MAX
NSEL,ALL
KSEL,ALL

! === Get Node Numbers from Keypoints ===
KSEL,S,KP,,1
NSLK,S
*GET,nkp1,NODE,0,NUM,MAX
NSEL,ALL
```

```
KSEL,ALL

FINISH
!=================================================================
!                SOLUTION STEPS
!=================================================================
/SOLU

! === Nonlinear ===
NLGEOM,1

! === Static Problem ===
ANTYPE,0

! === Boundary Conditions
*DO,n,1,legpairs,1
  DK,100+n,ALL,0
  DK,200+n,ALL,0
*ENDDO

!============ INITIAL THERMAL EXPANSION  =============
TREF,0
*DIM,Temps,ARRAY,datapoints,1
*DO,mm,1,expansionSteps+1,1
  Temps(mm,1) = (mm-1)*Tmax/expansionSteps
  TUNIF,Temps(mm,1)
  lswrite,mm
*ENDDO
lssolve,1,expansionSteps+1

*IF,getdYmax,EQ,1,THEN
  *GET,dYmax,NODE,nkp1000,U,Y
*ENDIF

!============ VERTICAL DISPLACEMENT  =============
*DO,mm,1,loadSteps+1,1
  DK,1000, ,dYmax-(mm-1)*(dYmax-dYmin)/loadSteps, , , ,UY, , , , ,
  lswrite,mm+expansionSteps+1
*ENDDO
lssolve,expansionSteps+2,datapoints

FINISH
!=================================================================
!                  POST PROCESS RESULTS
!=================================================================
/POST1

*DIM,Ydis,TABLE,datapoints
*DIM,Yforce,TABLE,datapoints
*DIM,Smax,TABLE,datapoints
*DIM,Zrot,TABLE,datapoints

*DO,mm,1,datapoints,1
  SET,mm

  ETABLE,,NMISC,1
  ETABLE,,NMISC,2
  ETABLE,,NMISC,3
  ETABLE,,NMISC,4
```

```
  SABS,1
  SMAX,ms1,NMIS1,NMIS3
  SMAX,ms2,NMIS2,NMIS4
  SMAX,ms3,ms1,ms2
  ESORT,ETAB,ms3,0,1,,
  *GET,stress,SORT,,MAX
  *SET,Smax(mm),stress

  *GET,disY,NODE,nkp1000,U,Y
  *SET,Ydis(mm),disY

  *GET,rotZ,NODE,nkp1000,ROT,Z
  *SET,Zrot(mm),rotZ

  *IF,mm,GT,expansionSteps+1,THEN
    *GET,forceY,NODE,nkp1000,RF,FY
    *SET,Yforce(mm),forceY*(-1)
    *SET,Temps(mm),Tmax
  *ELSE
    *SET,Yforce(mm),0
  *ENDIF

*ENDDO

*VPLOT,Ydis(1,1),Yforce(1,1)
/output,ANSYS_ta_results.txt
*VWRITE
       Displacement               Force              Stress                 Temp
Zrot
*VWRITE,Ydis(1),Yforce(1),Smax(1),Temps(1),Zrot(1)
%20e %20e %20e %20e %20e
/output

*IF,saveimage,EQ,1,THEN
  SET,LAST
  ! Background Colors: WHIT, BLAC, LGRA (light gray)
  /COLOR,WBAK,WHIT
  /SHOW,JPEG
  PLETAB,ms3,NOAV
  /SHOW,TERM
*ENDIF

FINISH
/eof
```